Università degli Studi di Torino

Facoltà di Scienze Matematiche, Fisiche e Naturali
Dottorato di Ricerca in Fisica - XIX ciclo
FIS/01 - Fisica Sperimentale

Simulation, Performance and Local Track Reconstruction of the Drift Tube Detectors of the CMS Experiment.

Coordinatore
Prof. Stefano Sciuto

Tutore
Dott. Ernesto Migliore

Candidato
Dott. Gianluca Cerminara

14 Dicembre 2006

Contents

Introduction

The Standard Model (SM) of particle physics has been experimentally tested with very high accuracy over a wide range of energies, and can be considered one of the most successful theories of modern physics. However, the SM still presents some open questions which must be addressed. In particular the mechanism which gives mass to all particles remains unexplained. The mechanism proposed to describe the introduction of the mass terms of the Lagrangian is the so called "Higgs mechanism" in which fermions and bosons acquire their masses because of a scalar field, the Higgs boson, which has not yet been observed. Regardless of the correctness of this explanation, there is widespread consensus that new physics must appear at energies higher than those reached by present particle accelerators.

This has lead to the design of the Large Hadron Collider (LHC), a machine which will collide proton beams with very high energy and luminosity. The LHC will be installed at the European Laboratory for Nuclear Research (CERN) in Geneva (Switzerland). The first beam is expected to be delivered in the second half of 2007. Four experiments will collect data at the LHC: two of them are the general-purpose experiments ATLAS and CMS, while the others are the ALICE detector, designed for the study of heavy ion collisions, and LHC-b, dedicated to b-physics.

This thesis describes the work I did for the Compact Muon Solenoid (CMS) collaboration within the Muon Physics Reconstruction and Selection (PRS/mu) group, whose purpose is to implement the full chain of simulation, reconstruction and selection of muons from the first level of trigger up to the off-line analysis. Many interesting LHC processes result in a final state containing muons with high transverse momenta: the muon spectrometer will thus play a key role both in the trigger and in the reconstruction of such events. The focus of my work has been the development and the study of the performance of the simulation and of the local reconstruction in the barrel Drift Tube (DT) detectors of the muon spectrometer.

In particular, my work covered the development and the test of the simulation of the drift cell response, based on a parametrization of the cell behavior, as described in Chapter 3. I also contributed to the algorithms for the recon-

struction of hits in the cell gas volume and for the reconstruction of muon track segments in the chambers. Both algorithms are described in detail in Chapter 4. These steps of the reconstruction require an accurate synchronization and calibration procedure: the development of the calibration strategies has been part of my task in the PRS/mu collaboration and is described in Chapter 5.

To validate the whole simulation and reconstruction chain I took part to the test-beam of the Autumn 2004, when two DT chambers were exposed to a bunched muon beam. I then participated to the data analysis working on the comparison between simulation and real data. The results of this work are presented in Chapter 6.

The DT simulation and the reconstruction algorithms described in this thesis have been documented in the Physics Technical Design Report (TDR) Volume I, submitted in February 2006 [1], and they have been used for all studies of the physics reach of the experiment, documented in the Physics Technical Design Report Volume II submitted in June 2006 [2].

The reconstruction algorithms have also been employed in the validation of the chamber performance during the commissioning which is on-going since May 2005. This consists in a detailed test of the on-chamber read-out and trigger electronics and in a data-taking using one chamber at a time exposed to cosmic muons. I took part in the commissioning, participating to the acquisition and to the analysis of the data and contributing to the development of the Data Quality Monitoring (DQM) tasks.

During the last year the CMS collaboration went through a re-engineering of the basic framework and design of the simulation and reconstruction code. In this context I was responsible of the porting of the DT simulation and local reconstruction software in the new official software of the experiment, called CMSSW.

An important benchmark for this new framework has been the Magnet Test and Cosmic Challenge (MTCC), which took place over the Summer 2006. It has been a combined data taking of a part of each of the CMS sub-detectors exposed to cosmic muons, using the final read-out and trigger electronics. I took part in the data taking and I contributed to the development of the DQM applications, running on-line on the filter farm machines. The MTCC has been a very successful test for the reconstruction software, demonstrating that it fits all the requirements for the on-line processing and the needs of the user community.

Chapter 1

Physics with the Large Hadron Collider

The Large Hadron Collider (LHC) is a proton-proton collider under construction at CERN. With a centre-of-mass energy of 14 TeV and a design luminosity of $10^{34}\text{cm}^{-2}\text{s}^{-1}$, it is a machine of unprecedented complexity and potential.

This chapter introduces the motivation, the design and the physics programme of LHC. In Section 1.1, a short overview of the Standard Model is given with the aim of introducing the open issues that LHC is expected to explore. The design of the LHC, the experimental environment and the requirements for the LHC experiments are described in Section 1.2. Finally, an overview of the main physics studies feasible at the LHC is presented in Section 1.3.

1.1 The Standard Model

The current picture of Particle Physics provides a description of the basic components of matter and their interactions. The present belief is that all known matter can be described through twelve fundamental particles, the *fermions*, which interact through three types of interactions: *electromagnetic*, *weak* and *strong* interactions. A fourth type of force is needed to describe the Universe, the *Gravitation*. Although this is the interaction closest to everyday experience, its effect is negligible at the scale of mass and distance typical of particle physics.

The electromagnetic interaction is responsible of the bond between atoms and molecules, while the weak interaction explains radioactivity and nuclear decays. Finally, the confinement of partons inside the nucleons is due to strong interactions. All these interactions are described in terms of the exchange of integer spin particles called *bosons*. The characteristics of electromagnetic, weak and strong interactions are summarized in Table 1.1.

Table 1.1: *Fundamental interactions relevant in particle physics.*

	Electromagnetic	**Weak**	**Strong**
Quantum	Photon (γ)	$W^{\pm}$ and Z	Gluons
Mass (GeV/c^2)	0	80–90	0
Coupling constant	$\alpha(Q^2 = 0) \approx \frac{1}{137}$	$G_F \approx 1.2 \times 10^{-5}\,\mathrm{GeV}^{-2}$	$\alpha_s(m_Z) \approx 0.1$
Range (cm)	∞	10^{-16}	10^{-13}

The fermions can be divided into two main groups according to their different behavior with respect to the four interactions: leptons and quarks. The leptons, which include electrons, muons, taus and neutrinos, interact through weak and electromagnetic interactions while the quarks are particles which also feel the strong interaction. Quarks have a fractional charge and do not freely exist in nature; they are the constituents of the *hadrons*, a wide class of particles which includes protons and neutrons.

The twelve fundamental particles can be also divided in three families, each of them with the same general behavior under the weak interaction. A classification of fermions is given in Table 1.2.

Table 1.2: *Classification of the three families of fundamental fermions.*

Fermions	**1st fam.**	**2nd fam.**	**3rd fam.**	**Charge**	**Interactions**
Quarks	$\begin{pmatrix} u \\ d \end{pmatrix}$	$\begin{pmatrix} c \\ s \end{pmatrix}$	$\begin{pmatrix} t \\ b \end{pmatrix}$	$+\frac{2}{3}$ $-\frac{1}{3}$	All
Leptons	$\begin{pmatrix} \nu_e \\ e \end{pmatrix}$	$\begin{pmatrix} \nu_\mu \\ \mu \end{pmatrix}$	$\begin{pmatrix} \nu_\tau \\ \tau \end{pmatrix}$	0 -1	Weak Weak, E.M.

The three fundamental interactions are descried with two theories:

- the theory of the electroweak interaction, or Electroweak Standard Model (SM), that unifies the electromagnetic and the weak interaction;
- the theory of strong interactions or Quantum Chromodynamics (QCD).

The SM for weak and electromagnetic interactions is constructed from a gauge theory with four gauge fields, the photon and the massive bosons $W^{\pm}$ and Z. The masses of the gauge fields, as well as the masses of the fermions, are

generated by spontaneous symmetry breaking. A renormalizable theory which perfectly reproduces the low energy phenomenology is then obtained.

A comprehensive description of the Electroweak Standard Model is outside the scope of this work. However, the main results are reviewed in the following sections.

1.1.1 Gauge Symmetry and Electroweak Unification

The theory of electromagnetic interactions is called Quantum Electrodynamics (QED), and it is based on the invariance of the Lagrangian for local gauge transformations with respect to the U(1) symmetry group. This condition leads to the existence of a massless vector field, the photon.

During the late sixties, Salam, Glashow and Weinberg proposed the unification of the QED with the theory of the weak interactions. This unification is accomplished by extending the symmetry of the Lagrangian to the group SU(2)×U(1) [3]. The quantum numbers associated with this group are the weak isospin I and the weak hypercharge Y which satisfy the relation:

$$Q = I_3 + \frac{Y}{2}, \tag{1.1}$$

with I_3 being the third component of the weak isospin and Q the electric charge.

To achieve local gauge invariance under SU(2)×U(1) transformations, four massless vector fields must be introduced: $W_\mu^{1,2,3}$ for SU(2) and B_μ for U(1). The corresponding gauge coupling constants with fermions are g and g'. The physical fields are linear combinations of $W_\mu^{1,2,3}$ and B_μ: the charged bosons W^+ and W^- correspond to

$$\mathrm{W}_\mu^\pm = \sqrt{\frac{1}{2}}(\mathrm{W}_\mu^1 \pm i\mathrm{W}_\mu^2), \tag{1.2}$$

while the neutral bosons γ and Z are obtained by mixing the neutral fields W_μ^3 and B_μ with a rotation defined by the *weak mixing angle* θ_W:

$$A_\mu = B_\mu \cos\theta_W + W_\mu^3 \sin\theta_W \tag{1.3}$$

$$Z_\mu = -B_\mu \sin\theta_W + W_\mu^3 \cos\theta_W. \tag{1.4}$$

The field A_μ is then identified with the electromagnetic field; requiring the coupling terms to be equal, one obtains

$$g \sin\theta_W = g' \cos\theta_W = e. \tag{1.5}$$

In this way the electroweak unification is achieved.

1.1.2 Electroweak Symmetry Breaking in the Standard Model

The scheme presented in the previous section has been obtained assuming all particles to be massless as a mass term for the gauge bosons in the the Lagrangian would spoil the SU(2)×U(1) gauge invariance.

To solve this problem, the Spontaneous Symmetry Breaking Mechanism was introduced in the theory. This is realized through the Higgs mechanism which allows fermions, $W^{\pm}$ and Z bosons to be massive, while keeping the photon massless. This is accomplished by introducing the Higgs field, a SU(2) doublet of complex scalar fields:

$$\phi = \begin{pmatrix} \phi^+ \\ \phi^0 \end{pmatrix} = \frac{1}{\sqrt{2}} \begin{pmatrix} \phi_1 + i\phi_2 \\ \phi_3 + i\phi_4 \end{pmatrix}. \tag{1.6}$$

In order to preserve the symmetry, the Lagrangian of this field must be invariant under SU(2)×U(1) local gauge transformations. The potential term of the Higgs Lagrangian is:

$$V(\phi) = -\mu^2 \phi^\dagger \phi + \lambda (\phi^\dagger \phi)^2, \tag{1.7}$$

where $\mu^2 > 0$ and $\lambda > 0$, so that the potential has a minimum for

$$\phi^\dagger \phi = \frac{1}{2}(\phi_1^2 + \phi_2^2 + \phi_3^2 + \phi_4^2) = \frac{\mu^2}{2\lambda} \equiv \frac{v^2}{2}. \tag{1.8}$$

This condition is satisfied not only for a particular choice of ϕ_i, but for a manifold of values; this is the bulk of the mechanism. Since the Higgs field has a non-zero vacuum expectation value, the fundamental state of the potential does not share the symmetry properties of the Lagrangian: the symmetry is spontaneously broken.

The boson fields acquire their masses by coupling to the vacuum value of the Higgs field. However, it can be shown that the minimum for the Higgs field is invariant for U(1) transformations; the electromagnetic U(1) symmetry is therefore unbroken and the photon remains massless.

The Higgs mechanism allows to include the weak boson masses while preserving the renormalizability of the theory. A theory based on a Lagrangian which does not respect the gauge symmetry is unrenormalizable and loses therefore all predictive power. Conversely, in a spontaneously broken gauge theory the symmetry is in a sense still present; it is merely "hidden" by our choice of the ground state and the theory can be shown to be renormalizable.

The Higgs mechanism gives rise to three massive gauge bosons, corresponding to nine degrees of freedom. Since the initial number of independent fields is ten (three massless bosons with two polarizations states each, plus the four real

ϕ_i fields), one additional scalar gauge boson should appear as a real particle. This is the Higgs boson. Its mass depends on v and λ: the self coupling can be expressed as

$$\lambda = \frac{{m_H}^2}{2v^2}. \tag{1.9}$$

The value of v is related to the boson masses by the relations:

$$m_{W^\pm}^2 = \left(\frac{1}{2}gv\right)^2; \qquad m_Z^2 = \frac{m_{W^\pm}^2}{\cos^2\theta_W} \tag{1.10}$$

However the parameter λ is characteristic of the field ϕ and cannot be determined from other measurements, so the Higgs mass is unknown.

The fermion masses are generated with a similar mechanism, but appear as free parameters of the theory, six for the quarks and three for the leptons (assuming neutrinos to be massless). These bring the number of free parameters of the Standard model to 17, the others being the four independent elements of the Cabibbo-Kobayashi-Maskawa matrix that describes the mixing of quark flavours, the couplings g and g', the parameter v of the Higgs vacuum expectation value and the Higgs mass.

All these parameters, except the mass of the Higgs boson which has not yet been observed, can be determined from experimental quantities. The measurement of these quantities allows therefore a consistency check of the electroweak Standard Model, which up to now has been confirmed at the level of quantum corrections.

1.1.3 Higgs Mass

Theoretical bounds. The mass of the Higgs boson is not predicted by the SM; however arguments of self-consistency of the theory can be used to yield constraints on its value.

An upper bound on m_H can be found requiring the Higgs self coupling λ to remain finite in its running up to an energy scale Λ (*triviality*). In fact λ rises indefinitely with energy and the theory could eventually become non-perturbative. On the other hand, the requirement that, when radiative corrections are included, the minimum of the potential in eq. 1.7 is an absolute minimum up to the scale Λ leads to a *vacuum stability* condition which limits m_H from below.

In both cases, the parameter Λ represents the scale up to which the Standard Model is taken to be valid. The theoretical bounds on m_H as a function of Λ are shown in Fig. 1.1.

For the SM to remain valid up to the Planck scale ($\Lambda = 10^{19}$ GeV), the Higgs mass must be in the range 130-190 GeV/c^2. Assuming the SM to be

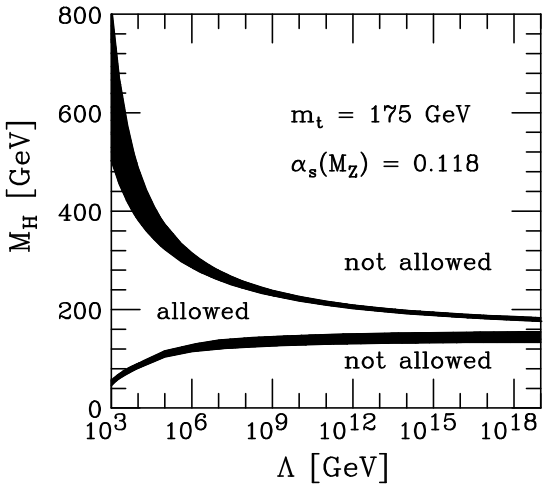

Figure 1.1: *Theoretical bounds on the Higgs mass as a function of the energy scale Λ up to which the Standard Model is valid [4].*

valid only up to $\Lambda \sim 1$ TeV, the Higgs mass can be up to 700 GeV/c^2. In any case, on the basis of these results, the guideline for the design of future colliders should be the search of the Higgs boson up to masses of the order of ≈ 1 TeV. If the Higgs particle is not found in this mass range then a more sophisticated explanation of the electroweak symmetry breaking mechanism is needed.

Experimental bounds. Experimental bounds on m_H are provided by measurements at LEP, SLC and Tevatron [5]. Direct searches [6] excluded the possibility of a Higgs boson with a mass below 114.4 GeV/c^2 at 95% confidence level. Indirect bounds can be obtained from to precision electroweak measurements; observables like the top and $W^{\pm}$ masses and Z decay parameters are logarithmically sensitive to m_H through radiative corrections. These data can therefore be fitted taking the Higgs mass as free parameter. The results of these procedure are summarized in in Fig. 1.2. The plot shows the value of $\Delta\chi^2 = \chi^2 - \chi^2_{min}$ as a function of m_H. The solid curve is the result of the fit while the shaded band represents the uncertainty due to so far not calculated higher order corrections.

The fit privileges low values of the Higgs mass and an upper limit of 166 GeV/c^2 can be set at 95% confidence level. This limit increases to 199 GeV/c^2 when including the LEP-2 direct search limit.

The Electroweak data can be also used to determine the top quark and the W masses indirectly and the results can be compared to the direct measurements performed at Tevatron and LEP-2. This is illustrated in Fig. 1.3 which also shows the SM prediction for the Higgs mass between 114 and 1000 GeV/c^2.

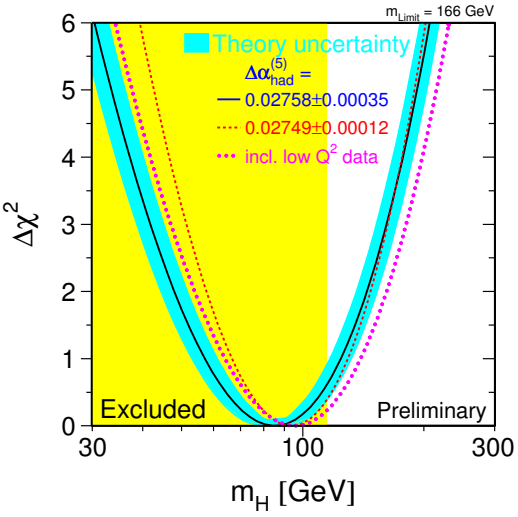

Figure 1.2: $\Delta\chi^2$ *of the fit of electroweak measurements of LEP, SLC and Tevatron as a function of the Higgs mass [5].*

The indirect and direct measurements of m_W and m_t are in good agreement. Since the accuracy on the measurement of m_W is much higher than that on m_t to further significantly constraint m_H a more accurate measurement of m_t is mandatory; to have the same weight on the Higgs mass prediction the two uncertainties should be $\Delta m_W \sim 7 \cdot 10^{-3} \Delta m_t$.

1.1.4 Open Questions

Up to now all precision measurements confirmed the SM predictions with very high accuracy. Moreover, even if the Higgs boson has never been observed, the experimental bounds on its mass are compatible with the SM being self-consistent up to the Planck scale. However, there are several reasons to think that the SM is not a fundamental theory but only an effective description at the electroweak scale ($\sim m_Z$).

We already observed that theoretical bounds on the Higgs mass can be derived from the requirement that, once radiative corrections are included, the theory remains valid up to a given energy scale Λ. It is natural to think that at higher energy scales some more general theory should be valid, possibly describing all interactions. In the Standard Model, the strong interaction is described by a SU(3) "colour" symmetry group, which however is not unified with the electroweak description. Gravity, whose strength should become comparable with that of other interactions at the Planck scale (10^{19} GeV), is not included

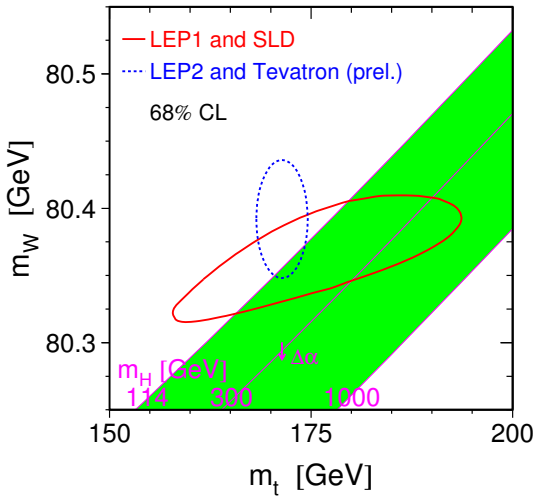

Figure 1.3: *Comparison of the indirect measurements of m_W and m_t (solid contour) and the direct measurements (dashed contour). In both cases the 68% CL contours are plotted. The Standard Model relationship for the masses as a function of the Higgs mass is also shown [5].*

at all. It would be appealing to find a wider symmetry that describes all interactions, and the reason why it is broken at the energy scales investigated up to now.

In addition, the Higgs mass suffers from divergences caused by radiative corrections which are proportional to the energy cutoff; for the Standard Model to be valid up to very high energy scales, extremely precise cancellations should be present at all perturbation levels. Such cancellations are formally possible, but such precise tuning appears to be artificial; this represents the so called *naturalness problem*.

The Higgs mechanism has been criticized also on the basis of more aesthetic considerations: it is an ad hoc addition to the SM which introduces the only scalar particle of the theory. Moreover, there is no explanation to the fact that the particle masses would be significantly smaller than the energy scale up to which the theory remains valid (*hierarchy problem*). Finally, the number of free parameters of the Standard model (17, neglecting neutrino masses and mixings) appears too high for a fundamental theory.

Several solutions for these problems have been proposed. Among them, supersymmetry (SUSY) is an elegant theory that introduces a new symmetry between bosons and fermions. SUSY predicts that each particle has a super-

symmetric partner whose spin differs by one half. The naturalness problem is solved by the fact that the loop contributions from particles and their supersymmetric partners cancel. The simplest supersymmetric model, called the Minimal Supersymmetric Standard Model (MSSM), requires at least two Higgs doublets, corresponding to five Higgs particles: two charged bosons, $H^{\pm}$, two scalar bosons, h and H, and one pseudo-scalar, A. The MSSM predicts a rich phenomenology to appear below energies of about 1 TeV; however no evidence for supersymmetry has been observed yet.

1.2 The Large Hadron Collider

1.2.1 Design of the LHC

In the previous section it has been explained that new physics is expected to appear at the TeV scale with the interesting processes characterized by extremely low cross sections. The LHC is the accelerator machine designed to investigate those phenomena.

LHC is a proton-proton collider which will collide beams at 14 TeV centre-of-mass energy and very high luminosity ($10^{34}\text{cm}^{-2}\text{s}^{-1}$).

The choice of proton beams is mainly dictated by the following considerations:

- hadrons allow to explore a wide range of energies with fixed-energy beams: they are the natural choice for a discovery machine. This is because of the fact that protons are not elementary particles, and in hard collisions the interaction involves their constituents (quarks and gluons), which carry only a fraction of the proton energy.

- protons due to their higher mass imply a smaller energy loss for synchrotron radiation with respect to electrons. In a circular collider of radius R, the energy loss per turn due to synchrotron radiation is proportional to $(E/m)^4/R$, where E and m are respectively the energy and mass of the particles accelerated.

Since only a fraction of the proton energy contributes to the hard scattering, the centre-of-mass energy of the beams must be much higher than the mass of the particle that has to be produced. The cross section for different processes as a function of the centre-of-mass energies in p-p collisions is shown in Fig. 1.4. It can be noted that the Higgs cross section increases steeply with the centre-of-mass energy, while the total cross section (*i.e.* the background) remains almost constant. It is clear that the highest centre-of-mass energy should be used. The idea behind the Large Hadron Collider is to reuse the existing 27 km

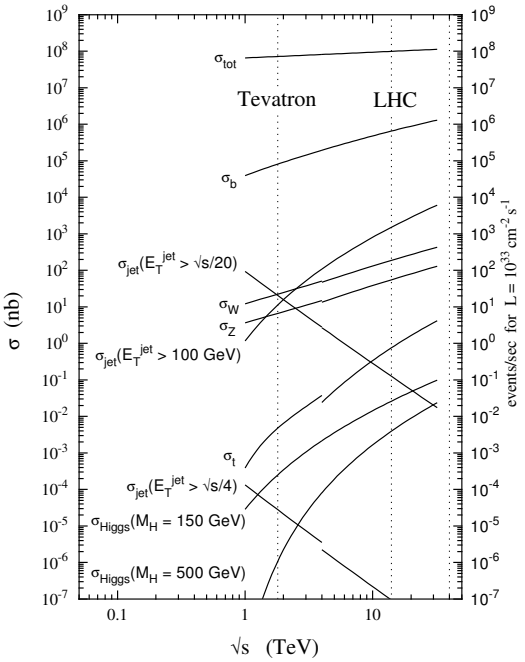

Figure 1.4: *Expected cross sections and event rates of several processes as a function of the centre-of-mass energy of proton-proton collisions [7].*

long LEP tunnel to install a new p-p collider. Considerable financial savings are obtained from the fact that the tunnel and several infrastructures (including pre-accelerators) already exist. However, the size of the tunnel limits the centre-of-mass energy to 14 TeV, since the beams must be bent by dipole magnets whose maximum field is currently limited at about 8 T.

The event rate R of a given process with cross section σ is given by:

$$R = \mathcal{L}\sigma \tag{1.11}$$

where the factor $\mathcal{L}$ is the luminosity which represents the number of collisions per unit time and cross-sectional area of the beams. It is specific to the collider parameters and does not depend on the process considered:

$$\mathcal{L} = f\frac{n_1 n_2}{A}. \tag{1.12}$$

Here f is the collision frequency of bunches composed of n_1 and n_2 particles and A is the overlapping cross-sectional area of the beams.

To compensate for the low cross section of the interesting processes the LHC must have a very high luminosity: it will operate at a bunch crossing rate of 40 MHz and a design luminosity of $10^{34}\mathrm{cm}^{-2}\mathrm{s}^{-1} = 10\ \mathrm{nb}^{-1}\mathrm{s}^{-1}$. The bunch structure is such that only about 80% of the bunches will be filled [8].

Table 1.3: *LHC parameters for p-p and Pb–Pb collisions.*

Parameter	*p-p*	$^{208}Pb^{82+}$
Centre-of-mass energy (TeV)	14	1148
Number of particles per bunch	1.1×10^{11}	$\sim 8\times10^{7}$
Number of bunches	2808	608
Design Luminosity ($cm^{-2}s^{-1}$)	10^{34}	2×10^{27}
Luminosity lifetime (h)	10	4.2
Bunch length (mm)	53	75
Beam radius at interaction point (μm)	15	15
Time between collisions (ns)	24.95	124.75×10^{3}
Bunch crossing rate (MHz)	40.08	0.008
Circumference (km)	26.659	
Dipole field (T)	8.3	8.3

This design has the drawback that the total event rate becomes so high that several interactions overlap in the same bunch crossing (*pile up*). Given that the total non-diffractive inelastic *p-p* cross section predicted by PYTHIA is 55 mb, on average 17.3 events will occur at every bunch crossing. With about 50 charged tracks per interaction, this pile-up poses several experimental problems, as discussed in Section 1.2.3.

The first beam is foreseen by the end of 2007 and it will be a commissioning run at reduced centre-of-mass energy of 900 GeV. The first collisions at 14 TeV centre-of-mass energy are planned for the second half of 2008. The operation will start at 75 ns bunch spacing and subsequently the design 25 ns spacing will be reached. During the first year of physics running the LHC should reach the peak luminosity of $2 \times 10^{33}cm^{-2}s^{-1}$ while the design luminosity of $10^{34}cm^{-2}s^{-1}$ should be reached within the fourth year of operation. These two luminosity regimes are commonly called "High luminosity" and "Low Luminosity", respectively. The LHC will also be able to accelerate and collide beams of heavy ions such as Pb to study the de-confined state of matter, the quark-gluon plasma. The parameters of the LHC are summarized in Table 1.3.

1.2.2 Phenomenology of Proton-Proton Collisions

Protons are not elementary particles, and in high-energy inelastic proton-proton collisions the interaction involves the partons (quarks and gluons) inside the proton. The effective centre-of-mass energy of the hard scattering, $\sqrt{\hat{s}}$, is therefore proportional to the fractional energies x_a and x_b carried by the two interacting partons: $\sqrt{\hat{s}} = \sqrt{x_a x_b s}$, where $\sqrt{s}$ is the centre-of-mass energy of the proton

beams.

The momentum distribution of the partons inside the proton are called Parton Density Functions (PDFs). They are different for gluons, u and d valence quarks and low-momentum quark-antiquark pairs of all flavours produced and annihilated as virtual particles (sea quarks). They are functions of the exchanged four-momentum squared, Q^2, since for higher exchanged momenta a shorter distance scale is probed and the contribution of gluons and sea quarks becomes higher. PDFs are obtained from experimental data covering the widest possible range of (x, Q^2); their accuracy is important for several precision measurements. In Fig. 1.5, the CTEQ4M PDFs [9] at two different values of Q^2 are shown.

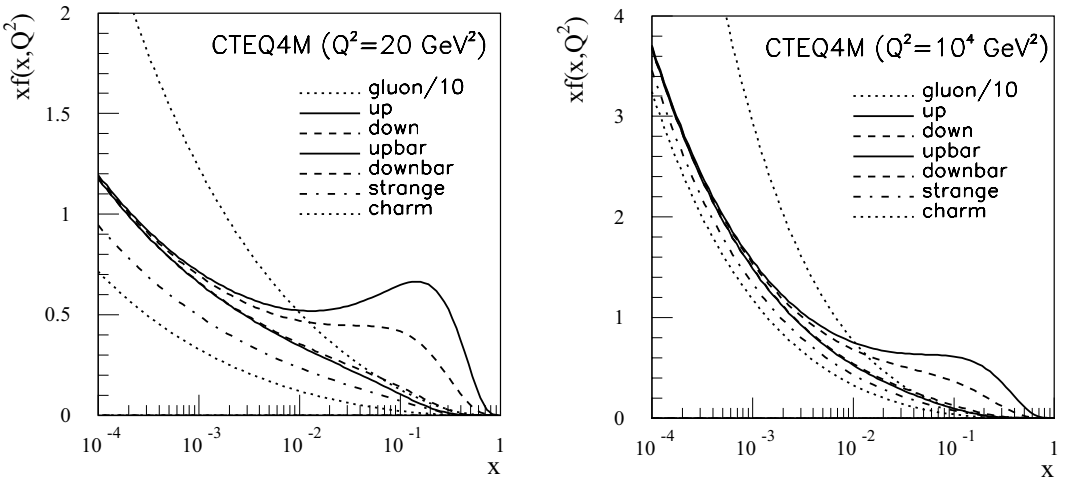

Figure 1.5: *Parton density functions for $Q^2 = 20$ GeV/c^2 and $Q^2 = 10^4$ GeV/c^2 [10].*

The fact that the two partons interact with unknown energies has two fundamental consequences. First of all the total energy of an event is unknown, because the proton remnants, that carry a sizeable fraction of the proton energy, are scattered at small angles and are predominantly lost in the beam pipe, escaping detection. Experimentally, it is therefore not possible to define the total and missing energy of the event, but only the total and missing transverse energies (in the plane transverse to the beams). Moreover, the centre of mass may be boosted along the beam direction. It is therefore very useful to use experimental quantities that are invariant under such boosts as the transverse momentum p_T or the *rapidity*. The rapidity, choosing the beam direction as z axis, is defined as:

$$y = \frac{1}{2} \ln \frac{E + p_z}{E - p_z} \tag{1.13}$$

and it is often used to describe angular distributions because it has the property that the shape of dN/dy distributions is invariant under boosts along the z direction. For utrarelativistic particles ($p \gg m$) the rapidity is approximated by the *pseudorapidity*:

$$\eta = -\ln \tan \frac{\theta}{2}, \tag{1.14}$$

where θ is the angle between the particle momentum and the z axis. The pseudorapidity can be reconstructed just from the measurement of the θ angle and can be also used for particles for which the mass and momentum are not measured.

One very remarkable aspect of LHC physics is the wide cross section range of the processes under investigation: in Fig. 1.4 we see for example that the Higgs production has a cross section at least ten orders of magnitude smaller than the total inelastic cross section. In fact, the bulk of the events produced in proton-proton collisions is either due to low-$\hat{p}_T$ scattering, where the protons collide at large distances, or to QCD high-$\hat{p}_T$ processes of the type:

$$\begin{cases} q_i\bar{q}_i \rightarrow q_k\bar{q}_k \\ q_iq_j \rightarrow q_iq_j \\ q_ig \rightarrow q_ig \\ q_i\bar{q}_i \rightarrow gg \\ gg \rightarrow q_k\bar{q}_k \\ gg \rightarrow gg \end{cases}$$

All these events are collectively called "minimum bias" and in LHC studies are in general considered uninteresting since they constitute a background for other processes, where massive particles like the Higgs are created in the hard scattering. This classification is somewhat arbitrary; for example, this definition of minimum bias events includes $b\bar{b}$ production that is of interest for b-physics studies.

1.2.3 LHC Experiments

LHC detectors will operate in a very difficult environment: the high bunch crossing frequency, the high event rate and the pile-up of several events in the same bunch crossing dictate strict requirements on the design of detectors. To cope with a bunch crossing rate of 25 ns and a pile-up of about 20 events per crossing, the detectors should have a very fast time response and the readout electronics should also be very fast. Due to the presence of pile-up, high granularity is also required to avoid the overlap of particles in the same sensitive elements. High granularity means a large number of electronics channels, and therefore high cost. LHC detectors will also have to stand an extremely high radiation dose; special radiation-hard electronics must be used.

Additional requirements apply to the on-line trigger selection, that has to deal with a background rate several orders of magnitude higher than the signal rate. These requirements are discussed in Section 2.5.

Four experiments will be installed at the LHC. Two of them are devoted to specific topics: Alice to heavy ions and LHC-b to b-physics. The other two are the general-purpose experiments ATLAS and CMS. Their design differs significantly, since two very different solutions were chosen for the configuration of magnetic field: CMS uses a solenoidal field generated by a big superconducting solenoid, while ATLAS uses a toroidal field produced by three sets of air-core toroids complemented by a small inner solenoid. A detector based on a toroidal magnet has the advantage that the track p_T resolution is constant as a function of pseudorapidity. A very large air-core toroid allows a good momentum resolution even without the aid of the inner tracker; however, it requires very precise detectors with excellent alignment. An iron-core solenoid, on the other hand, can generate a very intense field. The resulting system is very compact and allows calorimeters to be installed inside the magnet, improving the detection and energy measurement of electrons and photons. Precise tracking exploits both the constant field within the magnet and the field inside the return yoke. Moreover, tracks exiting the yoke point back to the interaction point, a property that can be used for track reconstruction. Multiple scattering within the yoke, however, degrades the resolution of the muon system.

Schematic pictures of CMS and ATLAS are shown in Fig. 1.6 and Fig. 1.7, respectively. The CMS experiment is described in detail in Chapter 2.

1.3 Physics with the LHC

Thanks to its high centre-of-mass energy and high luminosity, the LHC has a significant physics potential not only for the discovery of the Higgs, but also in many other fields like electroweak precision measurements, searches and b-physics. In this section, an overview of the LHC physics programme is given.

1.3.1 Higgs Search

The main processes which contribute to the Higgs production at LHC are shown in the diagrams in Fig. 1.8. The cross sections for these different processes as a function of m_H are shown in Fig. 1.9. Gluon fusion is the dominant process on the whole m_H spectrum and only at very high Higgs masses does the vector boson fusion become comparable. However, even if the WW scattering has on average a cross section about 5 to 10 times smaller than that of gluon-gluon fusion, this channel is extremely promising thanks to its clean experimental signature; the presence of two spectator jets provides a powerful tool to tag

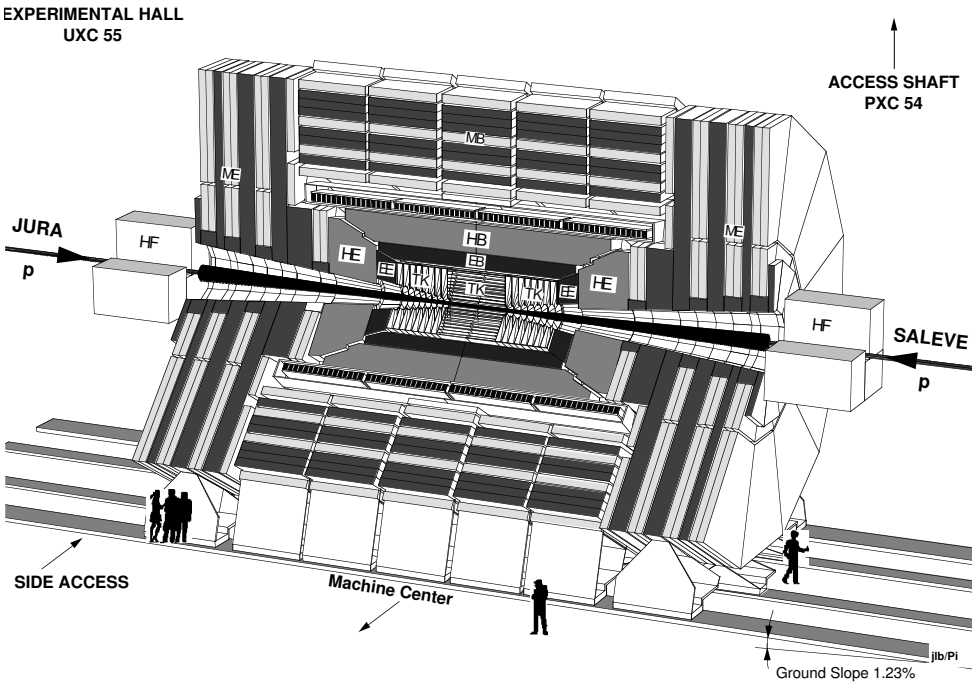

Figure 1.6: *The CMS detector.*

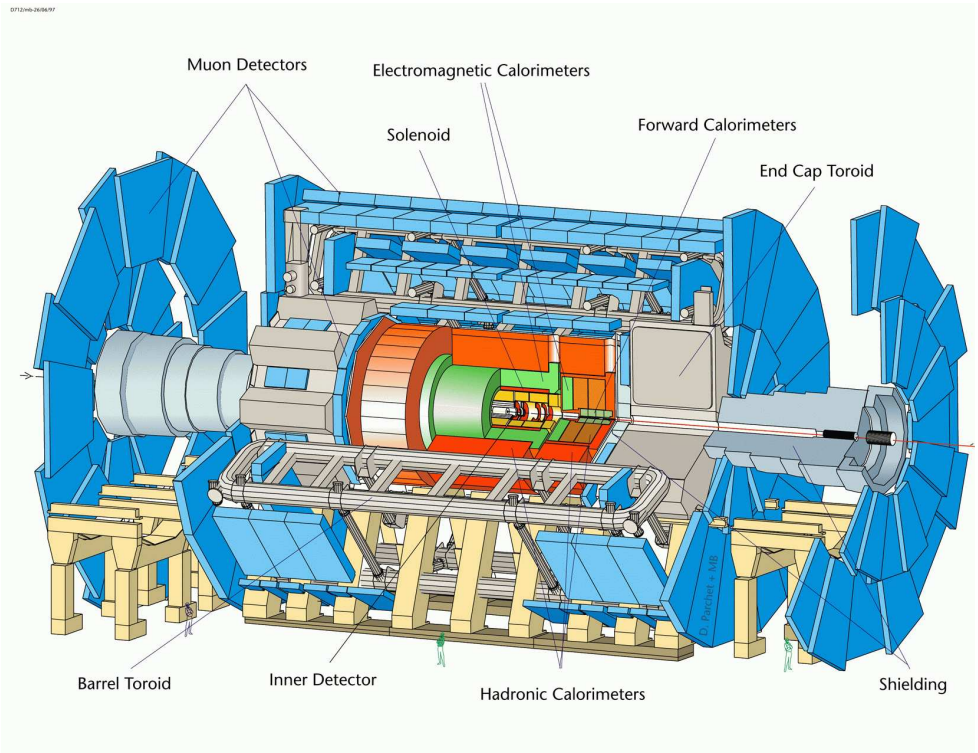

Figure 1.7: *The ATLAS detector.*

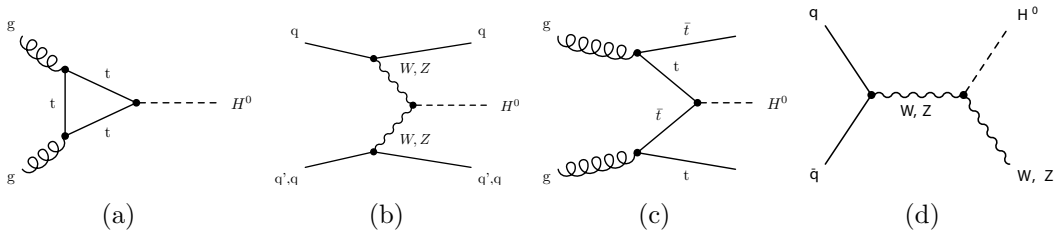

Figure 1.8: *Higgs production mechanisms at tree level in proton-proton collisions: (a) Gluon-gluon fusion; (b) W and Z fusion; (c) $t\bar{t}$ associated production; (d) W and Z associated production.*

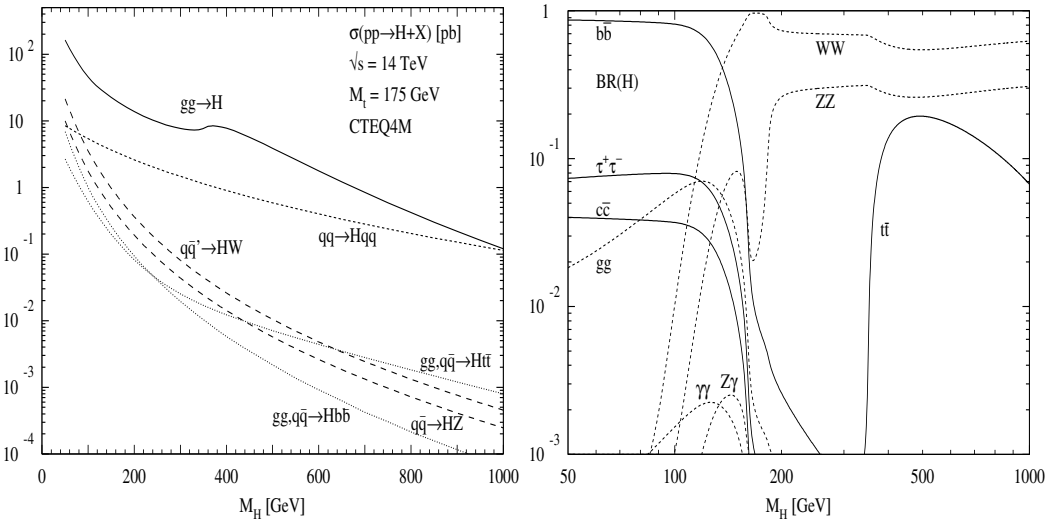

Figure 1.9: *Higgs production cross section (left) and branching ratios (right) as a function of the Higgs mass [11].*

the signal events discriminating the backgrounds. The associated production channels $q_i\bar{q}_j \rightarrow WH$ or $q_i\bar{q}_j \rightarrow ZH$, where an off-shell boson is produced and radiates a Higgs, have very small cross sections, except for very low m_H. Also the production mechanism $gg, q_i\bar{q}_j \rightarrow t\bar{t}H$ has a cross section almost 100 times smaller than that of gluon-gluon fusion. However, also in this case a powerful signature is given by the additional bosons or quarks in the final state.

Cross sections are typically of the order of few picobarns, which at the LHC design luminosity correspond to rates of about 10^{-2} Hz. However, not all final states will be experimentally accessible, and the branching ratios of the observable channels are usually small.

The branching ratios for several Higgs decay channels as a function of the Higgs mass are shown in Fig. 1.9. They can be interpreted on the basis of the

Higgs couplings to fermions and gauge bosons:

$$g_{Hff} = \frac{m_f}{v} \tag{1.15}$$

$$g_{HWW} = \frac{2m_W^2}{v} \tag{1.16}$$

$$g_{HZZ} = \frac{m_Z^2}{v}. \tag{1.17}$$

The coupling is proportional to the fermion masses and to the square of the boson masses; therefore the final state with the heaviest available particle dominates:

- low Higgs masses ($m_H < 130$ GeV/c^2): the heaviest available fermion is the b quark, and $H \to b\bar{b}$ dominates. However, this decay channel could be difficult to observe at the LHC because of the huge QCD background (except maybe by exploiting associated $t\bar{t}H$ or WH production). In this mass region the most promising channel is $H \to \gamma\gamma$, which despite the very low branching ratio ($\sim 10^{-3}$) has a very clean signature. The signal should appear as a narrow peak over the continuum $(q\bar{q}, gg) \to \gamma\gamma$ background, but excellent photon energy and angular resolution are required as well as good π^0 rejection;

- intermediate Higgs masses (130 GeV/$c^2 < m_H \lesssim 500 - 600$ GeV/c^2): the production of WW and ZZ pairs becomes possible; the branching ratio is high, but purely hadronic final states are again not accessible. $H \to 4\ell$ is the "golden-plated" channel for Higgs search; however it has very low branching ratio and suffers from the low Higgs production cross sections above $m_H \sim 600$ GeV/c^2. The channel $H \to WW$ has the disadvantage that experimentally accessible final states $(\ell\mu\ell\mu, \ell\nu jj)$ have at least one neutrino that escapes detection; however it will be a good discovery channel, especially for $m_H \approx 2m_W$ where the WW production is at threshold and the ZZ branching ratio drops to 20%;

- very high Higgs masses (above 500 GeV/c^2): the cross section becomes low and semi-hadronic final states $(2\ell 2j, \ell\nu 2j)$ have to be used. The Higgs width becomes also very broad, as shown in Fig. 1.10, so that the reconstruction of a mass peak becomes difficult.

1.3.2 Electroweak Physics

Several precision electroweak measurements will be possible with the two experiments ATLAS and CMS. Thanks to the high statistics available (*e.g.*

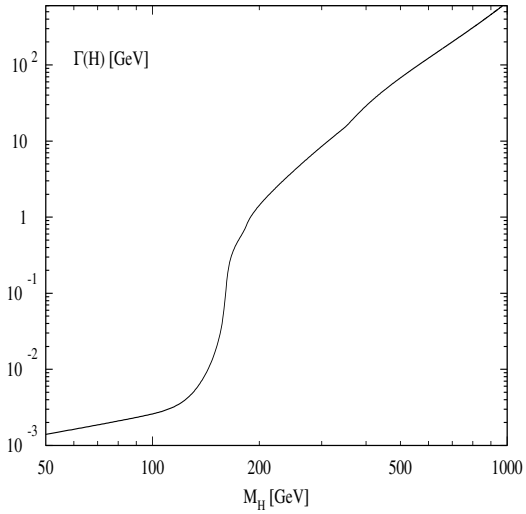

Figure 1.10: *Higgs width as a function of its mass [11].*

10^8 $W \to e\nu$ decays, 10^7 $t\bar{t}$ pairs produced in the first year of operation), for most measurements the statistical uncertainty will be very small. High statistics control samples will allow a good understanding of the detector response, thus reducing the systematic uncertainty.

In the following, we shortly discuss the experimental challenges of some electroweak measurements to be performed at LHC. A more comprehensive discussion can be found elsewhere [7, 12].

1.3.2.1 Measurement of the W and Top Mass

As already discussed in Section 1.1.3, the values of the top and Higgs masses enter in the prediction of the W mass through radiative corrections. Precise measurements of m_t and m_W allow therefore to set limits on m_H and, if the Higgs is found, they will allow stringent tests of the Standard Model (SM) or its extensions like the Minimal Supersymmetric Standard Model (MSSM).

The most promising channel for the measurement of the top mass is $t\bar{t} \to W^+W^-b\bar{b}$ with one leptonic and one hadronic W decay, where the hadronic part is used to reconstruct the top mass and the leptonic part to select the event. The main source of uncertainty will be the jet energy scale, which is affected by the knowledge of fragmentation and gluon radiation and of the response of the detectors. The same sample of $t\bar{t}$ events will provide a large number of hadronic W decays to be used for the calibration of the hadron calorimeters.

The final uncertainty on m_t will be better than about 2 GeV. This will allow to constrain the Higgs mass to better than 30% but, in order not to become the dominant source of uncertainty, the W mass will have be measured with a

precision of about 15 MeV.

Since the longitudinal component of the neutrino momentum cannot be measured in hadron colliders, the W mass is obtained from a fit to the distribution of the W transverse mass. The main source of uncertainty is the lepton energy and momentum scale, which should be known with a precision of $\sim 0.02\%$ to achieve the mentioned precision on m_W. This is a challenging goal that at LHC could be reached thanks to the high statistics of $Z \to \ell\ell$ decays. Other sources of systematic uncertainty include the W p_T spectrum, the W width and the proton structure functions. Since pile-up deteriorates the shape of the W transverse mass distribution, this measurement will probably be feasible only in the low luminosity mode.

1.3.2.2 Drell-Yan Production of Lepton Pairs

The Drell-Yan production of lepton pairs is a process with clean signature and low experimental backgrounds. The interesting quantities are the cross section and the forward-backward asymmetry, both functions of the rapidity y and of the invariant mass $m_{\ell\ell}$ of the di-lepton system.

The measurement of the cross section can provide evidence for new physics (new resonances, contact terms etc.) and probe electroweak radiative corrections up to 1.5 TeV. The main issue in this measurement is the knowledge of the absolute luminosity which should reach a precision of 5%, an ambitious goal requiring theoretical improvements in the knowledge of the W and Z production cross section.

The measurement of the forward-backward asymmetry $\mathrm{A_{FB}}$ allows the determination of the effective electroweak mixing angle $\sin^2\theta^{lept}_{eff}$. However, it requires the knowledge of the incoming quark and anti-quark direction, which in p-p colliders is difficult to determine and is affected by the uncertainty on parton density functions. Improving the LEP+SLD accuracy on $\sin^2\theta^{lept}_{eff}$ is therefore a very ambitious goal. Preliminary studies indicate that it might be possible to achieve it if the geometrical acceptance for electrons is extended up to $|\eta| < 4.9$ using the forward calorimeters.

1.3.2.3 Production of Vector Boson Pairs

At the lowest order vector boson pairs are produced in $q\bar{q}$ annihilations followed by triple gauge boson vertices. Triple Gauge Couplings (TGC) allow to test directly the non-Abelian gauge symmetry of the SM. They are described by five parameters, which can be measured with fits to the total cross sections and shapes of distributions such as that of $p_T^{\gamma,Z}$ in Wγ and WZ events. Deviations from the SM values can provide evidence for new physics, *e.g.* the presence of new heavy particles decaying to WW and ZZ pairs (including heavy

Higgs). Anomalous couplings are present in many extensions of the SM, including MSSM, technicolour etc. Since the sensitivity to anomalous couplings is enhanced at high centre-of-mass energies, LHC is expected to increase significantly the precision on TGC parameters.

At high energy, the process of vector boson scattering becomes dominant. This process is particularly sensitive to the electroweak symmetry breaking mechanism since the cross section for the scattering of longitudinally polarized vector bosons violates unitarity at a scale of ~ 1 TeV. In the SM, this is cured with the introduction of the Higgs boson; in the absence of the Higgs new physics must appear in this channel. Whatever the scenario will be, vector boson scattering will therefore probe the mechanism of electroweak symmetry breaking. It is thus important to measure the WW scattering cross section as a function of the invariant mass of the WW system up to a scale of ~ 1 TeV.

From the experimental point of view, one can exploit the presence of the two quarks emitting the incoming bosons by requiring the signature of forward tagging jets. Other selection criteria are similar to those used for heavy SM Higgs searches. Again purely hadronic final states will not be accessible due to the high QCD background; on the other hand it will be useful to reconstruct the invariant mass of the final state boson-boson system also in the absence of a resonance, which is not possible in final states with more than one neutrino.

High integrated luminosities will be necessary for these studies, due to the small cross sections and branching ratios and the high background rates.

1.3.3 Other Physics Studies

Supersymmetry. As already discussed, the simplest supersymmetric model, the Minimal Supersymmetric Standard Model (MSSM), predicts the existence of five Higgs bosons: two charged bosons, $H^{\pm}$, two scalar bosons, h and H, and one pseudo-scalar, A. At tree level, all masses and couplings depend on two parameters, chosen as the mass of the A boson, m_A, and the ratio of the vacuum expectation values of the two Higgs doublets, $\tan\beta$. In most of the parameter space, charged Higgs bosons decay predominantly to $\tau\nu$. For the neutral Higgs bosons, the decays to vector bosons are suppressed, so that the golden channels described for the case of a SM Higgs will not be observable. The dominant decays modes are those to $b\bar{b}$ and $\tau^+\tau^-$ [11], but the former is hidden by the large background of b-jets. The observation of MSSM Higgs bosons will therefore rely on the identification the leptons coming from τ decays and of τ-jets.

Additionally, supersymmetric theories predict a rich phenomenology. In general supersymmetric particles should be accessible at LHC energies and have very spectacular signatures due to cascade decays with many leptons and jets in the final state and large missing energy. If supersymmetry exists, LHC

experiments will certainly be able to observe and study it.

B-Physics. In the field of b-physics, LHC will benefit from a very large $b\bar{b}$ production cross section (see Fig. 1.4). The main interest is the study of the decays of neutral B mesons, and in particular of CP violation in the $B_d^0 - \bar{B}_d^0$ and $B_s^0 - \bar{B}_s^0$ systems. B decays can be identified in leptonic final states, especially in the case of muons. However these leptons are usually soft and the identification is difficult due to the high backgrounds and pile-up. One LHC experiment, LHCb, will be dedicated to b-physics, which will be studied also by ATLAS and CMS will in the low-luminosity phase. At high luminosity, the luminosity in the LHCb collision point will be reduced by de-tuning the beams.

Heavy ions. As already mentioned, LHC will also operate as a collider of heavy ions, with an energy 30 times higher than that that of RHIC, today's most powerful ion collider. Heavy ions collisions will be studied with a dedicated detector, Alice, but also with Atlas and CMS. The goal is to investigate the de-confined state of matter, the quark-gluon plasma.

Chapter 2

The CMS Detector

The Compact Muon Solenoid (CMS) [13] is a general-purpose experiment that will operate at the Large Hadron Collider. The first collisions are expected for the second half of 2007 and the detector is currently being installed and commissioned.

The CMS design was driven by the requirements of a robust and redundant muon system, a precise electromagnetic calorimetry, and a high quality central tracking. To achieve these goals maintaining a compact design a strong magnetic field was chosen. The 4 T magnetic field provides a large bending power, needed for a precise measurement of the muon momentum, and reduces the pile-up from soft hadrons in the muon system installed inside the return yoke.

This chapter describes the general design of CMS with emphasis on the muon spectrometer.

2.1 Overall Design

The layout of CMS is illustrated in Fig. 2.1. The detector consists of a cylindrical barrel closed by two endcap disks. The overall length is 21.6 m, the diameter 14.6 m and the total weight about 12500 tons.

The CMS coordinate system is a right-handed frame where the x axis points to the center of the LHC ring, the y axis points upward and the z axis is parallel to the beam. However, reconstruction algorithms use a cylindrical coordinate system based on the distance r from the z axis, the azimuthal angle ϕ with respect to the y axis and the pseudorapidity η.

The longitudinal view of one quarter of the CMS detector is shown in Fig. 2.2. The transverse view of the barrel region is shown in Fig. 2.3. Components are indicated with standard two-letter codes (the second being `B` for barrel and `E` for endcap) which will be used in the following.

The core of the apparatus is the magnet (`CB`), a 13 m long superconductive

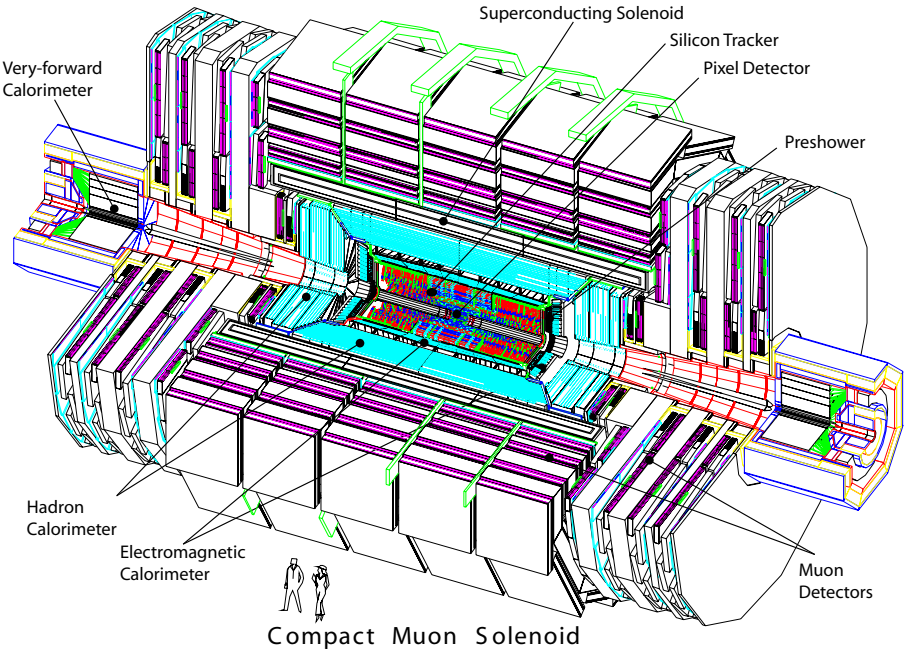

Figure 2.1: *The CMS detector.*

solenoid [14] cooled with liquid helium, which will provide a 4 T magnetic field. The iron return yoke of the magnet (YB, YE) hosts the muon spectrometer, composed by 4 stations of drift tube detectors (DT) in the barrel region (MB) and 4 stations of cathode strip chambers (CSC) in the endcaps (ME). Both the barrel and the endcaps are instrumented with resistive plate chambers (RPCs) to ensure redundancy and robustness to the muon trigger. The overall pseudorapidity coverage of the muon system goes up to $|\eta| < 2.4$. The muon spectrometer is described in detail in Section 2.4.

The magnet coil has a radius of 5.9 m and houses the tracker and the calorimeters. The tracking detector is a cylinder of length 5.8 m and diameter 2.6 m. Its design is leaded by the requirement of a precise vertex reconstruction and a reliable b-tagging with very high track multiplicity. To cope with this goal very fine segmentation is crucial; CMS employs 10 layers of silicon microstrip detectors, which provide the required granularity and precision. In addition, 3 layers of silicon pixel detectors are placed close to the interaction region to improve the measurement of the impact parameter of charged-particle tracks, as well as the position of primary and secondary vertices. This tracking device allows charged tracks reconstruction with at least 12 measurement points and a coverage of $|\eta| < 2.5$.

The electromagnetic calorimeter (ECAL) is a homogeneous calorimeter

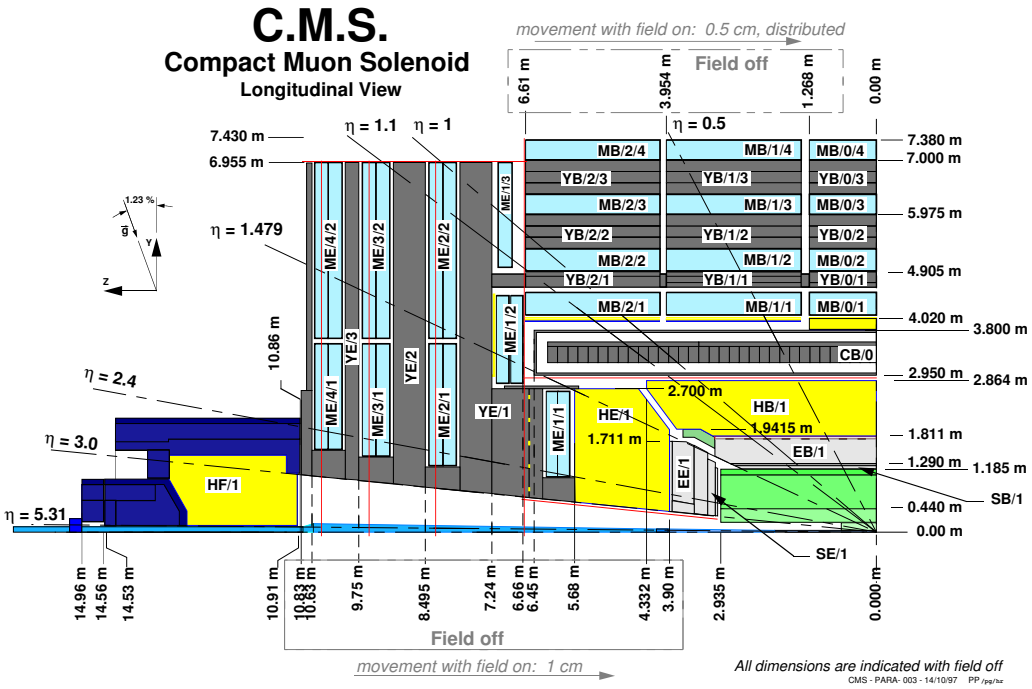

Figure 2.2: *Longitudinal view of one quarter of the CMS detector.*

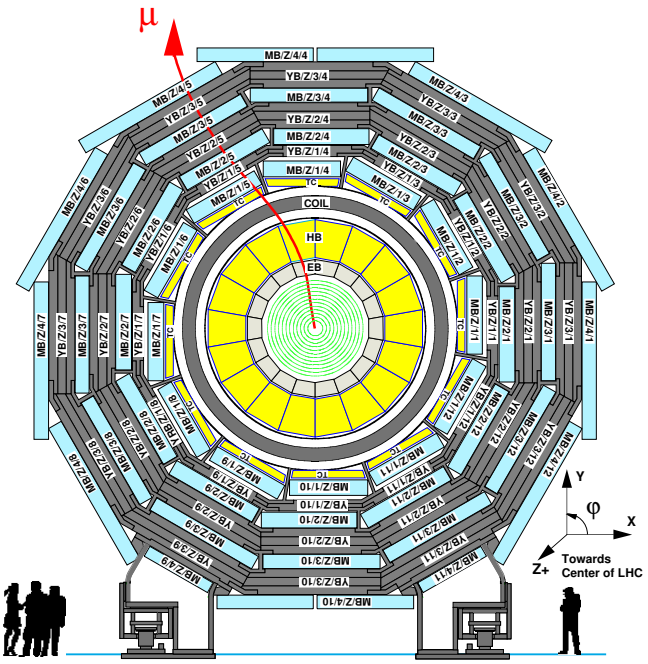

Figure 2.3: *Transverse view of the barrel region of the CMS detector. Barrel wheels are numbered Z = -2, -1, 0, 1, 2.*

made of lead tungstate ($PbWO_4$) scintillating crystals. The scintillation light is detected by silicon avalanche photodiodes (APDs) in the barrel region (EB) and vacuum phototriodes (VPTs) in the endcap region (EE). The pseudorapidity coverage extends up to $|\eta| = 3.0$. In the endcaps a lead/silicon pre-shower detector is installed to improve the resolution on electron and photon direction and help pion rejection.

Outside ECAL the hadronic calorimeter (HCAL) is installed. It is a brass/scintillator sampling calorimeter. In the central part, the HCAL is complemented by a "tail-catcher" ensuring that hadronic showers are sampled with nearly 11 hadronic interaction lengths. The barrel and endcap parts (HB,HE) have the same $|\eta|$ coverage as the ECAL, and are complemented by a very forward calorimeter (HF), which extends the coverage up to $|\eta| < 5.3$, enhancing the hermeticity of the detector and its ability to measure missing transverse energy.

2.2 The Inner Tracking System

The inner tracker [15, 16] is designed to reconstruct high-p_T charged tracks in the region $|\eta| < 2.5$ with high efficiency and good momentum resolution, to measure their impact parameter and to reconstruct secondary vertices. To achieve this goal several layers of silicon detectors are employed. In the innermost region pixel detectors are used. Thanks to their high granularity pixels are particularly suited for working with the very high particle flux and their good three-dimensional spatial resolution is crucial for the measurement of the impact parameter. The rest of the tracker is composed by single-sided and double-sided silicon strip detectors covering up to $r = 110$ cm and $|z| = 270$ cm.

The performance of the tracker is illustrated in Fig. 2.4, which shows the transverse momentum and impact parameter resolutions in the r-ϕ and r-z planes for single muons with a p_T of 1, 10 and 100 GeV/c, as a function of pseudorapidity. The resolution on the p_T measurement remains well below 2% up to $\eta = 1.6$.

2.2.1 The Pixel Detector

The detector consists 4.4 millions of n-type silicon pixels with a size of 100 μm $\times$ 150 μm on a n-type silicon substrate. The sensors are read-out analogically and a spatial resolution of $\sim$ 10 μm for the r-ϕ coordinate and $\sim$ 20 μm for the r-z measurement is achieved interpolating the charge induced in nearby pixels, helped by the large Lorentz drift angle in the magnetic field. The charge sharing is enhanced in the endcaps, where the electric and magnetic fields are parallel, by tilting the detectors by 20°.

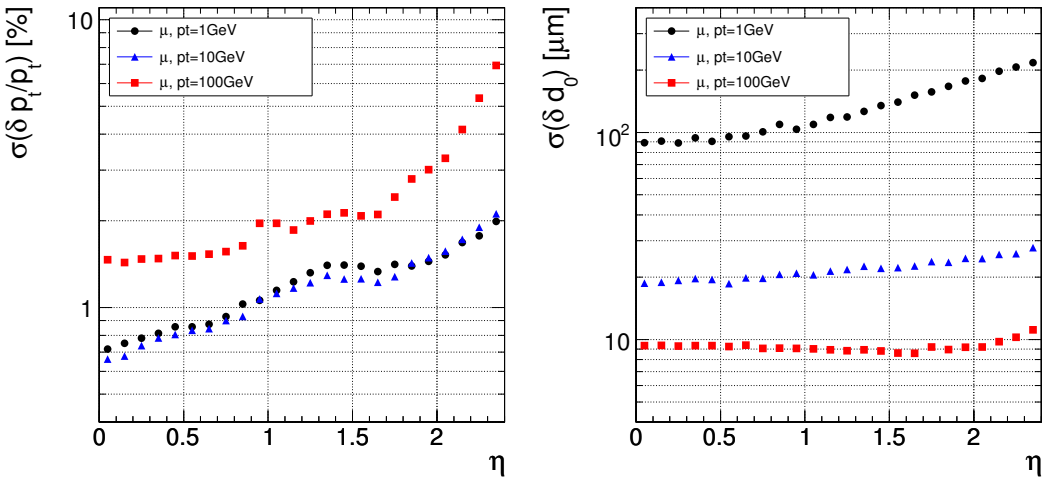

Figure 2.4: *Resolution of the tracker on the transverse momentum (left) and the transverse impact parameter (right) as a function of pseudorapidity, for single muons with transverse momentum of 1, 10 and 100 GeV/c [1].*

The sensors will be organized in three barrel layers at mean radii of 4.4 cm, 7.3 cm and 10.2 cm, extending for a total length of 53 cm. In the endcaps two disks will be placed at $z = 34.5$ cm and 46.5 cm extending in radius from 6 to 15 cm. The layout of the pixel detector is shown in Fig. 2.5. The pixel detector is designed to provide at least two hits for tracks originating within $2\sigma_Z$ [1] from the nominal interaction point up to about $|\eta| < 2.2$. Moreover, standalone track reconstruction which requires three hits per track will also be possible with good efficiency in the same region.

The three-dimensional resolution of the pixels will play a key role in the identification of b and τ-jets allowing the accurate measurement of the impact parameter and the reconstruction primary and secondary vertices.

The short distance from the interaction point will impose special requirements on radiation hardness and will probably require the substitution of the pixel detector during the lifetime of the experiment.

In the initial phase no pixels will be installed with the plan to install only two barrel layers and one end-cap disk in the first low-luminosity data taking. With this layout standalone track reconstruction will not be feasible and the region where two hits can be reconstructed is limited to $|\eta| < 2.0$.

[1] Longitudinal size of the luminosity region of the LHC beam: $\sigma_Z \sim 5$ cm.

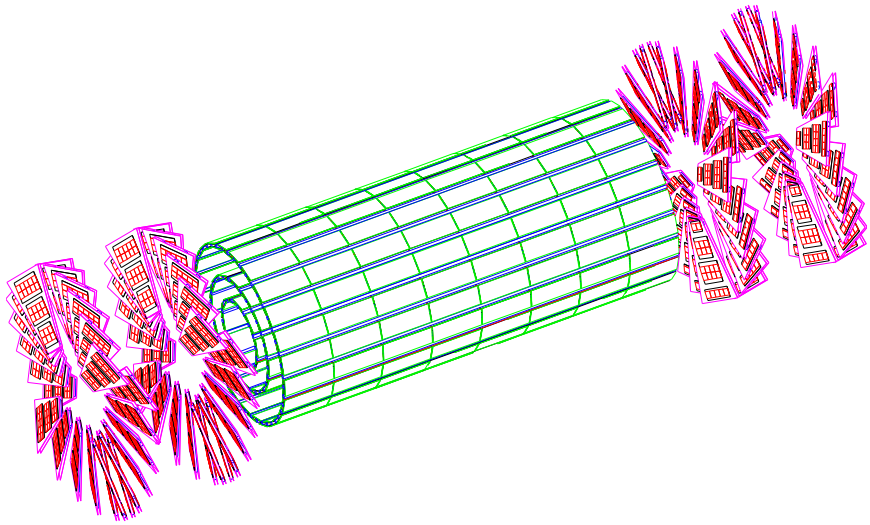

Figure 2.5: *Three-dimensional view of the full pixel detector.*

2.2.2 The Silicon Microstrip Detector

In addition to the pixel detectors, the tracker is composed of several layers of silicon microstrip detectors, whose layout is shown in Fig. 2.6. The barrel region is divided into two parts: a TIB (Tracker Inner Barrel) and a TOB (Tracker Outer Barrel). The TIB is composed by four layers of n-type silicon sensors with a thickness of 320 μm and strip pitches varying from 80 to 120 μm. The first two layers are made with double-sided ("stereo") modules, composed by two detectors mounted back-to-back with the strips rotated by 100 mrad. This kind of sensors provides a measurement in both r-ϕ and r-z coordinates with a single point resolution between 23-34 μm and 230 μm respectively. The TOB is constituted of six layers. In this region the radiation levels are smaller and thicker silicon sensors (500 μm) can be used to maintain a good S/N ratio for longer strip length and wider pitch. The strip pitch varies from 120 to 180 μm. Also for the TOB the first two layers provide a "stereo" measurement with a single-point resolution varies from 35 to 52 μm in the r-ϕ direction and 530 μm in z.

The endcaps are divided into the TID (Tracker Inner Disks) and TEC (Tracker End Cap). The three disks of the TID fill the gap between the TIB and the TEC while the TEC comprises nine disks that extend into the region 120 cm $< |z| <$ 280 cm. Both parts are composed of wedge shaped modules arranged in rings, centered on the beam line, and have strips that point towards the beam line. The modules mounted on the first two rings of the TID, on the innermost two rings and on the fifth ring of the TEC are double-sided.

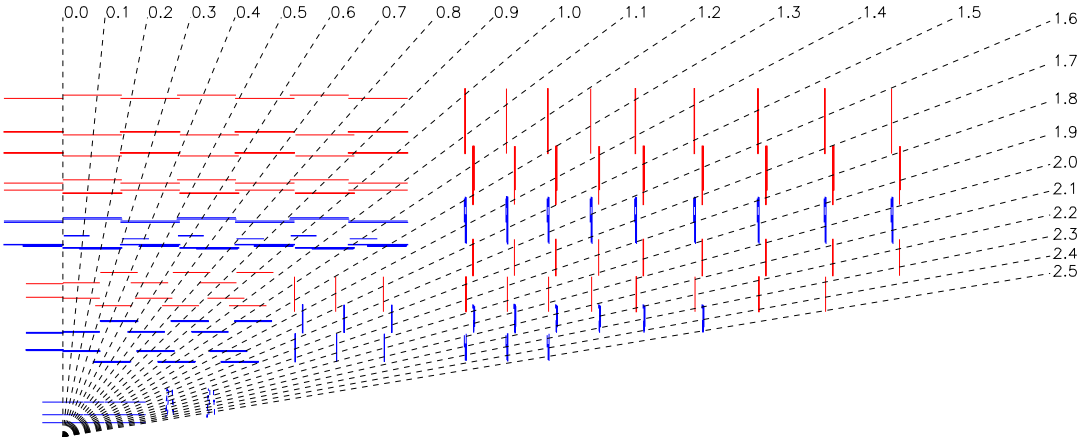

Figure 2.6: *Longitudinal view of one quarter of the silicon tracker, including the pixel detector. Different colors are used for single-sided (red), double-sided and pixel (blue) modules.*

The entire silicon strip detector consists of almost 15400 modules, which will be mounted on carbon-fiber structures and housed inside a temperature controlled outer support tube. To enhance the radiation hardness of the system, the full detector will operate at a temperature of about $-20°C$.

2.3 The Calorimeters

2.3.1 The Electromagnetic Calorimeter

The goal of the electromagnetic calorimeter (ECAL) [17] is the accurate measurement of the energy and position of electrons and photons. The physics process that imposes the strictest requirements on its performance is the low mass Higgs decay into two photons: the goal is a 1% $\gamma\gamma$ invariant mass resolution. The natural choice to achieve this task is a homogeneous calorimeter; ECAL is composed of about 80000 finely segmented lead tungstate ($PbWO_4$) crystals. Lead tungstate is a fast, radiation-hard scintillator characterized by a small Molière radius (21.9 mm) and a short radiation length (8.9 mm), that allows good shower containment in the limited space available for the detector. Moreover, these crystals are characterized by a very short scintillation decay time that allows to collect about 80% of the light within 25 ns.

The length of the crystals is 230 mm in the barrel and 220 mm in the endcaps, corresponding to 25.8 and 24.7 radiation lengths respectively. Crystals are trapezoidal, with a square front face of 22×22 mm^2 ($\Delta\eta \times \Delta\phi = 0.0175 \times 0.0175$) in the barrel and 28.6×28.6 mm^2 in the endcaps, matching the Molière

radius.

The calorimeter system should also be able to distinguish between showers initiated by neutral pions and photons, or charged pions and electrons. For this reason in the endcaps a pre-shower device with higher granularity will be used; it consists of two lead radiators and two planes of silicon strip detectors, with a total length of 3 X_0. This device will also help in the estimation of the photon direction thus improving the measurement of the two-photon invariant mass.

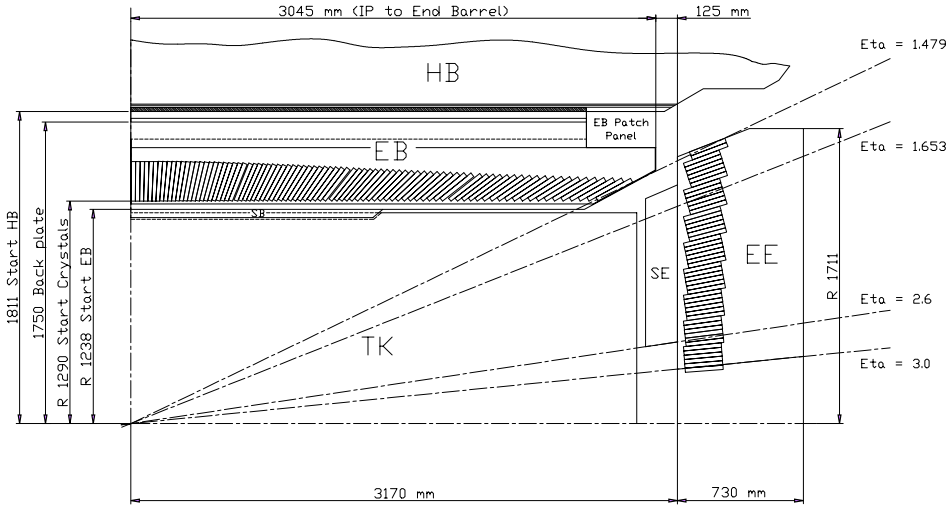

Figure 2.7: *Longitudinal view of one quarter of the ECAL.*

The geometric coverage of the calorimeter extends up to $|\eta| = 3.0$, as shown in Fig. 2.7. The crystals are arranged in a η-ϕ grid in the barrel and a x-y grid in the endcaps and they almost pointing to the interaction point: the axes are tilted at 3° in the barrel and at $2 - 5°$ in the endcaps with respect to the line from the nominal vertex position.

The relatively low light yield of the crystals ($\sim$ 30 γ/MeV) requires photodetectors with intrinsic high gain that can operate in a magnetic field. Silicon avalanche photodiodes (APDs) and vacuum phototriodes (VPTs) are used to collect the scintillation light in the barrel and in the endcaps respectively.

The energy (E) resolution of a calorimeter can be parametrized as

$$\left(\frac{\sigma}{E}\right)^2 = \left(\frac{a}{\sqrt{E}}\right)^2 + \left(\frac{\sigma_n}{E}\right)^2 + c^2 \tag{2.1}$$

where a is called stochastic term and it includes the effects of fluctuations in the number of photo-electrons as well as in the shower containment, σ_n is the noise from the electronics and pile-up and c is a constant term related to the

calibration of the calorimeter. The values of the three constants measured on test beams are reported in Table 2.1. The different contributions as a function of the energy are shown in Fig. 2.8.

Table 2.1: *Contributions to the energy resolution of ECAL (The energy E is expressed in GeV).*

Contribution	Barrel ($\eta = 0$)	Endcap ($\eta = 2$)
Stochastic term	$2.7\%/\sqrt{E}$	$5.7\%/\sqrt{E}$
Constant term	0.55%	0.55%
Noise (high luminosity)	0.155 GeV	0.205 GeV
Noise (low luminosity)	0.210 GeV	0.245 GeV

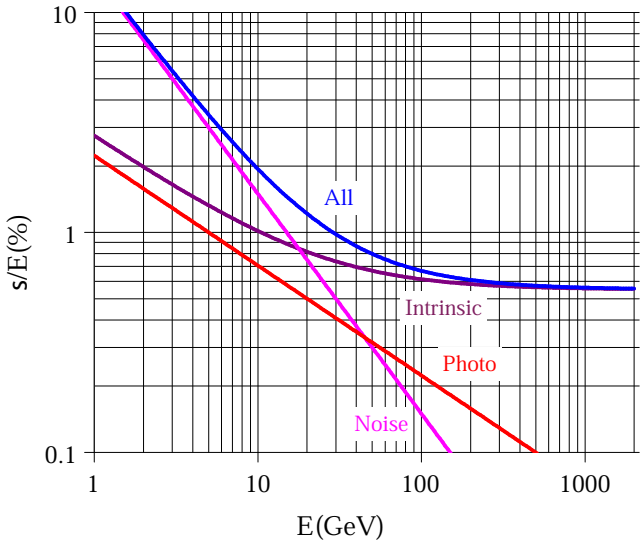

Figure 2.8: *Different contributions to the energy resolution of the ECAL [17]. The curve labeled "intrinsic" includes the shower containment and a constant term of 0.55%.*

2.3.2 The Hadron Calorimeter

The hadron calorimeter (HCAL) [18] surrounds the ECAL and works together with it to measure direction and energy of jets and transverse missing energy. One of the main design requirement for the HCAL is therefore a high hermeticity. Moreover, the identification of forward jets is very important for the rejection of many backgrounds. For these reasons, the barrel (HB) and the endcap (HE) parts, which cover up to $|\eta| < 3.0$, are complemented by a very forward

calorimeter (HF) which extends the coverage up to $|\eta| = 5.3$. The overall HCAL is assembled with essentially no un-instrumented cracks or dead areas; the gap between the barrel and the endcap HCAL, through which the services of the ECAL and the inner tracker pass, is inclined at 53° and points away from the center of the detector.

The barrel and endcap calorimeters are sampling calorimeters with active plastic scintillators interleaved with brass plates. This absorber material has been chosen as it has a reasonably short interaction length, and is non-magnetic. The read out system is composed of wavelength-shifting fibers. Only the first layer is read out separately while all others are read out together in towers of $\Delta\eta \times \Delta\phi = 0.087 \times 0.087$. In the barrel, full shower containment is not possible within the magnet volume, and an additional "tail catcher" is placed outside the magnet. It is referred as hadron outer (HO) detector and consists of an additional layer of scintillators. The projective depth in terms of nuclear absorption length goes from 5.15 λ_0 at $\eta = 0$ to 9.1 λ_0 at $\eta = 1.3$, and is 10.5 λ_0 in the endcap.

The very forward calorimeter is placed outside the magnet yoke, 11 m from the interaction point. The active elements are quartz fibers parallel to the beam, inserted in steel absorber plates.

The energy resolution is $\sigma/E \sim 65\%\sqrt{E}\oplus 5\%$ in the barrel; $\sigma/E \sim 85\%\sqrt{E}\oplus 5\%$ in the endcaps and $\sigma/E \sim 100\%\sqrt{E} \oplus 5\%$ (E in GeV) in the very forward calorimeter.

2.4 The Muon System

High-p_T muons will provide a clear signature for many physics processes. For this reason, the muon spectrometer must provide a robust trigger and an accurate measurement of the muon momentum and charge, also without the contribution of the tracker. The detection of narrow states decaying into muons over a wide range of masses, will pose stringent requirements on the momentum resolution: the goal is to reach $\Delta p_T/p_T \sim 10\%$ at $p_T = 1$ TeV/c.

The muon spectrometer [19] is composed of three independent subsystems, all of them are used both for tracking and for trigger in order to guarantee robustness and redundancy. The layout of the system is presented in Fig. 2.9. In the barrel ($|\eta| < 1.2$) where the track occupancy and the residual magnetic field are low, drift tube detectors (DT) are installed. In the endcaps the particle rate is higher and a large residual magnetic field is present, for this reason cathode strip chambers (CSC) are employed. The coverage of the DT and the CSC system goes up to $|\eta| < 2.4$. In the region $|\eta| < 2.1$ a third system, composed by resistive plate chambers (RPC), is present. These detectors are characterized by a limited spatial resolution but they have an excellent time resolution and

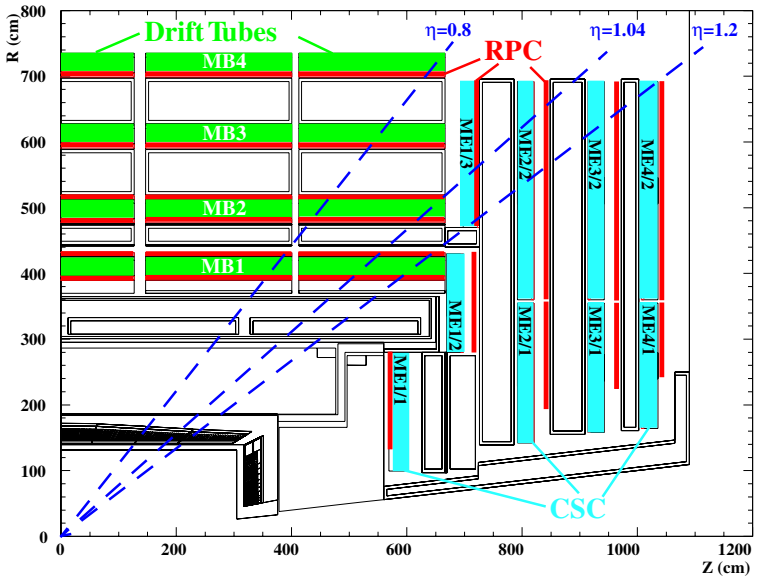

Figure 2.9: *Longitudinal view of one quarter of the muon system.*

fast response providing unambiguous bunch crossing identification.

The muon identification is guaranteed by the amount of material in front of the chambers and in the return yoke of the magnet which shields the spectrometer from charged particles other than muons. The plots in Fig. 2.10 [1] show the material thickness before each muon station as a function of the pseudorapidity; more than 10 interaction length and 110 radiation length are present before the first measurement station of the spectrometer.

The magnetic field inside the iron of the yoke bends the tracks in the transverse plane thus allowing the measurement of their p_T. The high field is fundamental for the momentum resolution of the spectrometer but it also sets the environment in which the detector operates. The innermost endcap CSCs, the ME1/1 chambers, are exposed to the full field which, in this region, is almost entirely axial and uniform. In the following CSC stations the field is no longer axial and uniform, however, the small drift space allows these detectors to limit the degradation of the chamber resolution.

In the barrel region most of the flux is contained within the iron plates of the yoke where the axial component of the field reaches $\sim$ 1.8 T. The space where the DT chambers are placed should ideally be field-free. However in the iron gaps and at the end of the coil the residual magnetic field is far from being negligible. The axial and the radial components are shown in Fig. 2.11 for the various barrel DT stations. There are spatially limited regions where the field in the radial direction can reach 0.8 T.

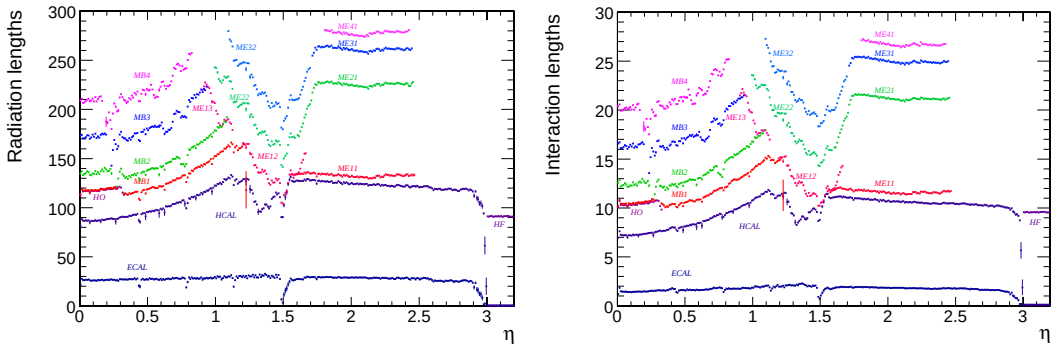

Figure 2.10: *Material thickness in radiation lengths (left) and interaction lengths (right) after the ECAL, HCAL, and at the depth of each muon station as a function of pseudorapidity. The thickness of the forward calorimeter (HF) remains approximately constant over the range $3 < |\eta| < 5$ (not shown).*

The robustness of the spectrometer is also guaranteed by the different sensitivity of DT, RPC and CSC to the backgrounds. The main sources of background particles in the LHC environment will be represented by secondary muons produced in pion and kaon decays, from punch-through hadrons and from low energy electrons originating after slow neutron capture by nuclei with subsequent photon emission. This neutron induced background will be the responsible of the major contribution to the occupancy level in the muon detectors. The total background rate at high pseudorapidity reaches up to 1 kHz/cm^2 in the innermost part of the ME1/1 station. In the barrel the fluences are much lower being everywhere less than 10 Hz/cm^2. As described in the following sections CSC and DT chambers, in contrast with RPC detectors are characterized by a layer layout which helps in reducing the effect of background hits: the request of correlation between consecutive layers is particularly effective against background hits affecting only a single layer.

2.4.1 The Drift Tube Chambers

Muon detectors in the barrel do not operate in particularly demanding conditions, since the occupancy in this region is low and the magnetic field is well contained in the iron plates of the return yoke. For this reason, drift tubes were chosen.

The basic element of a DT detector is the the drift cell, whose section is shown in Fig. 2.12. A layer of cell is obtained by two parallel aluminium planes separated by "I" shaped aluminium beams which define the boundary of the cells. The cell has a size of 42×13 mm^2 with a 50 μm diameter stainless steel anode wire at the center. The distance of the track from the wire is given by

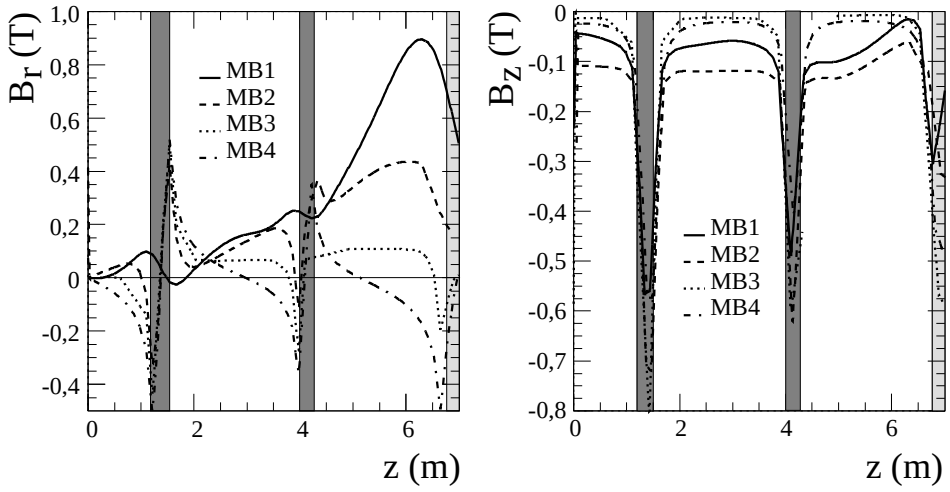

Figure 2.11: *Magnetic field components radial (B_r) and axial (B_z) with respect to the beam line in the different barrel stations as a function of the distance from the CMS center in the axial direction (along the z-axis). The shaded areas are the gaps between the detector rings.*

the drift time of electrons produced in the ionization; to improve the distance-time linearity, additional field shaping is obtained with two positively-biased insulated strips, glued on the the planes in correspondence of the wire. Typical operational voltages are +3600 V, +1800 V and -1200 V for the wires, the strips and the cathodes, respectively. The gas is a 85%/15% mixture of Ar/CO_2, which provides good quenching properties and a saturated drift velocity, of about 5.5 cm/μs. The maximum drift time is therefore $\sim$ 380 ns, *i.e.* 15 bunch crossings. A single cell has an efficiency of about 99.8% and a spatial resolution of about 180 μm.

Four staggered layers of parallel cells form a *superlayer*, which provides the measurement of a two-dimensional segment solving the left-right ambiguity of a single layer by means of pattern recognition. Also, the information of a superlayer can be used at the trigger level to measure the bunch crossing originating a segment with no need of external input, using a generalization of the mean-timer technique [20].

A chamber is composed by two superlayers measuring the r-ϕ coordinates, with the wires parallel to the beam line, and an orthogonal superlayer measuring the r-z coordinates. The latter is not present in the outermost station (MB4). The wire lenght varies, depending on the superlayer type and on the station, from about 2 m to 3 m. The superlayers are glued on the two sides of an honeycomb spacer which ensures the required stiffness to the structure. A cross-sectional view of a chamber is shown in Fig. 2.13.

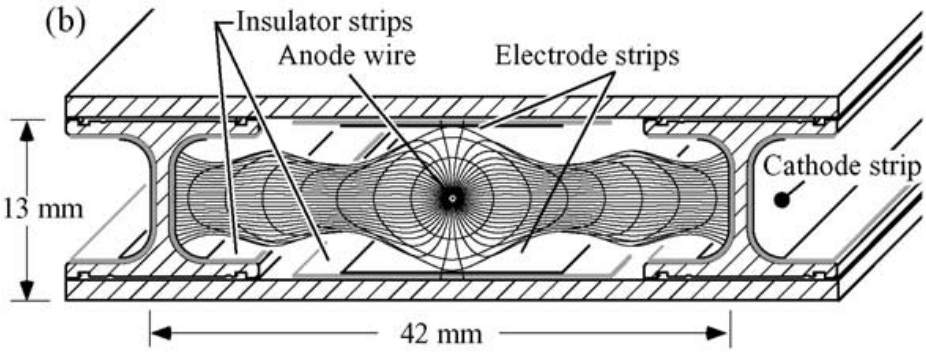

Figure 2.12: *Section of a drift tube cell.*

The Level-1 local trigger and read-out electronics is placed on the chamber, in a Mini-Crate (MC) mounted on the side opposite to the HV supply of each chamber, inside one of the "C" profiles surrounding the honeycomb structure shown in Fig. 2.13. The boards dedicated to the Level-1 chamber trigger hosted by the MC are the Bunch and Track Identifier (BTI), the Track Correlator (TRACO), and the Trigger Server (TS) [21] (cf. Section 2.5.1.1). Concerning the read-out devices the MC is intrumented with Readout Boards (ROB), each equipped with four 32-channel High Performance Time to Digital Converters (HPTDC) [22]. There are five to seven of such ROBs in each MC depending on the chamber size; the number of read-out channels varies from 608 to 800 per chamber.

2.4.1.1 Labelling and Reference Frame

The chamber segmentation follows that of the iron of the yoke, consisting in five wheels along the z-axis, each one divided into 12 azimuthal sectors. The wheels are numbered from -2 to +2, sorted according to global CMS z-axis, with wheel 0 situated in the central region around $\eta = 0$. The numbering of sectors is assigned in anti-clockwise sense when looking to the detector from the positive z-axis, starting from sector number 1 which is the vertical one towards positive x in the CMS reference frame. Chambers are arranged in four *stations* at different radii, named MB1, MB2, MB3 and MB4 as shown in Fig. 2.9. The first and the fourth stations are mounted on the inner and outer face of the yoke; the remaining two are located in slots within the iron. Each station consists of 12 chambers, one per sector, except for MB4 where 14 chambers are present.

The chamber reference frame used in the framework of the official CMS simulation and reconstruction code is centered in the chamber center with the x-axis orthogonal to the wires in r-ϕ superlayers while the y-axis has the direction

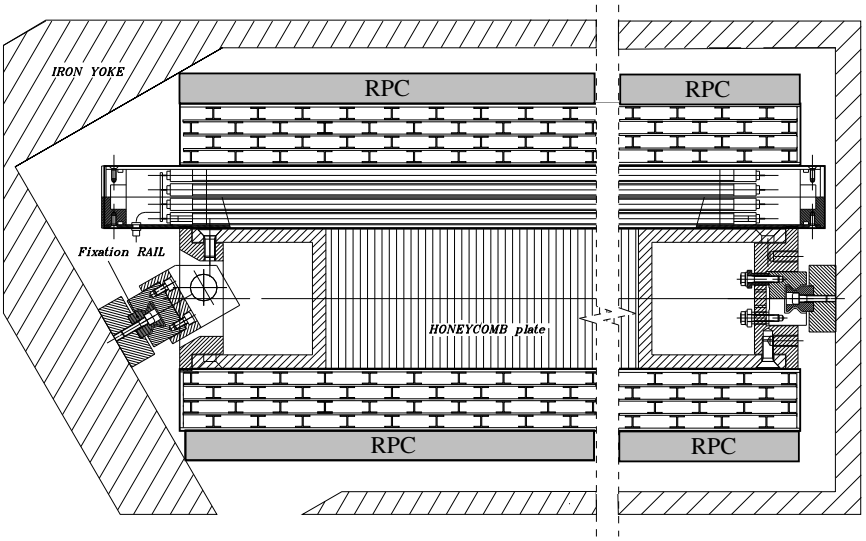

Figure 2.13: *Schematic view of a MB1/MB2 DT chamber. The two resistive plate chambers of the muon station are also shown.*

of the coordinate measured by r-z superlayer and points towards the r-ϕ FE electronics.

The front-end position of r-ϕ layers is always on the outermost side of the chamber with respect to the interaction point since this allows to compensate the effect of the time of flight and the propagation time along the wire on the TDC measurement. For this reason the reference frame of chambers in positive and negative wheels are opposetly disposed with respect to the CMS coordinate system: chambers in wheels +1 and +2 have the y-axis pointing towards the positive CMS z-axis (see Fig. 2.14), while chambers in wheels -1 and -2 have the reference frame rotated by 180°. In wheel 0 the FE position varies from sector to sector. The local coordinate system of the r-ϕ superlayers and layers have the same orientation of that of the chamber but their centers coincide with the quadruplet and layer center respectively. Regarding the r-z view, the local frames of superlayers and layers are oriented with the x-axis along the measured coordinate and the y-axis along the wires, pointing to the FE.

2.4.2 The Cathode Strip Chambers

Cathode strip chambers are multi-wire proportional chambers with good spatial and time resolution. Thanks to their capacity of operating with high occupancy levels and large inhomogeneous magnetic field they are adopted in the endcap regions.

CSC chambers are composed of six layers, each consisting of an array of

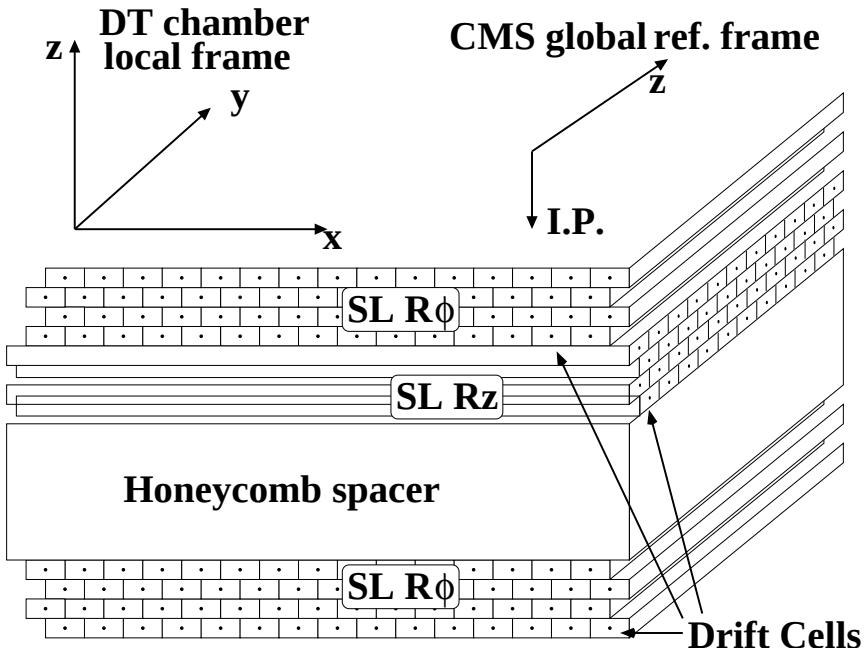

Figure 2.14: *Schematic view of a DT chamber indicating the coordinate system in a positive wheel, as defined in the CMS code.*

anode wires betwen two cathode planes (see Fig. 2.15) with a gap of 9.5 mm. One of the cathode planes is segmented into strips orthogonal to the wires, disposed in the radial direction to measure the ϕ coordinate. The width of the strips ranges from 3 to 16 mm for different chambers. The avalanche produced by the crossing particle in the 30%/50%/20% mixture of $Ar/CO_2/CF_4$ induces a charge in several adjacent strips. A precise spatial measurement is obtained interpolating the strip signals achieving a resolution of about ~ 50 μm. The r coordinate is measured by the wires which, to reduce the number channels, are read out in groups of 5 to 16 with a resolution of the order of ~ 0.5 cm.

CSC chambers are arranged in four disks (*stations*) placed between the iron disks of the yoke and labeled ME1, ME2, ME3 and ME4 (cf. Fig. 2.9). The innermost station consists of three concentric rings, the first (ME1/1) being at smaller $|z|$ than the other two. The other stations are composed by two disks only. The rings are formed by 18 or 36 trapezoidal chambers, which, with the exception of the outermost ring of ME1, are staggered with a small overlap in ϕ.

The most internal disk of the first station (ME1/1) is exposed to particularly difficult conditions characterized by high magnetic field and intense particle rate. These chambers adopt a slightly different design with wires tilted by 25° to compensate for the Lorentz drift in the magnetic field. The gap is reduced

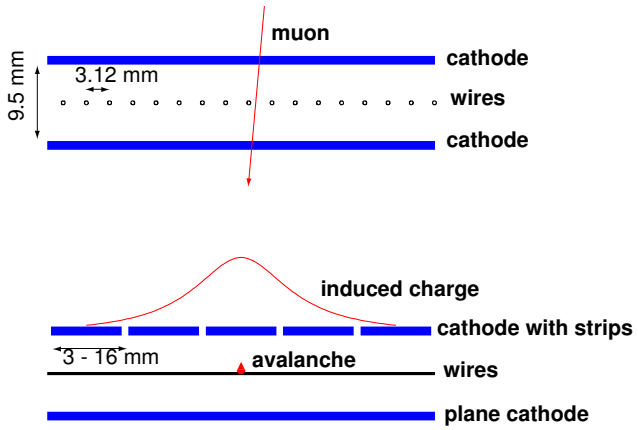

Figure 2.15: *Orthogonal sections of a CSC layer.*

to 6 mm and the number of strips is doubled above $\eta = 2.0$.

Although the single layer precision on the time measurement has a spread exceeding 25 ns, a sophisticate algorithm, using the second or third earlier hit in a pattern of six, can give more than 99% efficiency in finding the correct bunch crossing.

2.4.3 The Resistive Plate Chambers

The resistive plate chambers are installed both in the barrel and in the endcaps and are thus complementary to the CSC and the DT systems.

The RPCs used by CMS are double gap chambers composed of four bakelite planes externally coated by graphite electrodes, as shown in Fig. 2.16. Insulated

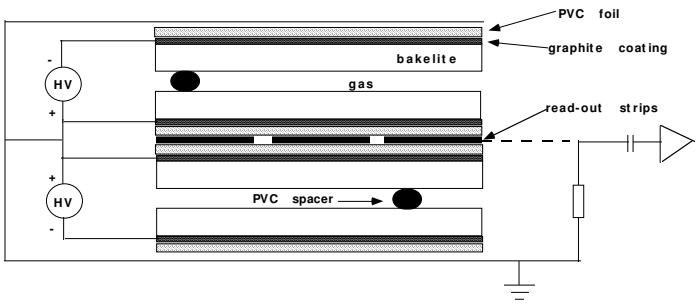

Figure 2.16: *Schema of a double-gap resistive plate chamber.*

aluminium strips are placed in the middle, to collect the signal induced in the 90% $C_2H_2F_4$ (freon) and 10% i-C_4 H_{10} (isobutane) gas mixture by crossing particles.

The two innermost electrodes are kept to +9.5 kV and the RPCs will operate in "avalanche" mode, rather than in the more common "streamer" mode, obtained with a lower electric field and allowing to sustain higher rates. However, the gas multiplication is reduced, and improved electronic amplification is required. The two-gap design is adopted to increase the charge induced on the strips.

Other concerns come from the noise rate due to discharges caused by irregularities in the bakelite surfaces. These effects can be suppressed by treating the surfaces with lineseed oil, which has been adopted for the barrel detectors. However, the high radiation dose can cause aging effects on the oil, which is therefore not used in the endcaps.

In the barrel, RPC chambers follow the segmentation of DT chambers. A total of six layers of RPCs are present; the first four are attached to each side of the MB1 and MB2 DT chambers, as shown in Fig. 2.13. The other two are attached to MB3 and MB4. In the endcaps, chambers are trapezoidal; four layers are present.

In the barrel, the strips are parallel to the beam line, with a length of 80 or 120 cm and their pitch varies from 2.1 cm in the inner MB1 plane to 4.1 cm in the MB4 planes. In the endcaps, strips are radial with a length of 25 to 80 cm and have a pitch ranging from 0.7 cm in the most forward chambers to roughly 3 cm. This segmentation is dictated by the radial geometry and by the expected neutral background hit rates. The coordinate orthogonal to the strips is estimated as the centre of a cluster of fired adjacent strips. No measurement is available in the second coordinate, apart from the constraint coming from the strip length. The spatial resolution provided by RPCs is limited by the strip pitch but they are characterized by an excellent time resolution, of the order of few nanoseconds.

2.5 The Trigger

The selection of the interesting events produced in the LHC collisions will be one of the most challenging tasks that the CMS detector will have to face. The bunch crossing frequency at CMS interaction point is 40 MHz while technical difficulties in handling, storing and processing extremly large amounts of data impose a limit of about 100 Hz on the rate of events that can be written to permanent storage, as the average event size will be of about 1 MB.

At the LHC nominal luminosity the total event rate for inhelastic interactions is expected to be of the order of 10^9 Hz while the rate of interesting events

is very small, as shown in Fig. 2.17. The goal of the trigger is to perform the

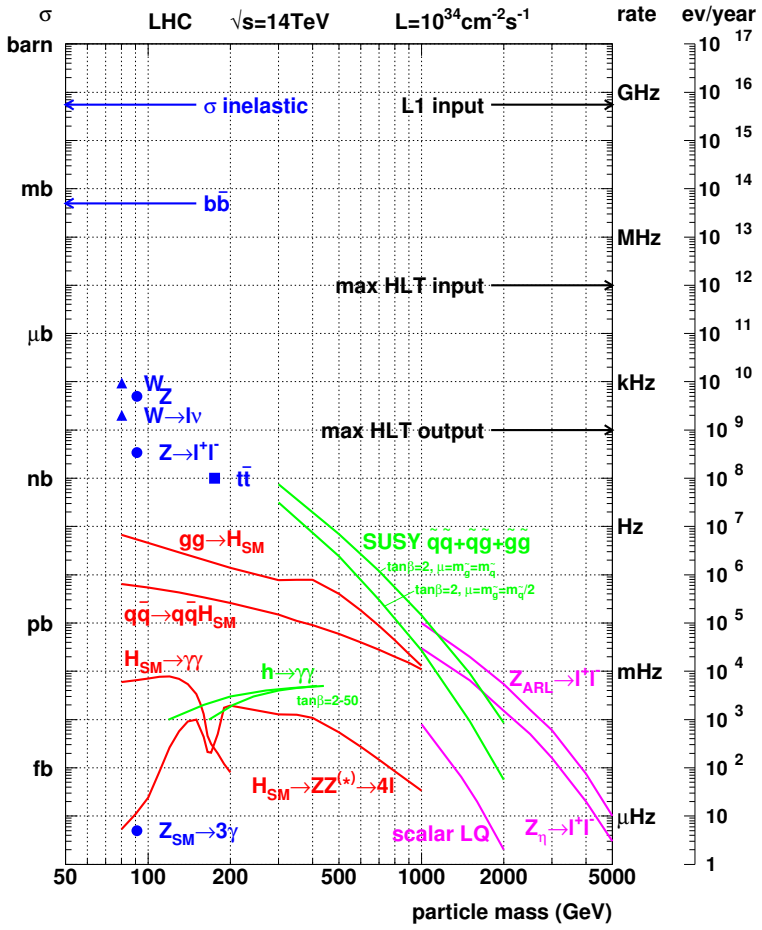

Figure 2.17: *Expected cross sections and event rates at* $10^{34} cm^{-2} s^{-1}$ *as a function of the mass of produced objects.*

required huge on-line selection. This task is difficult not only because of the large rejection factor it requires but also because the output rate is already saturated by processes like $Z \to \ell\ell$ and $W \to \ell\nu$, where high-p_T leptons are produced. The trigger must therefore be able to select events on the basis of their physics content, and online selection algorithms must have a level of sophistication comparable to that of offline reconstruction.

The time available to accept or reject an event is extremly limited, being the bunch crossing time of 25 ns, a time interval too small even to read out all raw data from the detector. For this reason CMS adopts a multi-level trigger design, where each step of the selection uses only part of the available data. In this way higher trigger levels have to process fewer events and have more time available; they can go into finer detail and use more refined algorithms.

The two steps of the CMS selection chain are the Level-1 and the High Level Trigger, which are briefly described in the following. A more detailed discussion can be found elsewhere [23, 24].

The Level-1 trigger. The first step is the Level-1 trigger [23] which has to reduce the input rate down to a level acceptable for the Data Acquisition (DAQ) system. At startup, the DAQ system will be able to handle an event rate of up to 50 kHz, which will be increased to 100 kHz when the full LHC design luminosity is reached. Only one third of this bandwidth will be allocated, the rest being used as safety margin accounting for all uncertainties in the simulation of the basic physics processes, the CMS detector, and the beam conditions [24].

The Level-1 trigger must take an accept or reject decision for each bunch crossing, *i.e.* every 25 ns. This is achieved with a synchronous pipelined structure of processing elements, each taking less than 25 ns to complete, implemented on custom-built programmable electronics in order to minimize the dead time. At each bunch crossing each processing element passes its results to the next element and receives a new event to analyze. The Level-1 has access to data from the calorimeters and the muon detectors with coarse granularity while all data of all detectors is held in pipeline memories in the front-end electronics, whose depth is limited to 128 bunch crossings by the amount of data storable in the tracker and preshower front-end buffers. The Level-1 decision must be therefore taken after a fixed time of 3.2 μs. This also includes the transmission time between the detector and the counting room (a cable path of up to 90 m each way) and, in the case of Drift Tube detectors, the electron drift times (up to 400 ns); tipically the Level-1 trigger calculation must be done in less than 1 μs.

The Level-1 trigger system is organized into three major subsystems: the Calorimeter Trigger, the Muon Trigger, and the Global Trigger. The Muon Trigger is further subdivided into three independent subsystems one for each of the three different muon detector systems, DTs, CSCs and RPCs. The results of these three systems are combined by the Global Muon Trigger. A schematic view of the components of the Level-1 trigger system and of their relationships is shown in Fig. 2.18.

The Calorimeter and Muon Triggers do not perform any selection themselves. They identify "trigger objects" of different types: isolated and non-isolated electron/photons; forward, central and τ-jets; muons. The four best candidates of each type are selected and sent to the Global Trigger, together with the measurement of their position, transverse energy or momentum and a quality flag. The Global Trigger also receives the total and missing transverse energy measurement from the Calorimeter Trigger.

The Global Trigger allows to define complex trigger algorithms based on

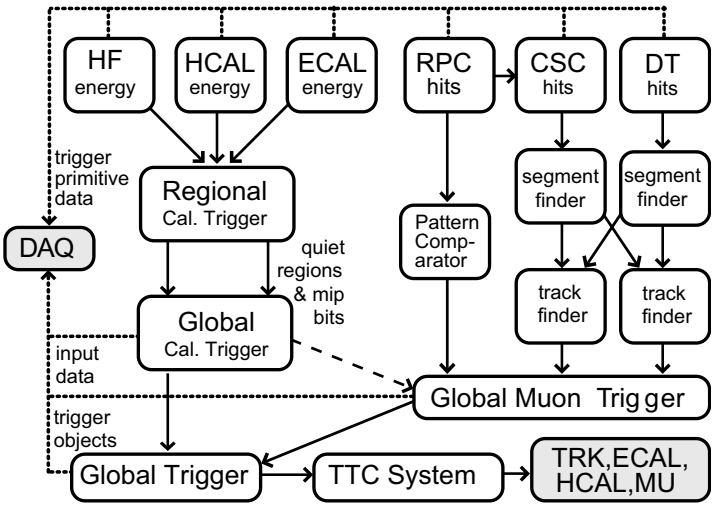

Figure 2.18: *Structure of the Level-1 trigger system.*

the presence of several different objects and on topological conditions and correlations. However, whenever possible, "inclusive" criteria should be used, to avoid biasing the sample of selected events. The simplest triggers are in general those based on the presence of one object with an E_T or p_T above a predefined threshold (single-object triggers) and those based on the presence of two objects of the same type (di-object triggers) with either symmetric or asymmetric thresholds. Other requirements are those for multiple objects of the same or different types ("mixed" and multiple-object triggers). In the case of special channels that are not efficiently selected by these simple criteria, very specific exclusive algorithms can be used.

The choice of the Level-1 trigger thresholds is determined by the maximum event rate (bandwidth) that can be accepted by the DAQ system. The available bandwidth is subdivided among the Level-1 objects [24] (muons, electrons and photons, tau jets, jets and combined channels) and for each of them between the single and multiple-object streams.

The result is a set of thresholds called trigger table. The present Level-1 trigger tables at low and high luminosity are shown in Table 2.2 and Table 2.3, respectively.

The High Level Trigger. Following a Level-1 accept, data are collected by readout units and the event is sent to the next step of the selection: the High Level Trigger (HLT) [24]. The goal of the HLT is to reduce the event rate from the maximum Level-1 output to 100 Hz which is the maximum rate for mass storage.

Table 2.2: *Level-1 trigger table at low luminosity ($2 \times 10^{33} cm^{-2} s^{-1}$) [24].*

Trigger	Threshold (GeV or GeV/c)	Rate (kHz)	Cumulative Rate (kHz)
Inclusive isolated electron/photon	29	3.3	3.3
Di-electrons/di-photons	17	1.3	4.3
Inclusive muon	14	2.7	7.0
Di-muons	3	0.9	7.9
Single tau-jet trigger	86	2.2	10.1
Two tau-jets	59	1.0	10.9
1-jet, 3-jets, 4-jets	177, 86, 70	3.0	12.5
Jet * ET miss	88 * 46	2.3	14.3
Electron * Jet	21 * 45	0.8	15.1
Minimum-bias (calibration)		0.9	16.0
Total			16.0

Table 2.3: *Level-1 trigger table at high luminosity ($10^{34} cm^{-2} s^{-1}$) [24].*

Trigger	Threshold (GeV or GeV/c)	Rate (kHz)	Cumulative Rate (kHz)
Inclusive isolated electron/photon	34	6.5	6.5
Di-electrons/di-photons	19	3.3	9.4
Inclusive muon	20	6.2	15.6
Di-muons	5	1.7	17.3
Single tau-jet trigger	101	5.3	22.6
Two tau-jets	67	3.6	25.0
1-jet, 3-jets, 4-jets	250, 110, 95	3.0	26.7
Jet * ET miss	113 * 70	4.5	30.4
Electron * Jet	25 * 52	1.3	31.7
Muon * Jet	15 * 40	0.8	32.5
Minimum-bias (calibration)		1.0	33.5
Total			33.5

The HLT will be completely implemented on software running on a farm of commercial processors thus allowing full flexibility and optimization of the algorithms, which are only limited by the maximum available CPU time and data bandwidth.

The use of standard software techniques and languages will also make it possible to benefit from the continuous improvements in the reconstruction software. In particular the algorithms used in the HLT, which will have access to data with full resolution and granularity from any part of the detector, will be identical to those used in the off-line reconstruction.

The HLT does not have an internal architecture of separate trigger levels. However, in order to discard uninteresting events as soon as possible, the selection is organized in a sequence of logical steps: the Level-2 and Level-3. The Level-2 uses the full information from calorimeters and muon detectors and it is expected to reduce the event rate by roughly one order of magnitude. The data from the silicon tracker represent almost 80% of the event size and require complex and time consuming algorithms for the reconstruction. For this reason this information is used only during the Level-3 selection.

2.5.1 The Muon Trigger Selection

The Muon Trigger has the goal to identify muons, reconstruct their position and transverse momentum and provide bunch crossing assignment with high purity and efficiency.

The generator-level inclusive integral rate of single muons is shown in Fig. 2.19, as a function of the p_T threshold. The total rate curve is very steep for low p_T thresholds; a precise measurement of the muon transverse momentum is therefore essential for the muon trigger in order to avoid large feed-through of low-p_T muons at high thresholds.

For p_T thresholds up to 5 GeV/c, the muon rate is dominated by non-prompt muons produced by decays of charged kaons and pions. For thresholds between 5 and 25 GeV/c the dominant contribution is the decay of the bottom and charm quarks, while above 25 GeV/c the contribution of W and Z boson decays become important.

The threshold for the single muon trigger at the LHC design luminosity should be of the order of 20-30 GeV/c to preserve good efficiency for signal events, like Higgs boson decays.

2.5.1.1 The Level-1 Muon Trigger

In order to ensure redudancy and robustness with high efficieny and good background rejection all the three detector subsystems described in Section 2.4 take

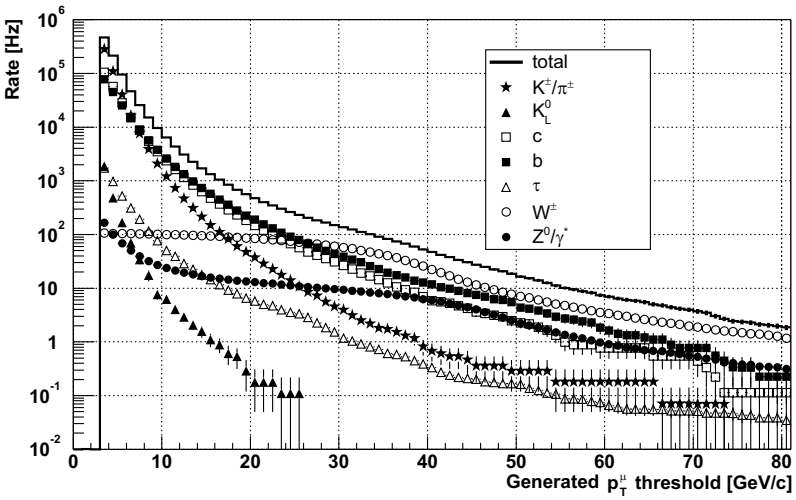

Figure 2.19: *Generator-level inclusive integral rate of single muons within the muon trigger geometrical acceptance ($|\eta| < 2.1$) at the LHC design luminosity ($10^{34} cm^{-2} s^{-1}$), as a function of the muon p_T threshold [25]. The breakdown of the rate from each source of muons is shown.*

part to the Level-1 muon trigger [23]. This allows to benefit from the complementary characteristics of the different types of detectors: the good spatial resolution of drift tubes and cathode strip chambers and the excellent time resolution of resistive plate chambers. The wire chamber systems and the RPC are complementary also in the sensitivity to backgrounds and in their inefficiencies; the layer structure of DTs and CSCs is an effective defence against low range background particles or intrinsic noise which, on the contrary, can cause ghost triggers in the RPCs.

The structure of the muon trigger is shown in Fig. 2.20. The DT and CSC Level-1 triggers are composed by two steps: a Local Trigger and a Regional Trigger. The Local Trigger consists in the reconstruction of track segments in the chambers. The following step is performed by the DT and CSC Regional Track Finders which match the segments in the different stations reconstructing a muon track and assigning a p_T measurement. In the overlap region DT and CSC segments are used by both Track Finders to allow the reconstruction of full tracks in each of the two subsystems.

In the RPCs, the hits are collected by a Pattern Comparator Trigger (PACT), which looks for predefined patterns. The PACT provides an estimate of the p_T of the muon and its position.

Each subsystem reconstructs up to four muon candidates which are then delivered to the Global Muon Trigger toghether with a word to indicate their

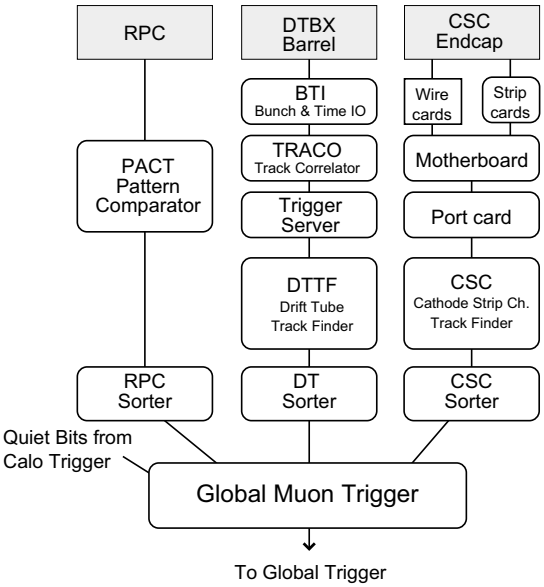

Figure 2.20: *Schematic structure of the muon trigger system.*

quality. The GMT matches them and looks for the MIP and Quiet bits in the corresponding calorimeter regions. Finally, the four muons with highest p_T are sent to the Global Trigger which takes the Level-1 decision.

The acceptance of the muon trigger will be limited with respect ot that of the whole spectrometer since the trigger electronics will not be installed in the most forward CSC station ME1/1a, thus covering only up to $|\eta| < 2.1$.

The following paragraphs shortly desribe the muon reconstruction in the different subsystems.

The DT Trigger. The Level-1 Local Trigger is the first step of the DT selection; it reconstructs segments at the chamber level. It is implemented using Application Specific Integrated Circuits (ASIC) installed on-chamber within the so called Mini-Crate togheter with the chamber read-out electronics.

The DT trigger front-end is called Bunch and Track Identifier (BTI). It is directly connected to the read-out electronics, and performs a straight segment fit within a superlayer using at least three hits out of the four layers of drift cells. Aligned hits are recognized exploiting a generalisation of the mean-timer technique [20], which also returns the bunch crossing originating the segment. In r-z superlayers, only segments pointing to the interaction point are selected. The segments reconstructed in the two r-ϕ superlayers of each chamber are matched by the Track Correlator (TRACO), that improves the angular resolution thanks to the bigger lever arm. The Trigger Server (TS) selects, among all

segment pairs in a chamber, the two corresponding to the highest p_T, (*i.e.* with the smallest angular distance with respect to the radial direction to the vertex) and forwards them to the Drift Tube Track Finder (DTTF).

The DTTF performs the Regional Level-1 reconstruction: it matches the segments reconstructed in the four stations into muon track candidates, assigning the track parameters p_T, η, ϕ and a quality word. This device, located in the underground control room, is implemented using Field Programmable Gate Arrays (FPGA). It is based on precomputed, memory-resident Look-Up Tables (LUT), which are used to extrapolate the segments between stations and to group matching segments. The track parameters are estimated with other LUTs on the basis of the the ϕ direction of the segments in the two innermost stations.

Finally, the candidates are sorted, and the four highest p_T muon candidates are delivered to the Global Muon Trigger.

The CSC Trigger. As for the barrel, the first step of the CSC Level-1 trigger is the reconstruction of segments at the chamber level. This is performed using independently the strips and the wires of the six layers composing each chamber.

Cathode strips are used to reconstruct the bending coordinate ϕ; they are digitized with half strip resolution using a simple interpolation based on a comparator that analyses the charge in three adjacent strips. The hits in the six layers are then searched for patterns compatible with high-p_T tracks.

The design of the anode electronics is optimized to determine the muon bunch crossing and the η value. Hit patterns compatible with a track coming from the nominal interaction point are searched for with a coincidence technique. A coincidence of two hits in different layers is needed to assign the bunch crossing, while the reconstruction of a segment requires four hits out of the six CSC planes. In order to reduce the number of channels, wires are read out in groups of 5 to 16.

Up to two cathode and two anode segments can be found in each chamber during any bunch crossing. The two projections are then combined into three-dimensional segments requiring a time coincidence. These are sent to the CSC track finder which matches the segment of the various stations to form a muon candidate and assigns p_T, η, ϕ and a quality word, using LUTs as in the case of the DTs.

The CSC system covers the region up to $|\eta| = 2.4$. However, the trigger electronics will not be installed in the most forward station ME1/1a: muon tracks in the region $2.1 < |\eta| < 2.4$ can only be reconstructed from segments in the other three stations, with poor p_T resolution due to the reduced magnetic field in the region. For this reason the acceptance of the single-muon trigger is limited to $|\eta| < 2.1$.

The RPC Trigger. Since the measurements in the single resistive plate chambers are simple points the RPC trigger [23] can not perform any local selection. The hits of the different stations are directly collected by the Pattern Comparator Trigger (PACT), which looks for hits correlated in space and time. Hits are matched with pre-defined patterns stored in a LUT to provide an estimation of the muon p_T. Muons can be identified using at least three hits in four stations. For the barrel, where six stations are present, the search is done independently for low-p_T muons in the first four layers (in MB1 and MB2) and for high-p_T ones using one layer in each station.

A ghost suppression algorithm is applied to reduce the effect of accidental coincidences due to background hits. The four highest p_T candidates in the barrel and endcaps are then separately sent to the Global Muon Trigger.

The Global Muon Trigger. The task of the Global Muon Trigger (GMT) is to match the best four barrel DT and the best four endcap CSC muon candidates with the 4+4 candidates sent by the RPC trigger. The matching is performed comparing the spatial coordinates of the candidates in the (ϕ, η) space and it can be tuned to achieve the optimal balance between efficiency and background suppression. High efficiency can be obtained selecting candidates even if they are found by only one sub-system. Maximum background rejection can be obtained requiring all candidates to be reconstructed by both subsystems. It is also possible to exploit more refined criteria; in the current implementation a candidate is accepted if it is reconstructed by two complementary systems otherwise it is selected on the basis of its quality word. Low-quality candidates from problematic η regions are discarded [26]. If two candidates are matched, the parameters of the track are combined according to a programmable logic to achieve optimum precision.

The GMT also extrapolates the muon tracks back to the calorimeter trigger towers and assigns each candidate the MIP and Quiet bit. These bits can optionally be used to confirm the muon candidate and require that it is isolated.

The data of the four best muon tracks in the entire CMS detector are sent to the Global Trigger which takes the Level-1 decision.

The simplest possible Level-1 muon trigger selection is based on a threshold on the p_T of GMT tracks. The resolution on the reciprocal of the transverse momentum $1/p_T$ is about 17% in the barrel, 20% in the endcaps and 22% in the overlap region. Non-gaussian tails are present and, together with the limited resolution, are responsible for the "feed-through" of low p_T muons that are reconstructed at high momenta, thus passing typical trigger thresholds. This effect is important since the muon rate increases steeply for low p_T values, as shown in Fig. 2.19, so that the contribution of feed-through muons to the Level-1 trigger rate is dominant even for high thresholds. This feed-through effect can

be reduced only by improving the p_T resolution. This is the task of the Muon High Level Trigger.

2.5.1.2 The Muon High Level Trigger

The Muon High Level Trigger [24] is organized in two logical steps: the Level-2 and the Level-3 muon reconstruction. Selection criteria are applied at the end of each step, in order to reduce the event rate to a level acceptable by the following one. The Level-2 consists in the reconstruction of muon tracks in the standalone spectrometer while the Level-3 reconstruction uses both tracker and spectrometer data.

The tracking is based on a Kalman Filter technique [27] which uses as input the results of the local reconstruction in the muon chambers. The same reconstruction algorithms are used also in the off-line reconstruction; the main differences will be in the seeding of the track fit. In particular, both the HLT and the off-line muon reconstruction will use the same local reconstruction algorithms which, for the DTs, are described in Chapter 4. The off-line muon reconstruction in the standalone spectrometer is usually referred as "Standalone Muon Reconstruction" while the analogous of the Level-3 is the "Global Muon Reconstruction".

Both at Level-2 and Level-3 the selection is based on thresholds on the p_T of reconstructed tracks. Additional rate reduction is obtained by the use of isolation algorithms.

The Level-2 Muon Reconstruction. The Level-2 step improves the Level-1 muon trigger response using the full resolution of the muon detectors. It consists in a track reconstruction based on the iterative Kalman Filter method. The selection is based on a cut on the p_T of reconstructed muons.

Track seeds are initially created using Level-1 muon candidates. Starting from these seeds, the hits to be included in the fit are looked for iteratively going from inside out in the muon spectrometer. At each step the state vector (track position, direction and momentum) is extrapolated to the next layer of chambers. The results of local reconstruction — track segments in the DT or CSC systems and three-dimensional hits for the RPCs — are used to update the estimate of the trajectory parameters with the Kalman Filter method.

This procedure is iterated until the outermost measurement station in the muon system is reached. The result is a track state at the outermost muon station updated with all available measurements. This is used as seed to the actual fit which is performed in a similar way using a backward Kalman Filter, and determines the track parameters at the innermost muon station. Finally, the track is extrapolated to the nominal interaction point and fitted with a vertex constraint.

The typical p_T resolution obtained by the Level-2 reconstruction, for muons coming from $W \to \mu\nu$ decays, is about 10% in the barrel, 16% in the endcaps and 15% in the overlap regions. The improvement in the resolution with respect to the Level-1 trigger allows to reduce the muon rate by almost an order of magnitude, as shown in Fig. 2.21.

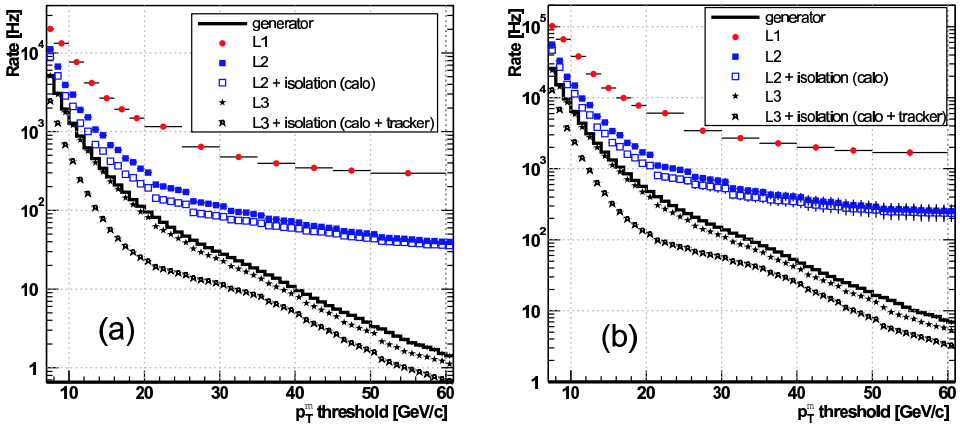

Figure 2.21: *Single-muon trigger rates as a function of the p_T threshold for (a) low luminosity ($2 \times 10^{33} cm^{-2} s^{-1}$) and (b) high luminosity ($10^{34} cm^{-2} s^{-1}$) running conditions. The rates are shown separately for the Level-1, Level-2 and Level-3. The rate generated in the simulation is also shown [24].*

The Level-3 Muon Reconstruction. At Level-3, muon tracks are reconstructed using data from the full tracking system. The resulting improved resolution allows a much sharper p_T cut than at Level-2.

The Level-3 reconstruction starts identifing a region of interest within the silicon tracker around the extrapolated track obtained from the Level-2 reconstruction. Track reconstruction is then performed using the tracker hits within this region starting from the innermost layer. Ambiguities between multiple trajectories that may result from the same seed are solved on the basis of the number of hits and the χ^2 of the track fit. Finally the trajectories are refitted including also the hits of the Level-2 track reconstructed in the muon chambers.

The typical p_T resolution obtained by the Level-3 reconstruction, for muons coming from $W \to \mu\nu$ decays, is about 1.0% in the barrel, 1.7% in the endcaps and 1.4% in the overlap region. This allows to eventually reduce the rate with respect to the Level-2, as shown in Fig. 2.21.

2.6 The Relevance of Muon Reconstruction for the CMS Physics Programme

In the LHC hadronic environment muons represent a clear signature for many physiscs processes. For this reason the muon reconstruction has a key role in the CMS design. In particular, the performance of the spectrometer will be crucial for the following aspects:

- **on-line reconstruction**:
  - *trigger selection*: many interesting processes will be triggered thanks to the presence of muons in the final state since in the LHC hadronic environment the thresholds for selections based on jets will be high. The standalone resolution of the spectrometer plays a key role in the Level-2 selection (cf. Section 2.5.1) substantially improving the resolution with respect to the Level-1, thus reducing the rate of "feed-through" muons and therefore allowing a reliable selection;
- **off-line reconstruction**:
  - *momentum resolution for high energy muons and charge assignment*: the momentum resolution of the spectrometer is shown in Fig. 2.22 toghether with that of the tracker and the global one. The multiple scattering in the material determines the flat behavior of the spectrometer resolution up to p_T values of $100 - 200$ GeV/c, where the chamber spatial resolution begins to be decisive. For low momentum muons it is the tracker which determines the global resolution while at momenta higher than 200 GeV/c the contrinbution of the spectrometer becomes more and more important thanks to its larger lever arm. The large bending power and lever arm provide robust charge assignment also for high energy muons; the fraction of wrongly assigned charge for muons in the barrel region with $p_T = 100$ GeV/c is less than 1% for muons reconstructed with the standalone spectrometer and less than 0.1% when the track is reconstructed using also the tracker information;
  - *muon identification*: thanks to its redundant design the spectrometer allows muon reconstruction with an efficiency of 95%-99% for transverse momenta ranging from 5 GeV/c to 1 TeV/c with an acceptance of $|\eta| < 2.4$. The high magnetic field and the amount of material in front of the chambers will allow reliable muon identification.

Several physics channels will exploit these features of the muon reconstruction. In particular three channels are considered as a benchmark for the muon

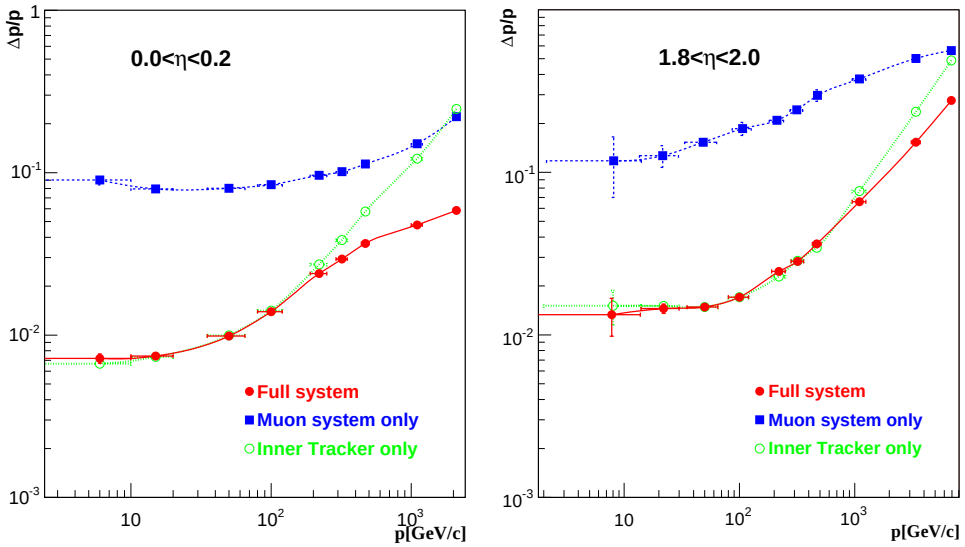

Figure 2.22: *Muon momentum resolution versus p obtained using the muon system only, the inner tracker only, or both ("full system"). The plot on the left is referred to tracks in the central part of the barrel spectrometer ($|\eta| < 0.2$) while the one on the left is referred to tracks in the endcaps ($1.8 < |\eta| < 2.0$) [1].*

reconstruction [1]. These are the $H \to WW^{(*)} \to 2\mu 2\nu$, which is of particular importance if the mass of the Higgs is around 165 GeV/c^2 where the Higgs to WW branching ratio is close to 1, the $H \to ZZ^{(*)} \to 4\mu$ channel, which is one of the cleanest discovery channels for a Standard Model Higgs with a mass up to 600 GeV/c^2 and the $Z' \to \mu\mu$ channel which poses the requirements for the muon reconstruction with p_T in the TeV range.

$H \to WW^{(*)} \to 2\mu 2\nu$ channel. This channel is of particular importance if the mass of the Higgs is around 165 GeV/c^2, where the decay into ZZ is suppresssed. The challenge is to establish a dimuon excess, keeping the uncertainty on the background well under control, since this channel does not allow reconstruction of the Higgs mass.

The muon reconstruction efficiency plays a key role for this channel. The expected efficiency of the double-muon HLT trigger is about 80% while the efficiency for the single or double-muon trigger is 92%.

The cross section for a Higgs mass of 165 GeV/c^2 is about 2 pb. The dominant irreducible background is the continuum production of W pairs decaying into muons and neutrinos. Other significant sources of background are the production of $t\bar{t}$ pairs and the Drell-Yan process.

The signal can be established by looking at the distribution of the azimuthal

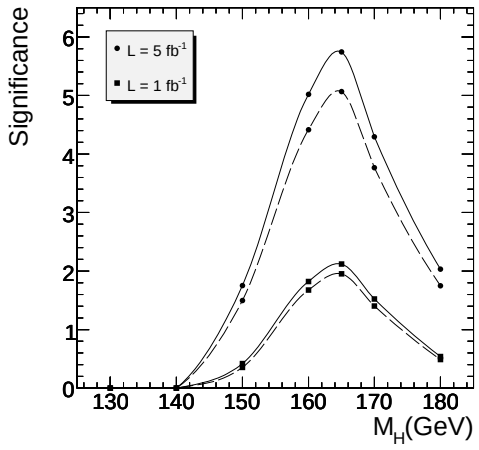

Figure 2.23: *Significance as a function of different masses of the Higgs boson for an integrated luminosity of 1 and 5 fb^{-1}. Solid and dashed lines are referred to different scenarios in the control of the systematics due to WW background [2].*

separation of the leptons ($\Delta\phi$): due to the scalar nature of the Higgs boson, for Higgs masses close to $2M_W$, the W^+W^- spin correlation plays in favour of small opening angles between the two muons while the background distribution is peaked at large values. The significance as a function of different Higgs masses is shown in Fig. 2.23 for integrated luminosities of 1 and 5 fb^{-1}. A signal significance bigger than 3 standard deviations can be achieved with 5 fb^{-1} in the Higgs mass range $155-175$ GeV/c^2. With 1 fb^{-1} luminosity only a 2 sigma significance can be achieved even in the most favourable case $m_H \sim 2m_W$.

$H \to ZZ^{(*)} \to 4\mu$ **channel.** This channel not only represents a "golden-plated" channel for the Higgs discovery over a wide range of masses, but it is also particularly suited for the measurement of the properties of this particle.

The expected cross section for this process ranges from 1 to about 5 fb depending on the Higgs mass in the range 115 GeV/c^2 $< m_H <$ 600 GeV/c^2. The main backgrounds are due to the $t\bar{t}$, $(Z^{(*)}/\gamma^{(*)})b\bar{b}$ and $(Z^{(*)}/\gamma^{(*)})(Z^{(*)}/\gamma^{(*)})$ productions which cross sections are many orders of magnitude higher than the signal one.

The presence of 4 muons in the final state provides a very clean signature and a very high trigger efficiency: the inclusive selection of single or di-muon events assures an efficiency close to 100%.

The isolation requirement on the four leptons is the most powerful tool in the backround rejection. The ZZ background, which presents a topology very

similar to that of the signal, is the dominant and irreducible background.

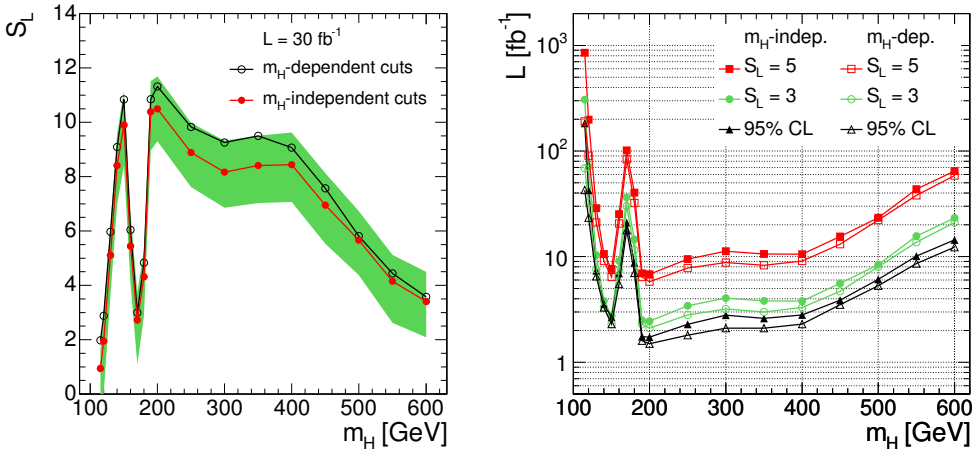

Figure 2.24: *Statistical significance (left) of the $H \to ZZ^{(*)} \to 4\mu$ signal as a function of the Higgs boson mass for an integrated luminosity of 30 fb^{-1}. The shaded band represents the statistical uncertainty. Integrated luminosity (right) required to achieve a statistical significance of 3σ and 5σ, as a function of the Higgs mass. The integrated luminosity required to exclude a Higgs boson signal at 95% C.L. is also shown. [2].*

Figure 2.24 shows the integrated luminosity required to reach a statistical significance of the signal of 3σ and 5σ, as a function of m_H. The expected integrated luminosity required to exclude the signal at 95% confidence level is also shown. By the time CMS reaches $\sim$ 30 fb^{-1}, it would exclude the SM Higgs in the mass range 120 GeV/c^2 $< m_H <$ 600 GeV/c^2, if indeed it does not exists. The discovery at the level of 5σ significance will require from $\sim$ 10 fb^{-1} to $\sim$ 100 fb^{-1} depending on the Higgs mass.

At an integrated luminosity of about 30 fb^{-1} the Higgs mass can be measured with a precision between 0.1% and 5.4% and the intrinsic width could be measured only for the Higgs boson havier than 190 GeV/c^2, with a precision of about 35%. The uncertainty on m_H increases at high masses due to the smaller production cross sections, the larger width of the Higgs boson and to the worse resolution on high p_T muons. The production cross section would be determined with a precision of about 30%.

$Z' \to \mu\mu$ channel. The production of a new gauge boson with a mass in the TeV range is one of the possible early discoveries at the LHC. This process represents a benchmark for the muon reconstruction and, in particular, for the performance of the spectrometer since it requires the reconstruction of very high

energy muons. The resolution, the alignment and the calibration of the muon chambers will play a key role for this signal.

A variety of models has been considered [2] with masses of the Z' boson between 1 and 5 TeV/c^2. The expected cross section varies for each model, it is $\mathcal{O}$(100 fb) for a mass of 1 TeV/c^2 and decreases to $\mathcal{O}(10^{-2}$ fb) for a Z' boson of 5 TeV/c^2. The dominant irreducible background is the Drell Yan production of muons pairs $pp \to \gamma/Z \to \mu^+\mu^-$.

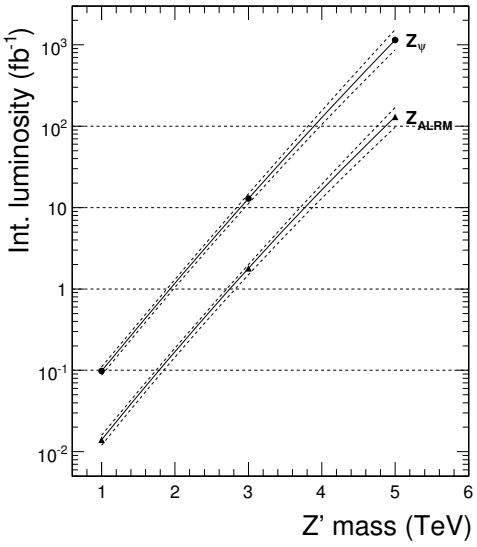

Figure 2.25: *Integrated luminosity needed to reach 5σ significance as a function of the Z' mass for two particular models among those studied in [2]. The dashed lines indicate the boundaries of the band corresponding to the prediction with $\pm 1\sigma$ theoretical uncertainty.*

The efficiency for the single- or di-muon trigger decreases with the Z' mass: it is 98% (95%) at 1 TeV/c^2 and 95% (93%) at 5 TeV/c^2 for low (high) luminosity running conditions. The effect of different foreseen misalignment scenarios on this number has been proved to be negligible if the corresponding uncertainties are considered in the reconstruction.

On the contrary, the misalignment strongly affects the resolution on the Z' mass. Also the non perfect calibration of the drift velocity can have an impact on this measurement. The estimated resolution on the Z' mass ranges from 4 to 8% depending on the alignment uncertainties.

Figure 2.25 shows the integrated luminosity needed to reach a 5σ significance for the signal considering the two models with the smallest and largest cross sections among those considered in the study. A very low integrated lumi-

nosity, less than 0.1 fb^{-1} should be sufficient to discover a Z' boson of 1 TeV/c^2 mass. The discovery of a 3 TeV/c^2 boson will require about 10 fb^{-1} while an integrated luminosity of 100 fb^{-1} is not enough to obtain 5σ significance at 5 TeV/c^2. However, it must be considered that the accuracy in the prediction of the background shape and the knowledge of the invariant mass resolution are important sources of systematics which may sensibly affect the significance of the signal.

Chapter 3

Simulation of the DT Response

Many interesting LHC processes result in a final state containing muons with high transverse momenta. A reliable reconstruction of such events requires a deep understanding of their signature in the apparatus. For this reason an accurate simulation of the response of all CMS subdetectors is needed.

This chapter, after a short introduction to the working principles of the drift detectors in Section 3.1, focuses on the description of the simulation of the Drift Tube chambers. This basically involves two major steps: the first is the simulation of the interaction and of the propagation of the particles in the detector material. The second step is the modeling of the ionization process in the gas volume and of the response of the read-out electronics, including the simulation of the signal collection with all the time delays which contribute the final measurement. The whole procedure is described in Section 3.2.

3.1 DT Working Principles

In the present section a short introduction about the working principles of the DT detectors, described in Section 2.4.1, is given.

A drift chamber relies on the detection of the ionization electrons produced in the Ar/CO_2 gas mixture by a particle crossing the cell. The drift time of such electrons in the electrostatic field is measured to get the information about the spatial coordinates of the ionizing event.

The cell design is shown in Fig. 2.12. A minimum ionizing particle will produce, on average, about 100 ionization electrons in the cell volume. Once they are produced along the trajectory of the particle they drift in the electrostatic field generated by the central anode wire, maintained at a positive potential, and the cathode strips, glued on the I-beam profile, which have negative potential. The drift field is shaped in order to have a linear space-time relationship over the entire volume; this is achieved with the positively-biased strips glued

at the center of the aluminium planes delimiting the cell volume.

The ionization electrons are eventually collected by the anode wire where a strong electric field, increasing as $1/r$, accelerates them enough to produce secondary ionization and hence an avalanche. A gain of about 10^5 is achieved. The CO_2 gas acts as quencher, thanks to its large photo-absorption cross section absorbs the majority of the photons produced during the avalanche development, keeping the avalanche region limited.

The electrons produced in the avalanche are collected by the wire while the positive ions move away from the anode. The induced signal is amplified and discriminated against a configurable threshold by the front-end electronics and it is then sent to the read-out electronics for the TDC measurement.

Electrons produced at a time t_0 by the incoming particle migrate toward the anode with velocity v_d and reach the anode at the a time t_1. The distance of the track with respect to the anode wire is therefore given by:

$$x = \int_{t_0}^{t_1} v_d \cdot dt; \tag{3.1}$$

which, considering a constant drift velocity, becomes:

$$x = (t_1 - t_0)v_d. \tag{3.2}$$

The CMS DTs do not need any external device to determine the t_0 time. In the trigger the on-chamber electronics (cf. Section 2.5.1.1) exploits the redundancy of measurements in three consecutive staggered layers with an extension of the meantimer technique [20] to recognize aligned hits and to determine the bunch crossing when the muon has been produced, without the knowledge of the t_0 offset. In the reconstruction the time pedestal is then extracted directly by the measurement distribution with the calibration procedure that will be described in Section 5.1.

The major factors which can influence the drift velocity are:

- electric field strength and direction and atmospheric pressure. To limit the dependence from these two factors, the working point is chosen to have a value of E/p corresponding to a saturated drift velocity: in the gas mixture used for the CMS DTs the drift velocity saturates for fields of about 1.9 kV/cm. The cell is therefore designed in such a way to avoid regions of field lower than this value, reducing the sensitivity to local field variations;

- gas composition and temperature. The pressure, temperature and purity of the mixture are continuously monitored. In particular the oxygen concentration is always kept below 500 ppm;

- presence of external factors such magnetic stray fields. The presence of a magnetic field modifies the drift properties of an electrons swarm. The Lorentz force applied to each of the moving charges transforms the trajectory into a bending curve. In case of a homogeneous magnetic field along the wire, the main consequence would be an effective lower drift velocity. The movement of the swarm happens along a line different from the field line, as shown in Fig. 3.1 for a simulation of the cell. In CMS the situation is complicated by the fact that the residual magnetic field in the cell volume will not be homogeneous, as shown in Fig. 2.11.

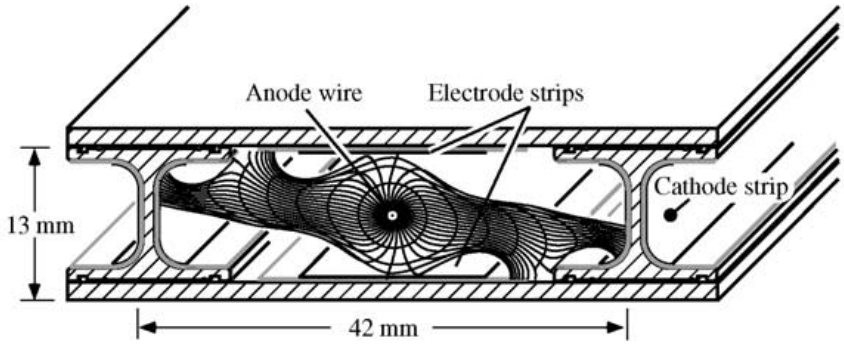

Figure 3.1: *Simulation of the effect produced on the drift lines by a 0.5 T magnetic field parallel to the wire.*

Moreover, for tracks inclined with respect to the normal to the layer plane the time-distance relation is modified by the fact that the electrons having the shortest drift time are not those produced in the mid plane of the drift cell. The effective drift-velocity is therefore higher. No deviation from linearity is usually observed for tracks inclined in a plane parallel to the wire.

The spatial resolution of a drift chamber is limited by the diffusion of the ionization electrons during the drift, the fluctuations of the the primary ionization processes and, finally, by the knowledge of the space-time relationship; the cell resolution of the CMS DT chambers is about 180 μm.

3.2 Simulation of the Drift Cell

The output of the simulation should be as close as possible to the real detector output. This is not meant as a bit stream approximation of the actual raw data, but as a value representing the essential measurement. In the case of the DT detectors this output is basically a time coming from a TDC measurement, containing the drift time information.

The first step of the simulation of the DT response is the propagation of the simulated particles in the detector. The interaction with the material should account for the multiple scattering, the energy loss, the bending of the track due to the magnetic field and the production of secondary particles. During this phase, the information about the passage of a track thorough the sensitive volume of the chamber must be recorded. This step, described in Section 3.2.1, is carried on by the GEANT4 [28] package, which takes into account the geometry and material of the detector and simulates the physics processes that occur as particles cross each volume. The output of this stage of the simulation are GEANT "hits" in "sensitive detector material".

The information contained in those hits is then used for the simulation of the cell response, which consists in the computation of the drift-time of the electrons produced by the ionization. This simulation must reproduce not only the average behavior of the cell as a function of the track parameters and of the magnetic field, but also the dispersion of the drift-times around the mean value, since it has direct impact on the cell resolution. This is achieved with a parametrization of the drift-cell behavior.

Finally, since the DTs are time-measuring devices, all the delays contributing to the TDC measurement must be introduced. In particular the time of flight of the muons from the interaction point to the cell and the propagation time of the signal along the anode wire must be added to the simulated time.

The last two steps, which we refer to as detector "digitization", are described in Section 3.2.2.

3.2.1 Interaction of Crossing Particles with the Detector Material

The interaction of crossing particles with the detector material, in the DTs as in all CMS sub-detectors, is simulated with GEANT4. This software package uses a detailed description of the geometry and the material of the apparatus to propagate particles through the detector. This tracking is performed in steps and, at each step, GEANT employs Monte Carlo techniques to evaluate the probability of all the concurrent processes and computes their effect on the track. At this stage the effect of the multiple scattering on the incoming particle, its energy loss in the material and the bending of tracks due to the magnetic field are simulated. The energy loss is simulated continuously up to a configurable threshold and, above it, by the explicit production of secondary particles such as delta-rays and shower activities which may occur because of bremsstrahlung, Compton scattering and pair production processes. Also the hadronic interactions are included in the simulation.

When a particle crosses a volume declared as sensible, which for the DTs

is the gas volume in each cell, the related information is saved in a simulated "hits", called "SimHits". The information contained in a SimHit is:

- ID of the particle which generated the hit;
- process which generated the particle;
- entry and exit points of the simulated particle as it crosses a detector gas layer;
- position defined as the mid point of the hit track;
- time-of-flight from the interaction point to the hit position;
- energy loss in the volume.

In the following we will show what are the relevant processes involved in the simulation of the DT chamber response. On this purpose we generated a sample of 20000 muons both with positive and negative charge, with a flat momentum distribution between 10 GeV/c and 100 GeV/c. The muons were required to be within the acceptance of the DT subsystem which means they have been generated in the pseudorapidity interval $-1.2 < |\eta| < 1.2$.

The composition of the hits simulated by GEANT in the DTs is summarized in Fig. 3.2 which shows the number of hits per particle type for the various simulated processes. Only 56.0% of the hits is originated by a primary muon crossing the detector. The rest mainly comes from electrons, which contribute for the 39.7%, while the positrons represent only 4.2% of the total. There is also a very small contibution from hadronic hits (about 0.004%) which is not reported in the plot.

The large number of electron hits is mainly produced by the primary ionization due to muons crossing the chamber material (48.4% of the electron hits), but also the secondary ionization, produced by electrons, plays an important role, contributing for 30.6% of the e^- hits. Most of the positrons is originated by conversion processes in the aluminium.

This big population of delta-rays can be ideally divided into two classes: hits produced in the gas volume and hits produced in the aluminium.

The plots in Fig. 3.3 show the momentum (left plot) and the path (right plot) of the hits belonging to the two families. The e^- produced in the gas present a softer momentum spectrum with respect to those produced in the aluminium and, as a consequence, their path in the gas volume is much shorter. We should note that, while 88.7% of these hits cross the whole cell, most of the e^- produced in the gas stops in the sensible volume. Only 6.0% of those hits travels more than 200 μm along the drift lines of the cell, a distance smaller than the cell resolution.

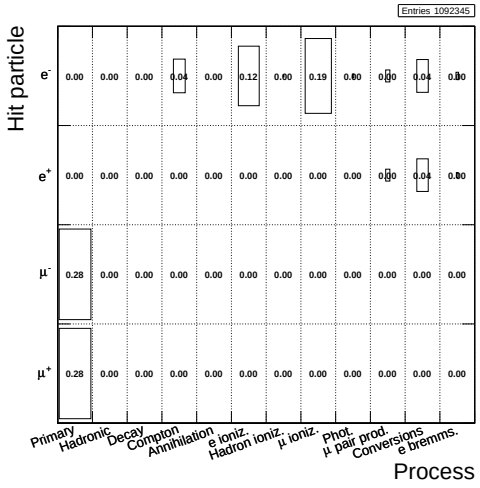

Figure 3.2: *Relative weight of the various particles and processes for the* GEANT *hits in the DT gas volume for a simulated sample of 20000 muons with* p_T *between 10 and 100 GeV/c.*

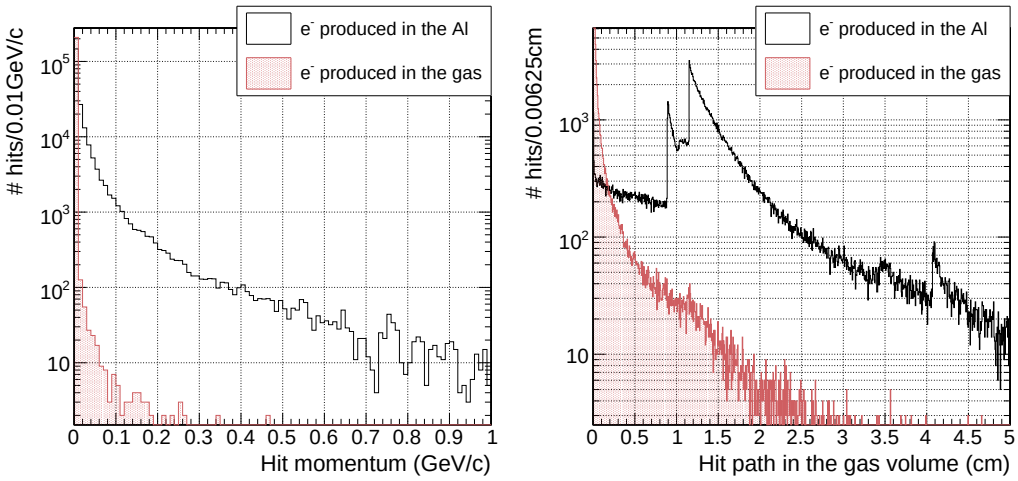

Figure 3.3: *Momentum (left) and path in the gas volume (right) for electron hits produced in the gas and in the aluminium. The three peaks in the path of the* e^- *produced in the aluminium are due to particles crossing the whole drift cell in the two transverse directions. In particular the peak around 0.7 cm is due to particles crossing the layer in correspondence to the I-beam aluminium profiles.*

3.2.2 Digitization in the DTs

The digitization process consists in the computation of a time, simulating a real TDC measurement, starting from the information contained in the GEANT hits.

This involves, first of all, the estimation of a drift time for the electrons produced by the ionization. The second step is the computation of all the delays which contribute to the measurement, namely the time-of-flight of the muon from the interaction point to the cell, the propagation time of the signal along the anode wire and a time pedestal simulating electronic and trigger offsets. They must be simulated since the jitter introduced in the reconstruction by their non-perfect calibration directly contributes to the final resolution.

3.2.2.1 Modeling of the Drift Cell Response

Although the shaping of the drift field in the DT cell was designed to maintain a linear relation between drift-times and distances, residual non linear effects are not negligible especially in the region closest to the anode. For this reason a precise modeling of the cell response can not be obtained using a constant drift velocity for the computation of the drift-time related to a simulated hit. Moreover, the spatial distribution of the electrons produced by ionization depends on the track parameters, such the impact angle, and could have a direct impact on the measured time. The digitization procedure must also take into account the effect of the residual magnetic field in the gas volume which can modify the drift paths of electrons. It is therefore necessary to model the cell response as a function of all these parameters considering their effect on the average behavior but also on the dispersions of the drift times and, as a consequence, on the cell resolution.

To cope with these requirements the digitization process developed was based on an existing parametrization of the DT cell [29]. In the following the parametrization and the way it has been used in the official simulation are described.

Cell Simulation and Parametrization. GARFIELD [30] is a software package for the detailed simulation of gas detectors. Given the description of the cell geometry, the electrostatic field configuration and the magnetic field in the gas volume it can simulate the response of the cell to ionizing particles. The electrons produced in the gas are followed along their path toward the anode wire taking into account diffusion, avalanche development and signal induction. This program can be therefore used to estimate the drift-time related to a crossing particle.

The transverse cross section of the cell was introduced describing the geometry of the I-beams and the plates with the strips and the cathodes voltages set to 1800 V and -1200 V respectively, while the anode wire was defined with a voltage of 3600 V.

The properties of the 85% Ar / 15% CO_2 gas mixture were simulated using the HEED [31] program. This package can compute the energy loss of traversing

particles for ionization in the gas volume, the number of primary and secondary electrons generated, the diffusion coefficients and the cluster size. The ejection of electrons from atoms due to the incidence of a charged particle was also considered in the simulation. When the energy of these electrons is high enough to cause further ionization (giving rise to delta-rays) the simulation of the ionization process was carried on, otherwise the electrons were simply drifted through the gas [1]. HEED also considers the emission of Auger electrons and fluorescence photons from the excited atoms. The simulation also takes into account the external parameters which can influence the drift properties of the gas, namely the pressure, the temperature and the magnetic field.

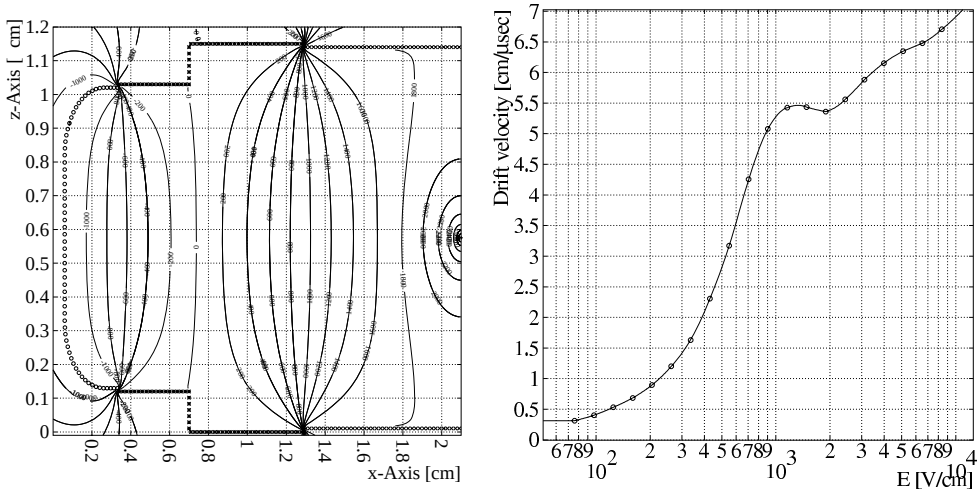

Figure 3.4: *Equipotential lines in the semi-cell (left) and drift velocity of electrons as a function of the electric field (right) computed by* GARFIELD *for the 85% Ar / 15% CO_2 gas mixture at a temperature of 293 K and a pressure of 1 atm [29].*

Figure 3.4 shows the electric potential within the cell volume. The predicted drift velocity is also shown for different values of the electric field. At the nominal field, which is around 1.9 kV/cm, the drift velocity is stable and saturates around 55 μm/ns, in agreement with the experimental measurement presented in [32, 33].

GARFIELD can be used to estimate the drift-time generated by a single track crossing the cell as a function of the track parameters and of the magnetic field. In order to parametrize the results of the simulation it was necessary to accumulate statistics for each of the simulated configurations. The detailed

[1] In order to avoid double counting, the delta-rays simulated by GEANT are not digitized since the parametrization based on the GARFIELD simulation already accounts statistically for their production (cf. Section 3.3).

simulation was therefore used to study the drift process for muons of 100 GeV/c traversing the cell at different positions along the x-axis. Steps of 0.2 mm were chosen and for each step 500 muons were simulated. Since the arrival time of the drift electrons depends on the magnetic field along the wire (B_{wire}, the field component along the negative direction of the y-axis of the superlayer, see Fig. 3.5 for details) and perpendicular to the anode wire in the radial direction of CMS (B_{norm}, component of the field along the z-axis of the superlayer) and from the impact angle of the muon, for each step along x a grid of values (reported in Table 3.1) for those parameters was chosen.

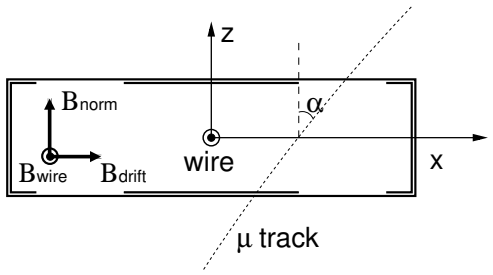

Figure 3.5: *Schematic view of the cell section illustrating the coordinate system and definition of the components of the magnetic field used by the* GARFIELD *parametrization.*

Table 3.1: *Values of the B field components parallel and perpendicular to the wire and of the impact angle used in the* GARFIELD *simulation.*

B_{norm} (T)	B_{wire} (T)	Angle (degrees)
0	0	0
0.1	0.05	±5
0.2	0.1	±10
0.35	0.2	±15
0.75	0.4	±30
		±45

The simulation of the cell was therefore repeated for each of the 275 possible combinations of these values. Note that, due to the distortion induced by the magnetic field parallel to the wire on the drift lines, it was necessary to simulate both muons with negative and positive angles in order to account for the asymmetric behavior of the cell.

The signal produced by the ionization electrons can be simulated by GARFIELD considering the charge induction on the anode, otherwise, a simplified approach can be chosen directly considering the arrival of the drift electrons.

The latter approximation is acceptable for drift cells of non-extreme resolution such the CMS DTs. The time signal was therefore chosen as the arrival time of the 5^{th} electron after a comparison with experimental data. An example of this arrival-time distribution is shown in Fig. 3.6. The width of the distribution is due to diffusion, cell non-linearities and delta-rays. To account for the asymmetry an asymmetric Gaussian fit with independent widths at each side of the maximum was performed recording, for each step of the simulation, the average value, the maximum and both sigmas of the fit.

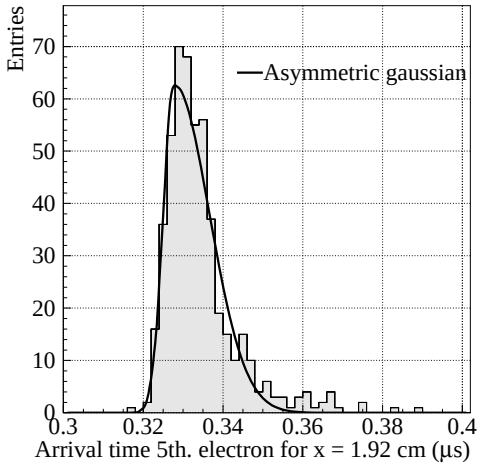

Figure 3.6: *Arrival time distribution for 500 muons crossing the cell at an angle of 30 degrees, at a distance of 1.92 cm from the wire and in a magnetic field $B_{wire} = 0.4$ T. The distribution is fitted with a double Gaussian [29].*

The behavior of the peak value of the arrival time distributions as a function of the position along the cell was used to estimate the average drift velocity in each configuration. For this purpose a linear fit was performed in the central part of the cell, between 2.5 mm and 19 mm from the anode, where the effect of the non-linearities is less pronounced. The following step was to estimate the deviation of the drift time from the linear space-time relationship. This deviation from linearity can be expressed as:

$$\Delta t = t_{sim} - \left(\frac{x}{v_d} + b \right) \tag{3.3}$$

where v_d and b are the parameters of the linear fit and t_{sim} is the peak value of the arrival time distribution. An example of the obtained non-linearities for different values of the impact angle and of the two components of the magnetic field is shown in Fig. 3.7. The deviation clearly affects mainly the regions close to the anode wire and the cathode and it is directly related to the track angle.

The field parallel to the wire has an important impact on the non-linearity while the effect of B_{norm} is almost negligible.

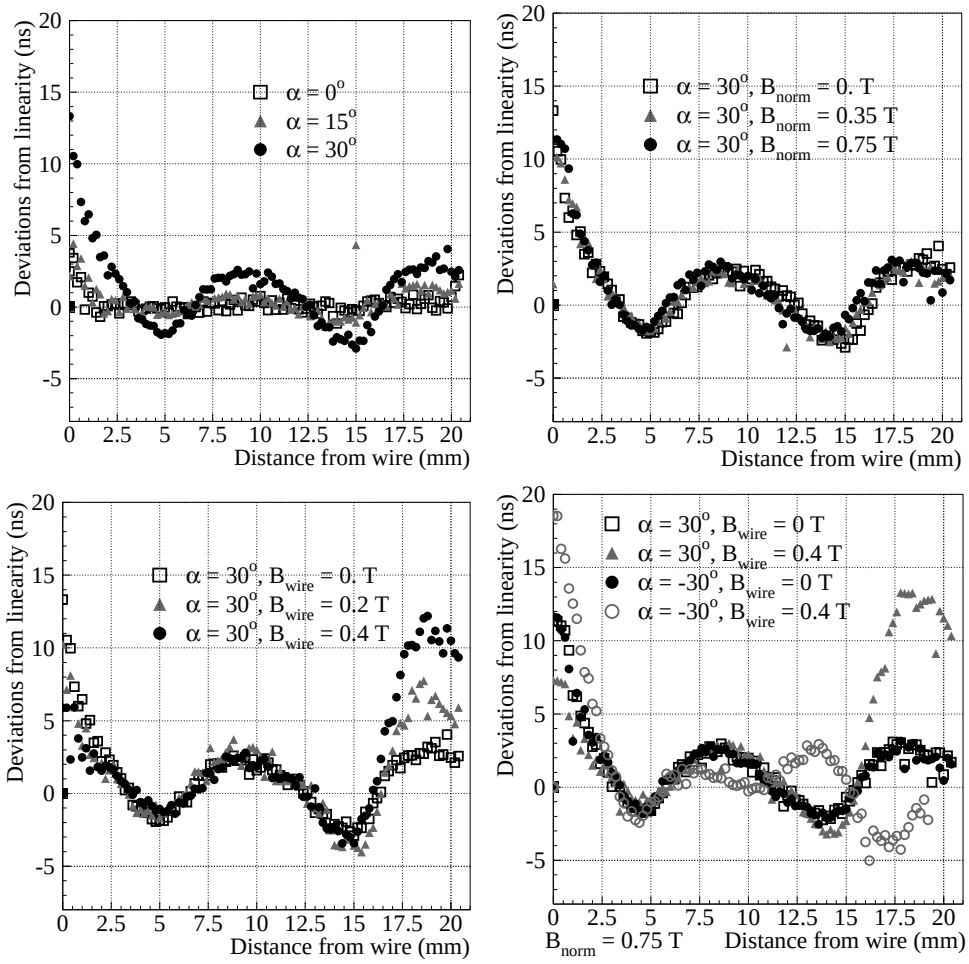

Figure 3.7: *Local deviations from the linearity of the time-space relation for different angles with no magnetic field (upper, left), different B_{norm} and B_{wire} values at 30° (upper right and lower left) and extreme cases of magnetic fields at 30° (lower, right). The asymmetry between positive and negative angles is clearly observed in the presence of B_{wire} [29].*

For each simulated configuration of angle and field a polynomial fit to the deviation from linearity $\Delta t(x)$ was performed together with the fit to the two sigma of the arrival time distribution $\sigma_p(x)$ and $\sigma_m(x)$ (the sigma toward greater and lower drift times respectively).

The complete set of functions was then used to implement a parametrization which models the drift-time distributions analogous to the one in Fig. 3.6, in order to reproduce them statistically for each crossing track. Given the po-

sition of the hit along the cell, the impact angle of the track α, and the two components of the magnetic field B_{wire} B_{norm} this function takes the nearest simulated points in the three dimensional grid $(\alpha, B_{wire}, B_{norm})$ and performs a multidimensional linear interpolation returning the estimated average drift-time and the two sigmas. An example of the output of the parametrization function

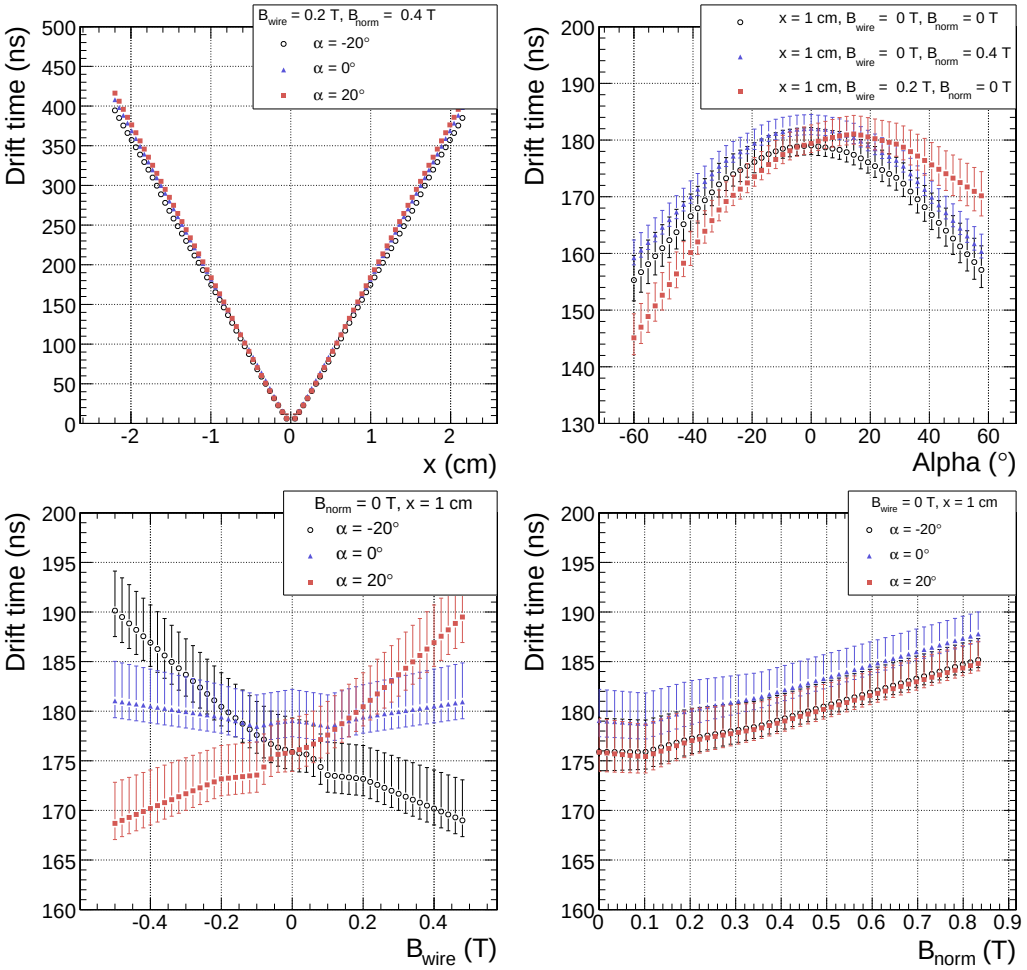

Figure 3.8: *Response of the parametrization function for various values of the input parameters. The drift time is plotted as a function of the distance from the wire (left, top), of the impact angle (right, top) and of the two components of the magnetic field B_{wire} (left, bottom) and B_{norm} (right, bottom). The error bars associated to each point correspond to the two sigma σ_p and σ_m of the drift-time distribution.*

is given in Fig. 3.8 where the drift time and the two sigmas are reported for various values of the position within the cell, the impact angle and the magnetic field.

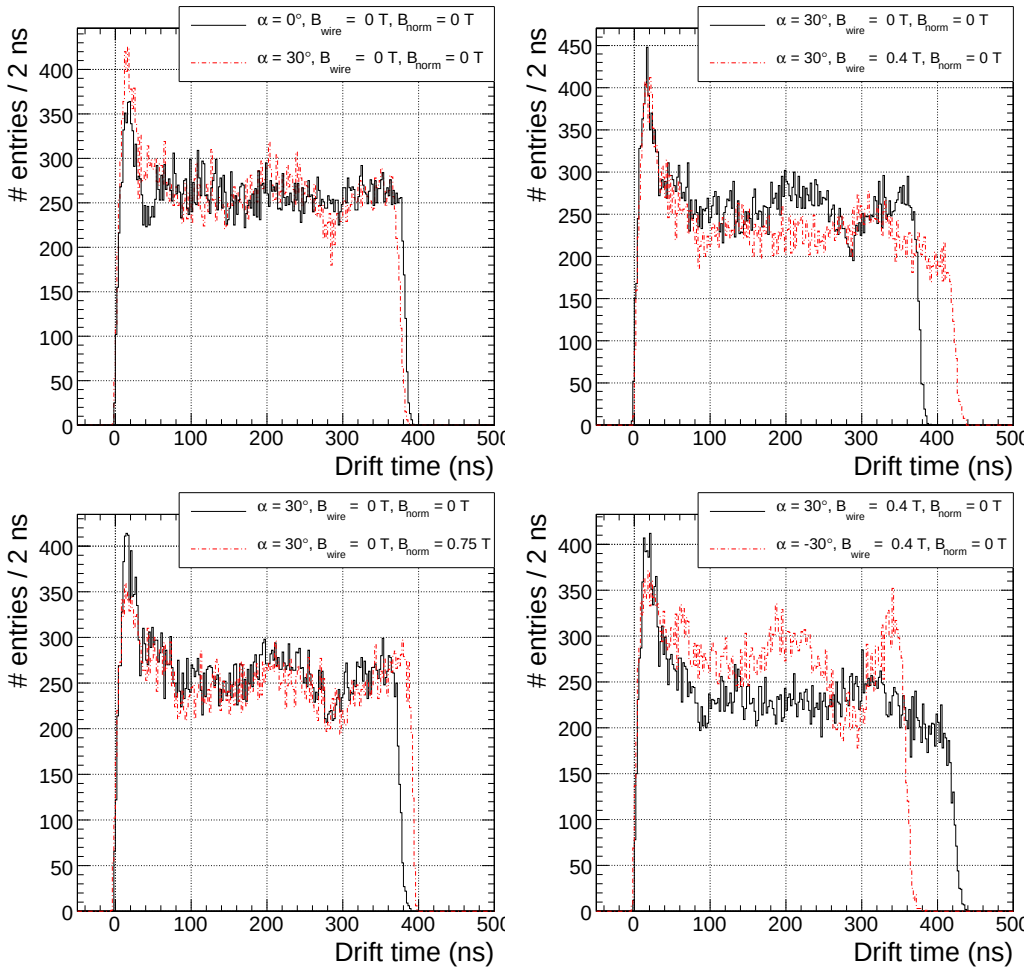

Figure 3.9: *Distributions of the drift-times obtained with the* GARFIELD *parametrization shooting muons uniformly along the cell with various values of the impact angle and of the magnetic field.*

The plots in Fig. 3.9 show the drift-time distributions obtained for various values of the input parameters, simulating tracks uniformly distributed along the cell. This distribution, usually referred as "time box" for the particular shape, reflects both the effect of the cell non linearities in the deviation from a flat behavior, and the effect of the average drift velocity which determines the width. The peak at small times is due to the field close to the anode where the drift of electrons is far from being linear.

3.2.2.2 The Parametrization in the CMS Simulation

The parametrization described in the previous section has been integrated in the framework of the official simulation of the DT detector to estimate the drift-time corresponding to the GEANT hits.

The GARFIELD simulation was considering only primary tracks crossing the full transverse section of the cell, or two adjacent borders. For this reason all particles which stop in the sensitive volume must be discarded. Also the hits from soft delta-rays produced in the gas are not digitized since their effect is already included, statistically, in the arrival time distribution simulated with GARFIELD. Details about these families of hits not directly treated in the digitization can be found in Section 3.3.

Moreover, the parametrization was available only for muons of 100 GeV but, in the simulation, is applied also to electron and positron hits independently from their energy, although this is expected to introduce only a minor effect.

The parametrization is implemented as a function of the form:

$$t_{drift}^{peak}, \sigma_p, \sigma_m = f(d, \alpha, B_{\text{wire}}, B_{\text{norm}}). \tag{3.4}$$

The distance d is defined as the distance of the hit from the wire on the plane parallel to the layer and containing the anode. The hit position provided by GEANT, coinciding with the mid point of the hit track, can be used to estimate this distance only if its z component is close to wire plane, otherwise d is computed extrapolating the direction identified by entry and exit points. However, in case of inclined tracks, if the extrapolated distances is bigger than 2.1 cm, namely outside the cell, the hit is discarded. Note that the hit tracks are approximated to straight lines not considering the bending due to the magnetic field.

As far as the impact angle is concerned, the parametrization was built considering only the two dimensional section of the cell therefore only the projection of the track in the measurement plane can be considered. As a consequence in the simulation the angle is defined as:

$$\alpha = -\arctan\frac{\Delta x}{\Delta z} \tag{3.5}$$

where Δx and Δz are the two components of the hit direction in the superlayer reference frame (cf. Section 2.4.1.1). The sign is dictated by the different choice of reference frames between the official simulation and the parametrization. The effect of the track angle along the wire direction should be evaluated with a detailed dedicated study. In fact, the number of electron-ion pairs produced in the gas by very inclined track can be sensibly higher and this may have an influence on the signal time and on the cell resolution.

The three plots in Fig. 3.10 show the distributions of the impact angle α and of the magnetic field components B_{wire} and B_{norm} for all the GEANT hits treated by the parametrization in the sample described in Section 3.2.1. The impact

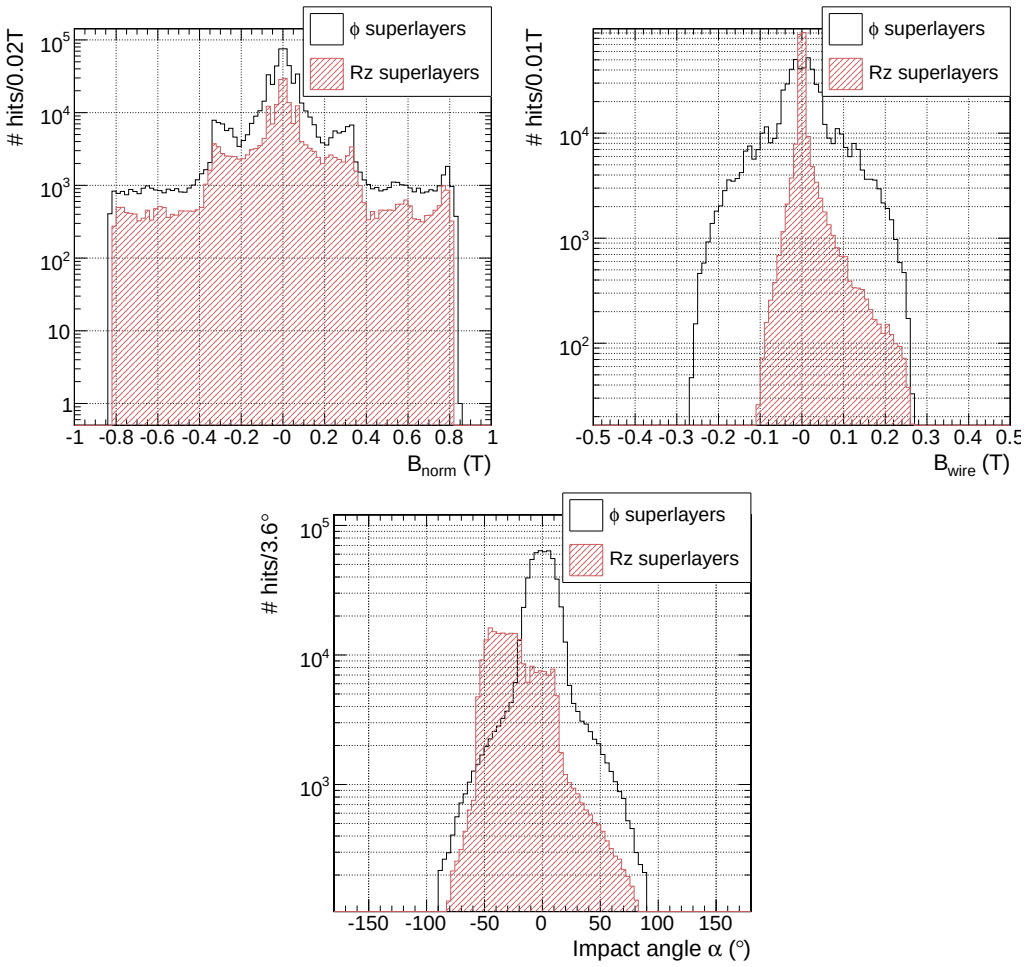

Figure 3.10: *Distribution of the input parameters B_{norm} (left), B_{wire} (right) and α (bottom) for all the hits handled by the cell parametrization.*

angle of muons with transverse momentum between 10 GeV and 100 GeV in r-ϕ superlayers is well contained between $-20°$ and $20°$ while, in the r-z superlayers of the most forward chambers, it can also reach $50°$. However, in all superlayers long tails, due to secondaries traveling almost parallel to the drift lines, are present.

The residual magnetic field in the gas volume ranges from -0.27 T and 0.28 T for the component parallel to the wires and from almost -0.8 T and 0.8 T for the component orthogonal to the anode. The asymmetry in the distributions of α and B_{wire} for the r-z superlayers is simply due to the choice of the chamber

reference frames with respect to the CMS one (cf. Section 2.4.1.1).

Note that the range of the input parameters is much wider than the one used as input in the GARFIELD simulation. For this reason for $\alpha > 45°$, $B_{\text{wire}} > 0.4$ T and $B_{\text{norm}} > 0.75$ T the parametrization functions must be extrapolated.

The drift-time t_{drift}^{peak}, corresponding to the peak of the arrival time distribution identified by the parameters d, α, B_{wire} and B_{norm}, is smeared according to a asymmetric Gaussian distribution defined by the two sigmas σ_p and σ_m. The result of the smearing is the drift-time t_{drift} assigned to the hit. At this point of the simulation all the time delays described in next section are added to t_{drift} to form the time information contained in a DT digi.

In case of several hits in the same cell, the drift times are computed independently, but separate digis are created only if the difference between the two times, at the end of the whole simulation chain, is larger than a configurable dead time (the default value is 150 ns) simulating the behavior of the readout electronics. In case of a second hit within the dead time only the first hit is recorded.

3.2.2.3 Additional Time Contributions

A DT measurement consists in a TDC time which also contains contributions other than the drift-time of the electrons in the cell. The delays and offsets which directly contribute to the measurement are:

- propagation time of the signal along the anode wire;
- time-of-flight of the muon from the interaction point to the cell;
- delays due to the cable length and read-out electronics;
- time phase due to the Level-1 trigger.

All these offsets must be estimated during the reconstruction thorough appropriate calibration and synchronization procedures. The jitter in the drift-time deriving from the uncertainties of this procedure directly contribute to the DT resolution.

In order to emulate all these contributions in the simulation the time contained in a digi is built as follows:

$$t_{digi} = t_{drift} + t_{prop} + TOF_{GEANT} + t_{offset} - TOF_{assumed} \tag{3.6}$$

The propagation time of the signal along the sense wire t_{prop} depends on the distance of the crossing particle from the front-end electronics due to the finite propagation velocity which, in the simulation, is assumed to be 0.244 m/ns. This value was directly measured using a chamber prototype tested on a muon beam [34].

The contribution of the time-of-flight (TOF_{GEANT}) of the muon from the collision vertex is directly computed by GEANT. A proper offset, multiple of 25 ns, is also added for hits coming from muons generated in a different bunch crossing than the signal one. Those hits represent the so called "out-of-time pile-up".

A time pedestal t_{offset}, which represents the delays due to cables, phases, and readout, is also added. In the real data taking this offset can be different for each channel and this difference is taken into account in the reconstruction thanks to "test pulses" sent to the front-end electronics. In the simulation there is no need for a different offset for each channel and the default value is 500 ns for all the cells.

We should note that the only important reason to introduce all these delays in the simulation is the jitter introduced by their calibration and not their absolute value. In the analysis of simulated data is extremely convenient to have all the time boxes for the different chambers aligned to the same time. This is obtained subtracting the time-of-flight of an infinite-momentum particle traveling from the nominal interaction point to the center of the chamber. This is the $TOF_{assumed}$ offset which is re-absorbed by the calibration procedure during the reconstruction. This simplification, although it doesn't have any impact on the simulated resolution, allows to simplify the handling of the inter-chamber synchronization in the whole simulation chain and this is of great importance for the emulation of the Level-1 trigger.

In the digitization the digi time is not affected by the bunch crossing assignment performed by the Level-1 emulator. In fact in p-p collisions the BX assignment is known to be correct in more than 99% of the cases. On the contrary, this feature of the simulation must be carefully considered when the simulation code is used to study the response of the DT apparatus to cosmic rays. Since cosmic muons are uniformly distributed in time, the meaning of the "correct bunch crossing" is lost and a jitter to the measured time should be added depending on the Level-1 output.

3.3 Treatment of Secondaries and Hits not Handled by the Parametrization

The GARFIELD simulation was performed only for particles crossing the whole gas layer or one corner of it, entering and exiting from two adjacent surfaces. For this reason not all the GEANT hits can be treated by the parametrization: all the tracks which cross the cell with a different topology can not be handled. As a consequence, the secondary particles produced in the aluminium which stop in the gas must be discarded while the hits from energetic secondaries crossing

the whole cell (e.g. e^+e^- from pair production and delta-rays) are treated the same way as muons.

Also the soft delta-rays produced in the sensitive volume are not digitized; in this case the reason is that they were already generated by GARFIELD and their effect is therefore included (statistically) in the parametrization of the cell.

Table 3.2 reports the relative compositions of these three families of hits distinguishing for the particle which generated the hit.

Table 3.2: *Fraction of* GEANT *hits which can be handled by the parametrization, hits produced in the gas and therefore already considered statistically in the* GARFIELD *simulation and hits which can not be treated by the parametrization. The relative contribution of the electron, positron and muon hits is also reported.*

	Parametrized	Secondaries in gas	Not parametrized
e^-	16.19%	19.12%	4.36%
e^+	3.72%	0.02%	0.49%
μ	53.97%	–	2.14%
Sub-total	73.87%	19.14%	6.99%

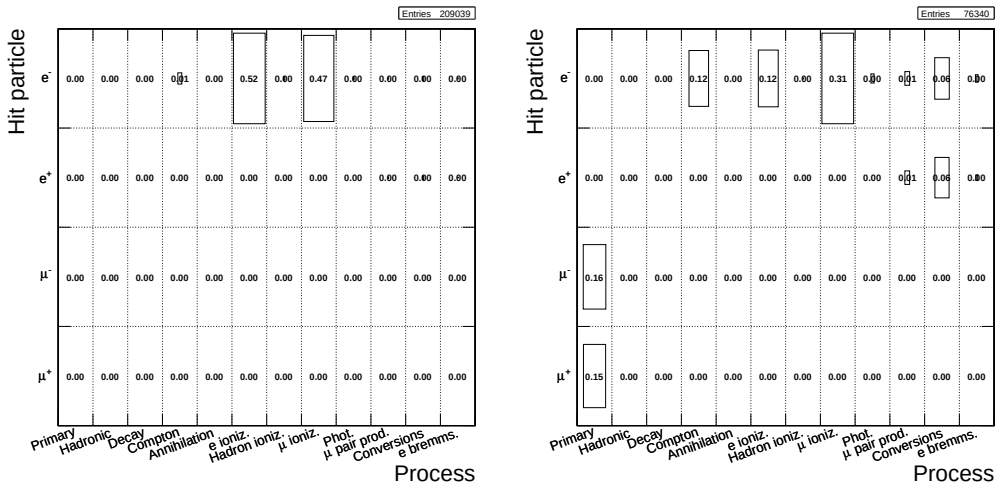

Figure 3.11: *Particle type versus generation process for the hits produced in the gas (left) and the hits which can not be handled by the parametrization (right).*

Secondaries produced in the gas. The effect of this kind of secondaries is already accounted in the GARFIELD simulation which explicitly generated

and propagated these particles within the gas volume. As a consequence they directly contribute to the width of the arrival time distributions of the drift electrons considered in the parametrization and there is no need to digitize those hits.

The processes involved in the production of these soft secondaries, which represent 19% of the total number of SimHits, are shown in the left plot of Fig. 3.11. Almost 99% of those hits is produced by electrons generated in primary and secondary ionization.

The path and the momentum distribution of these soft delta-rays have already been discussed in Section 3.2.1. Most of them, around 89%, travel less than 200 μm (see Fig. 3.3) which is a distance comparable with the resolution of the DT cell. The distribution of their position along the measurement direction is shown in Fig. 3.12.

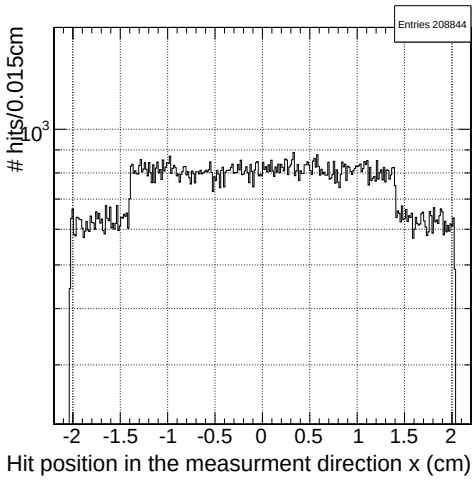

Figure 3.12: *Position within the cell, along the measurement direction, of the electron hits produced in the gas. The steps at the two sides of the cell correspond to the smallest gas volume available because of the I-beam profile.*

Hits not treated by the parametrization. All the particles which cross the cell with a topology which was not simulated by GARFIELD can not be treated by the parametrization. This is the case of:

- secondary particles produced in the aluminium which do not have enough energy to cross the whole gas layer;
- particles which, due to the bending induced by the magnetic field, enter and exit the gas volume from the same surface;
- particles crossing the cell transversally from I-beam to I-beam;

- particles crossing the cell with a big impact angle, such that their position extrapolated to the mid plane of the cell is outside the cell volume;
- particles which enter or exit the gas volume from the surfaces delimiting the tube length.

If we consider the reference sample of muons with transverse momentum between 10 and 100 GeV/c the hits which can not be digitized account for almost 7% of the total population. Their composition and the relative importance of the various processes are shown in the right plot of Fig. 3.11.

The electrons represent 62.4% of the discarded hits; most of them are delta-rays while the other relevant processes are the Compton scattering and the conversion in the aluminium plates (these three production processes account respectively for 68.8%, 18.8% and 10.4% of the e^- hits). The plots in Fig. 3.13

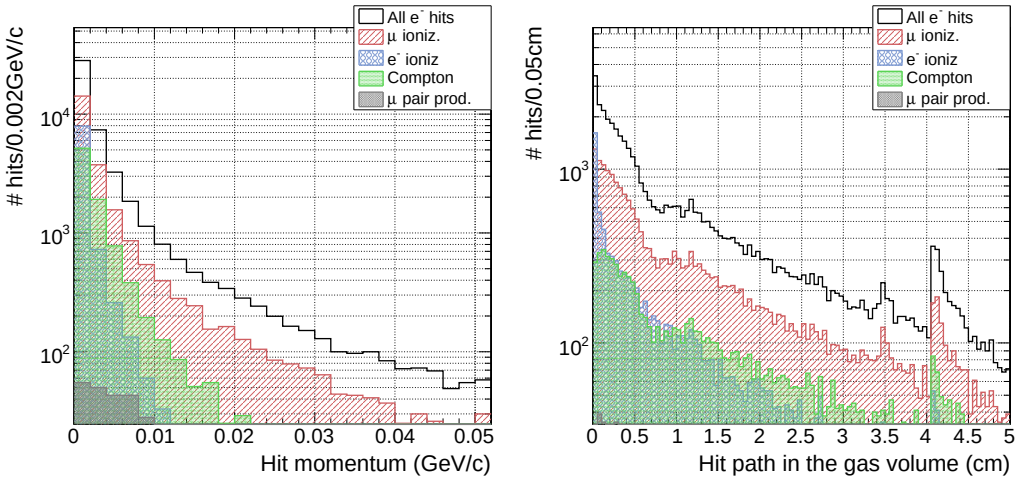

Figure 3.13: *Momentum and path in the gas volume of the electron hits which can not be handled by the parametrization.*

show the momentum and path distributions for these various component of the discarded electron hits.

A consistent fraction of the discarded electron hits (around 43%) can not be treated because it crosses the cell with a big angle, such that its extrapolated position on the wire plane falls outside the gas. The distribution of this kind of hits along the cell and their path in the gas volume are shown in Fig. 3.14. Most of these hits cross only one corner of the cell describing a short trajectory in the sensitive volume. The peak structure in the x coordinate of their position is related to particular geometry configurations for tracks crossing the whole cell almost horizontally.

Almost 38% of the e^- hits is discarded because of the particular topology due to the bending generated by the magnetic field: the entry and exit points of

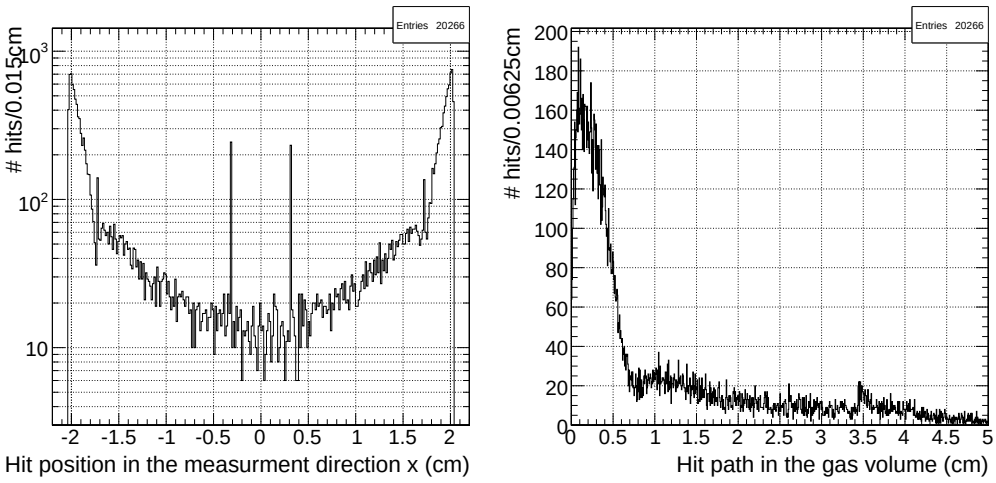

Figure 3.14: *Position along the cell and path in the gas volume of electron hits which cross the cell volume with a big impact angle. They are discarded during the digitization since their position extrapolated on the wire plane falls outside the gas volume.*

these hits are on the same side of the cell. The spectrum of momentum of these electrons is plotted, together with their path in the gas volume, in Fig. 3.15.

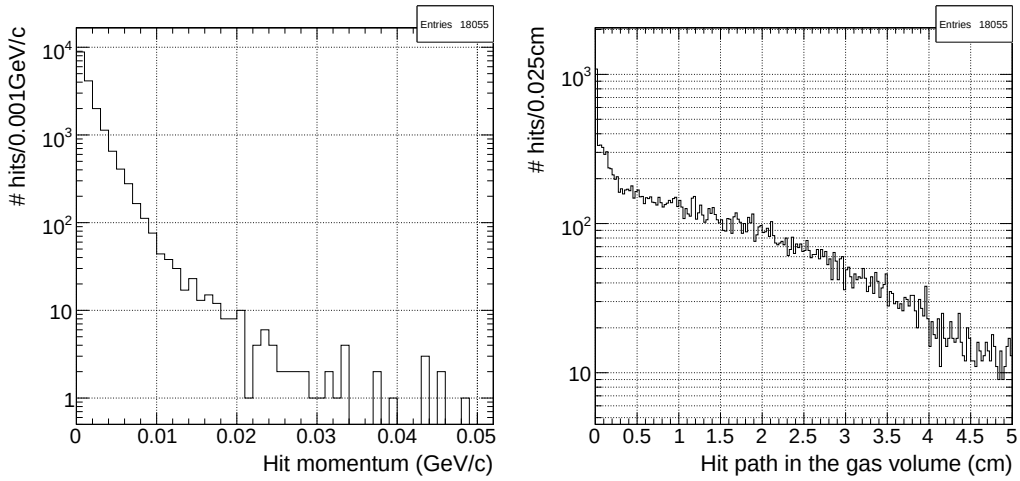

Figure 3.15: *Momentum and path in the gas volume of the electron hits which, due to the bending for the magnetic field, enter and exit the gas volume on the same side of the cell.*

The distribution of the x coordinate of their position in the gas volume is shown in Fig. 3.16. The peaks in correspondence of the I-beam feet, 6 mm before the end of the cell, are mainly due to hits which enter and exit from the same side

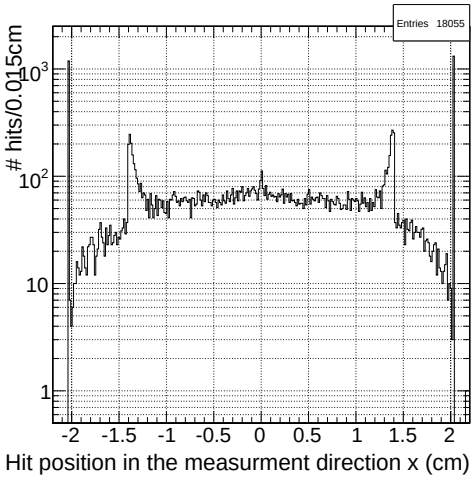

Figure 3.16: *Position within the cell, along the measurement direction, of the electron hits which enter and exit the cell volume thorough the same surface due to the bending.*

since in that point the available aluminium surface is bigger.

The electrons which are discarded because they stop their trajectories within the gas volume are 15% of the discarded hits. They are homogeneously distributed along the cell, as shown in Fig. 3.17, where their position and path are plotted.

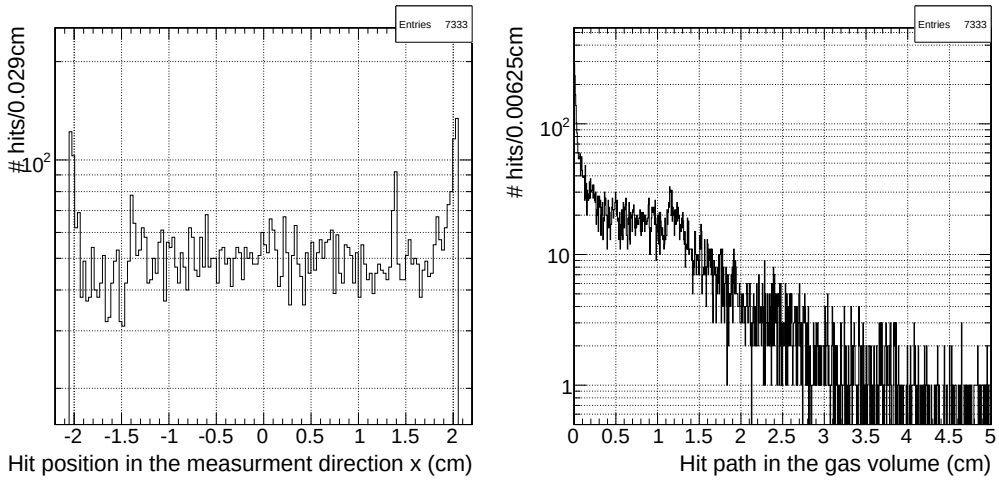

Figure 3.17: *Position along the cell and path in the gas volume of the electron hits which stop in the gas volume*

Finally, the remaining fraction of electrons, around 4%, has enough energy to cross the whole cell volume from I-beam to I-beam and they are responsible

for the tail above 4.2 cm in the hit path distributions visible in the right plots of Figures 3.3 and 3.13.

The plot on the right in Fig. 3.11 shows that an important contribution to the hits which cannot be parametrized comes from muons. Those hits, represent 30.7% of the hits discarded during the digitization and 3.8% of the muon hits totally produced.

Most of them, almost 80%, can not be parametrized because they cross only one corner of the cell with a distance from the wire which is estimated to be bigger than 2.1 cm. However, they mostly will cross the I-beam giving a hit, and therefore a digi, in the adjacent cell. Other muon hits are lost simply because they enter the gas volume from one of the surfaces delimiting the tube length. In this case it is not possible to digitize them simply because the parametrization do not consider the effect of the impact angle along this coordinate.

Note that not all the hits which account for this 7% of hits not treated by the parametrization are expected to actually produce a signal. Some of them can not be detected as their path in the gas volume is too short. Also, part of the hits which, due to the bending, enter and exit the cell from the same surface cross particular limited regions of the gas volume where the charge collection may be not efficient. Finally, even if a signal is produced this can fall in the TDC dead time, masked either by the muon hit or by other secondary particles. In conclusion, the effect of these hits on the number of digis is expected to be smaller than 7% but only a dedicated study using GARFIELD can estimate the precise contribution to the measurement.

3.4 Conclusions

A detailed simulation of the response of the DT detectors plays a key role for the understanding of the behavior of the apparatus. This chapter first presents an analysis of the output of the GEANT simulation, pointing out what are the relevant processes involved. It is then presented the modeling of the response of the drift cell in the framework of the official simulation. A parametrization obtained with GARFIELD allows to reproduce the effect of non-linearities in the drift of the electrons and the dependence of the drift velocity on the track angle and the magnetic field in the cell volume, providing an accurate description of the cell behavior.

The validation of this simulation procedure requires a detailed comparison with real data. This test has been performed exploiting the data taking on muon beam of October 2004 and the results are reported in Chapter 6. It is shown that the agreement with real data is satisfactory: the drift properties of the cell are accurately reproduced and the simulated resolution matches the one measured on real data.

This study also points to further possible improvements. Various assumptions which are now part of the simulation should be carefully checked:

- the parametrization is obtained simulating only muons crossing the cell but it is currently used to model the response to all kind of particles;
- the effect of the track inclination in the non-measurement plane is currently ignored since it was not simulated with GARFIELD;
- the measured time is currently determined by the arrival of the fifth electron in the GARFIELD simulation; this choice, although determined comparing the results with the real data, is not optimal, especially for signals in the multiplication region close to the anode. A more precise result can be obtained simulating with GARFIELD the signal induced on the wire and the response of the electronics with an appropriate threshold.

Also, a fraction of the GEANT hits can not be handled by the parametrization. It is shown that these hits are about 7% of the total and only a fraction of them is expected to give a detectable signal in the apparatus; we therefore expect this contribution to be almost negligible. However, to distinguish the fraction of hits which could produce a signal on the wire a dedicated study with GARFIELD is needed. The solution for the hits which can contribute to the measurement consists in the explicit generation of clusters along the track trajectory; drift times are then calculated by means of an interpolation table (a "time map"), to be obtained with GARFIELD, which relates the position of the clusters with the arrival time of the drift electrons.

Another possible improvement is the simulation of cell inefficiencies and after-pulses which are due to photo-electric extraction of electrons from the cathodes and strips. The impact of these effects is studied in Chapter 6 and it has been shown to be negligible.

Finally it is worth noticing that the whole simulation chain described in this chapter has been designed for bunched muons produced in LHC *p*-*p* collisions. Particular care should be therefore paid when this is used for the simulation of muons with a different time structure. This is the case of cosmics muons which have a flat arrival time distribution; the delays for the time-of-flight and the bunch crossing assignment performed by the Level-1 trigger must be accurately simulated because of their direct impact on the measured time.

Chapter 4

Local Reconstruction in the DT Detectors

The main purpose of this chapter is to describe the local reconstruction in the DT detectors. This is the reconstruction step where basic hits are built starting from the output of the Data Acquisition System.

The local reconstruction begins building mono-dimensional hits in single drift cells. The only information contained in these hits is the distance from the wire, with an intrinsic left/right ambiguity and without any information about their position along the tube.

The cell hits are the basic ingredients for the reconstruction of segments separately in the r-ϕ and r-z projections. These two-dimensional segments still do not provide any information about the coordinate parallel to the sense wires but they add the knowledge about the track angle projected in the measurement plane.

Combining the two projections, it is possible to reconstruct the three-dimensional information about the track crossing the chamber. The resulting three-dimensional segments are used in the following reconstruction steps to fit the muon track in the CMS spectrometer.

The pattern recognition during the segment building allows to solve the intrinsic left-right ambiguity of mono-dimensional hits using goodness-of-fit criteria to discriminate between the different hypothesis. Also, the segment reconstruction helps discriminating electromagnetic debris accompanying high energy muons. As long as low energy electrons are produced, the measurement in two consecutive layers are decoupled by the 2 mm thick aluminium wall ($0.022\ X_0$) of the drift tubes. In this case, the pattern recognition allows the rejection of most of the hits caused by secondaries inside a cell. The situation is quite different in case of hard electromagnetic activity, such as muon bremsstrahlung; if the shower spans over several cells and layers the local reconstruction can be heavily affected by the large hit multiplicity.

In the following all the steps leading to the reconstruction of three-dimensional segments within the chambers, starting from the TDC measurements, are described.

4.1 Input to the Local Reconstruction

The input to the local reconstruction are TDC measurements stored in the so called "digis". During the real data taking the DT digis are created directly from the raw output of the Data Acquisition (DAQ) System while, in case of simulated samples, they are created through the digitization procedure, described in Section 3.2.2, starting from the GEANT hits in the cell volume. In both cases, the time information contained in a digi is not limited to the drift-time of the electrons in the cell but it also contains other contributions: the time-of-flight of the muon from the interaction point to the cell, the propagation time of the signal along the anode wire, an offset due to the cable and electronic delays and an arbitrary phase due to the trigger. These additional contributions are accounted in the simulation as described in Section 3.2.2.3.

A synchronization procedure must be therefore applied to the digis in order to extract the drift time, which is the relevant information for the hit reconstruction. This procedure must be flexible enough to treat both real and simulated data under different running conditions, such as exposure to cosmic rays, to a test beam and in p-p collisions.

4.1.1 Synchronization of Real Data

The extraction of the drift-time from the TDC measurement, in case of real data, is performed in several consecutive steps:

- the measured TDC times are corrected for the relative offset due to the different signal path lengths to the readout electronics of each wire. This relative difference is measured for each wire sending simultaneous "test-pulses" to the front-end of a group of wires and registering the measured times called t_0, as described in Section 5.1.1. Once the t_0 is subtracted, the resulting TDC times for the different channels within the chamber are synchronized among them;

- the absolute offset of the drift-time distribution is computed. This offset, called t_{trig} because of its dependence on the trigger latency, allows to extract the drift-time from the TDC measurement. The usual choice is to determine a t_{trig} pedestal for each superlayer using the procedure described in Section 5.1.2.

Because of the way it is computed, the t_{trig} offset already accounts for the average time-of-flight of the muons which crossed the superlayer and the average time for the signal propagation along the anode wire. In case of p-p collisions, if the chamber is uniformly illuminated, the average TOF will be equivalent, as a first approximation, to that of a muon crossing the superlayer center. Also, the average time for the signal propagation along the wire can be considered as the time which a signal takes to travel from the mid of the wire to the front-end electronics.

Further corrections for these two quantities can be computed as soon as the three-dimensional hit position within the chamber is known, namely when the hit has been used to build a 3D segment. This is done iteratively during the reconstruction, refining the knowledge of the drift-time on an event by event basis:

- the hit position is used to correct the synchronization for the difference in the time-of-flight of an infinite-momentum particle traveling to the superlayer center and one traveling to the actual hit position;
- the hit coordinate along the wire is used to correct the propagation time with respect to the mid of the wire, assuming a propagation velocity of 0.244 m/ns, as directly measured on test-beam data [34].

These corrections can be adapted or switched off in case of different running conditions. This is the case of cosmic data, where the previous definition of the time-of-flight can not be applied, or test-beam data, where the chamber is usually not uniformly illuminated. Therefore, particular care have been taken to provide this flexibility.

4.1.2 Synchronization of Simulated Data

The same synchronization procedure described for the real data can be applied also to simulated events. It is however un-practical to set in the simulation different time pedestals for each channel; therefore the offset simulating the cable and electronic delays has the same value for all the wires and it does not depend on the Level-1 trigger synchronization, as described in Section 3.2.2.3.

It is also possible to use in the reconstruction the exact knowledge of the time pedestals set during the digitization without computing and using the calibration constants as done for real data. In this case the uncertainties deriving from the calibration of the t_0 and t_{trig} pedestals, are not accounted in the reconstruction of simulated events.

As far as the time-of-flight and signal propagation along the anode wire are concerned, the same iterative procedure adopted for real data is applied: the synchronization is refined event-by-event computing corrections as soon as better information about the three-dimensional hit position become available.

4.2 Reconstruction of Hit Positions within the Cell

The primary objects that result from the DT local reconstruction are points in the cell volume also called "RecHits". These objects are built computing the drift distance corresponding to the measured drift-time. This requires the knowledge of the average drift velocity in the cell, possibly considering its dependence on the residual magnetic field and on the track angle.

Two reconstruction algorithms have been developed in the CMS software, one that uses a constant drift velocity over the entire cell, and another based on a time-to-distance parametrization obtained using a GARFIELD [30] simulation of the cell behavior. The latter takes into account the dependence of the drift velocity and of the cell non-linearities on the track angle and the residual magnetic field, already discussed in Section 3.2.2.1, thus achieving better resolution. The two reconstruction algorithms are described in Sections 4.2.1 and 4.2.2 respectively.

The input parameters of the cell parametrization and the corrections for the synchronization constants, such as the time-of-flight and the signal propagation along the wire, can not be computed for the individual digi which only contains the information about the hit distance from the wire. For this reason an iterative reconstruction procedure is adopted:

- *first step*: reconstruction at the cell level: left-right ambiguity and position along the wire not yet determined;

- *second step*: the hit is used to build a segment at superlayer level. The left-right ambiguity is solved. Using the parametrization the hit position can be recomputed using the impact angle which is then known;

- *third step*: the hit is used to fit a three-dimensional segment with both r-ϕ and r-z projections. At this point, also the position along the wire is determined and can be used for a more precise estimation of the residual magnetic field which may change along the tube. Also the synchronization offsets due to the TOF and the signal propagation along the wire can be recomputed and the resulting drift-time is used for improved computation of the distance from the wire.

In summary, the initial reconstruction at the cell level gives the input hits used to find a segment. When the segment is built the position of the hits is further refined to finally obtain the best fit.

In order to discard noise and pile-up signals, the reconstruction is performed only for drift-times falling in a user-defined time window: usually the times are

required to be within -3 and 415 ns. All other digis are discarded and the reconstruction is not attempted.

4.2.1 Reconstruction with Constant Drift Velocity

The good linearity of the drift field within the cell allows to reconstruct the distance from the wire associated to a certain drift-time using a constant drift velocity (v_{drift}) over the entire cell:

$$x = v_{drift} t_{drift}. \tag{4.1}$$

The drift velocity is estimated with the calibration procedure, based on the meantimer technique, described in Section 5.2. The same procedure also allows to calculate the error assigned to the reconstructed hits.

Although using a constant drift velocity does not account for local variations of the magnetic field in the tube or for different impact angle of each track, the calibration procedure allows to find an average drift velocity which best fits the working conditions of a group of cells; normally, a different drift velocity for different superlayers is used.

Such simple reconstruction algorithm allows satisfactory results especially for tracks with small impact angles and in regions with low residual magnetic field, as in these cases the cell non-linearities are less important.

For this algorithm, the three-step reconstruction procedure described above is only used for the refinement of the synchronization constants.

4.2.2 Reconstruction Using the Cell Parametrization

The optimum cell resolution can be achieved taking into account the dependence of the drift velocity on track parameters and magnetic field, as the impact angle of the crossing track and the residual magnetic field in the gas volume affect the drift-times as already described in Section 3.2.2.1.

These effects are not considered by the algorithm described in the previous section, where the calibration can only account for the average impact on the drift velocity but not for the non-linearities and the variation of the magnetic field along the tube.

For this reason, an existing parametrization, obtained from the same GARFIELD simulation described in Section 3.2.2, has been used to implement a reconstruction algorithm which computes the drift distance considering its dependence not only on the drift-time, but also on the track angle (α) and on the components of the magnetic field parallel (B_{wire}) and perpendicular (B_{norm}) to the wire in the radial direction with respect to the CMS center.

GARFIELD **simulation and time-to-distance parametrization.** The data obtained from the detailed simulation of the drift cell with GARFIELD were also used to build a parametrization of the time-to-distance relation which can be used in the reconstruction of the distance of the hit from the anode wire.

The procedure described in Section 3.2.2 provides and estimate of the average drift velocity (v_d) of the ionization electrons and a function $\Delta t(x)$ describing the deviations from a linear space-time relation. This function was then inverted obtaining the function $\Delta x(t)$ which can be used to compute the deviations from linearity in position for a given drift time. The plot in Fig. 4.1 shows an example of this function for the extreme case of $B_{\text{norm}} = 0.75$ T, $B_{\text{wire}} = 0.40$ T and an impact angle of 30°.

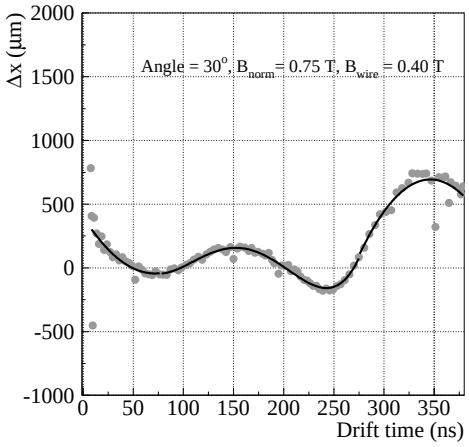

Figure 4.1: *Deviations from linearity in the time to distance relation. Dots are the result of the simulation while the continuous line is the polynomial function used in the parametrization [29].*

The distance (x^{mode}) from the wire associated to the peak-time t^{peak}_{drift} can be computed with the relation:

$$x^{mode} = (v_d t^{peak}_{drift} + b) + \Delta x. \tag{4.2}$$

As an indication of the uncertainty, the two sigmas $\sigma^x_p(t)$ and $\sigma^x_n(t)$ are also obtained inverting the relations $\sigma^t_p(x)$ and $\sigma^t_n(x)$ which describe the width of the asymmetric Gaussian fit of the drift-time distribution.

The complete set of functions referring to the various simulated configurations was then used to build a parametrization which, given a certain drift-time, the impact angle α and the two components of the magnetic field B_{wire} and B_{norm}, computes the corresponding distance from the wire taking the closest point in the (α, B_{wire}, B_{norm}) grid and performing a multidimensional linear interpolation.

Reconstruction using the time-to-distance parametrization. The parametrization described in the previous section is used in the reconstruction of the hit distance from the wire.

Reconstruction requires the knowledge of the *average* distance from the wire associated with a certain drift-time. This is information is not what is directly provided by the parametrization described above; in fact, the relation in eq. 4.2 returns the distance from the anode of a track which would give an arrival time distribution with a peak at the time t_{drift}^{peak}.

It is however possible to use the parametrization to estimate the mean value of the drift-distance distribution given the peak (the "mode") and the two sigmas. For the assumed asymmetric Gaussian shape, the relation between the mean and the mode is:

$$x_{drift}^{mean} = x_{drift}^{mode} - (\sigma_p - \sigma_n)\sqrt{\frac{2}{\pi}}. \tag{4.3}$$

Note that this is an approximation of the actual value since the detailed treatment would require to use the GARFIELD simulation to build the distribution of the distances from the wire resulting in a certain drift-time. However, the effect of this approximation is expected to be small in all the regions of the cell where the width of the distribution is slowly varying moving on the cell axis. The only region where this condition is not matched is the one close to the anode, where important variations of the drift field over a small distance can heavily affect the shape of the distribution.

The resulting parametrization has been implemented in the framework of the official CMS reconstruction code as a function of the form:

$$x_{\text{drift}} = f(t_{\text{drift}}, B_{\text{wire}}, B_{\text{norm}}, \alpha) \tag{4.4}$$

where x_{drift} is the drift-distance, t_{drift} the drift-time, B_{wire} and B_{norm}, the components of the $\vec{B}$ field parallel and perpendicular, respectively, to the wire and α the projection of the impact angle in the measurement direction. (cf. Fig. 3.5 for the definition of the reference frame used by the parametrization). Note that, because of the way the GARFIELD simulation was performed, no information is available on the effect of the track angle with respect to the wire direction.

Since B_{wire}, B_{norm}, and α are not known at the level of the individual hit, the three-step reconstruction procedure previously described is implemented. The first step assumes a crude estimate of the input parameters of the parametrization: the field at the middle of the wire is used and the track is assumed to be vertical in the r-ϕ superlayers and to point toward the interaction point in the r-z superlayer. At this stage, also the correction for the signal propagation along the wire and for the TOF of the muon are computed assuming the hit coordinate not directly measured to coincide with the mid-point of the wire.

The hit is then updated twice: after it has been used to build a 2D r-ϕ or r-z segment (second step) and after it has been used in the 3D segment fit (third step). At the second step the angle of the segment is used to update the RecHit position. Finally, in the last step the knowledge of the hit position along the wire is used to evaluate the magnetic field and the x_{drift} is computed again providing improved parameters to the function 4.4. The knowledge of the three-dimensional position of the hit also allows to refine the synchronization of the digi-time (cf. Section 4.1).

The values of the two sigmas $\sigma_p^x(t)$ and $\sigma_n^x(t)$ are not related to the actual error to be assigned to the measurement, as they are only the translation of the width of the arrival time distributions into a distance. The actual errors assigned to the reconstructed hits is therefore estimated from the residual distributions obtained comparing the distances from the wire of simulated GEANT hits and RecHits. Gaussian fits have been performed and the corresponding sigmas recorded. The errors computed in such a way are different for each reconstruction step and for r-ϕ and r-z superlayers. For the latter view also the dependence on the wheel number is considered since it is directly related to the track impact angle. It should be noted that, in this way, no dependence of the error on the hit position within the cell is taken into account. The error values for the different cases are reported in Table 4.1. At the third reconstruction step the uncertainty on the reconstructed distance is similar for all the superlayer types in the different wheels.

Table 4.1: *Errors (in μm) assigned to one dimensional RecHits reconstructed using the drift time parametrization at various reconstruction steps for different types of superlayers and wheel positions. These errors are obtained from a Gaussian fit of the residual distribution of the reconstructed drift distance.*

	Superlayer type			
	r-ϕ	r-z, **Wheel** 0	r-z, **Wheel** ±1	r-z, **Wheel** ±2
Step 1	200	221	302	315
Step 2	188	220	252	258
Step 3	142	146	167	167

4.2.3 Performance of the Hit Reconstruction

The goal of this section is to show the performance of the hit reconstruction on simulated data: the reconstruction is performed using the GARFIELD parametrization and the synchronization constants are taken from the Monte Carlo truth as described in Section 4.1.2. Note that, when comparing the results

presented here with those obtained on real data the contribution to the resolution deriving from the accuracy in the computation of the t_0 and t_{trig} delays should also be added. The simulated sample used for this study is constituted by 10000 single muon events generated with a flat p_T spectrum in the range 10-100 GeV/c.

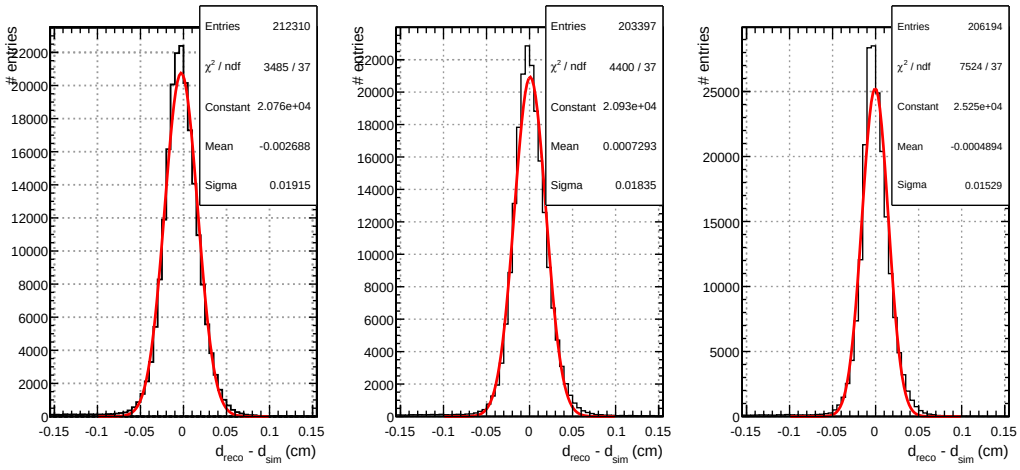

Figure 4.2: *Residuals between the reconstructed and the simulated hit distances from the wire. The 3 plots refer to the first (left) second (center) and third (right) reconstruction step of the drift time parametrization in superlayers r-ϕ.*

The plots in Fig. 4.2 show the resolution on the distance from the wire for hits reconstructed in the DT cells of r-ϕ superlayers. The distribution is described by a Gaussian and the mean value and the sigma resulting from the fits are reported in Table 4.2 for the r-ϕ superlayers and for the the r-z ones in the different wheels.

Table 4.2: *Residuals between the reconstructed and the simulated hit distances from the wire. The mean value (μm) and the sigma (μm) of the Gaussian fit are reported for the three reconstruction steps with the drift-time parametrization in r-ϕ and r-z superlayers.*

	Superlayer type							
	r-ϕ		r-z, **Wheel** 0		r-z, **Wheel** ±1		r-z, **Wheel** ±2	
	mean	σ	mean	σ	mean	σ	mean	σ
Step 1	-27	191	7	222	7	240	-6	274
Step 2	7	183	7	222	7	239	-4	275
Step 3	-4	153	-5	146	-3	163	-9	171

The width of the residuals grows moving toward the outermost wheels in the r-z superlayers. This is due to the impact angle of muons which, in the cells measuring the angle with respect to the beam line, increases with the pseudorapidity enhancing the effect of the cell non-linearities. This effect is less pronounced at the second and third reconstruction steps where the knowledge of the segment angle can be used in the parametrization. The final resolution is below 170 μm in all the chambers.

The tails of the residual distributions are non-Gaussian and asymmetric as visible, for example, in Fig. 4.3 which shows again the resolution of the first reconstruction step in r-ϕ superlayers. The long tail toward negative values is

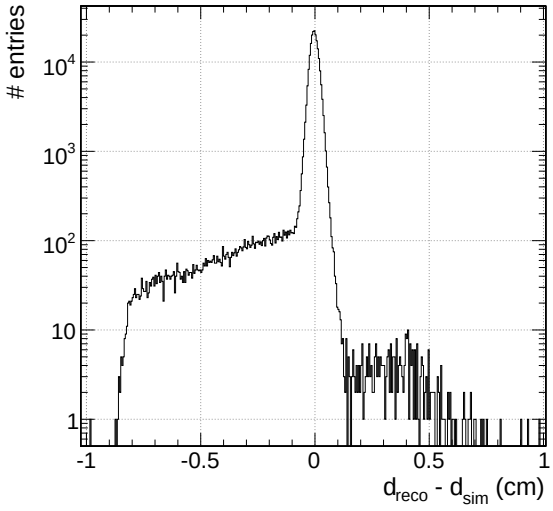

Figure 4.3: *Residuals between the reconstructed and the simulated hit distances from the wire. The plot refers to the first reconstruction step using the drift-time parametrization in superlayers r-ϕ.*

due to the delta-rays and secondary hits from electromagnetic debris in general. In fact, due to the dead time of the TDC, only the hits giving drift-times smaller than the muon one can be detected. The tail drops sharply around 8.1 mm which, considering an average drift velocity of about 54 μm/ns, correspond to the 150 ns dead time set in the digitization (cf. Section 3.3). In fact, after this time offset, the muon hit can be detected again and, therefore, selected by the pattern recognition.

The effect of the refinement of the synchronization constants as soon as the three-dimensional hit position is known is illustrated in Fig. 4.4. The plot on the left shows the dependence of the residuals on the pseudorapidity at the first reconstruction step. The pattern, although confused by the different η regions covered by the different stations which are plotted altogether, is due

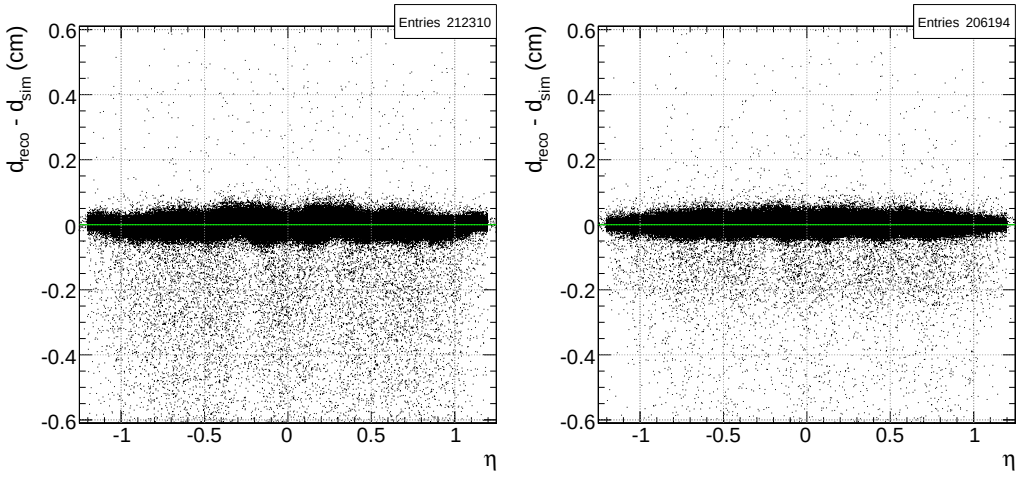

Figure 4.4: *Residuals on the distance from the wire as a function of the pseudorapidity (η). The plots are referred to the first (left) and the last (right) reconstruction step using the the drift-time parametrization in superlayers r-ϕ.*

to the interplay of the approximation made to estimate the time-of-flight and the signal propagation along the wire. At this step, in fact, the hit position along the wire is considered to be in the middle of the anode wire. At the last reconstruction step, (plot on the right) the three-dimensional position of the hit is estimated combining the two measurement projections thus reducing the effect of the synchronization constants on the residual distribution.

The error assignment on the reconstructed position plays an important role in the segment reconstruction since the whole pattern recognition is based on quality selection exploiting the χ^2 of the linear fit. The plots in Fig. 4.5 show the pull distributions for the three reconstruction steps in the r-ϕ superlayers assuming, for the reconstructed hits, the errors given in Table 4.1. The parameters of the Gaussian fit to the distributions are reported in Table 4.3 also for r-z superlayers. The shape of the pull distributions is not perfectly Gaussian since the assignment of a uniform error along the whole cell is not the ideal choice due to the presence of critical regions, like the one close to the anode, where the drift-time distribution is affected by non-linearities. However, the width of the distribution is compatible with 1 in all the chambers.

The efficiency in the reconstruction of the hits within the cell is on average higher than 99%. The plot in Fig. 4.6 shows the efficiency in r-ϕ superlayers as a function of the pseudorapidity. The effect of the transitions between the wheels is visible even if the structure of the drops in the efficiency is complicated because of the different η regions covered by the different stations.

As far as the reconstruction using a constant drift velocity is concerned, it is interesting to compare the behavior of this reconstruction algorithm with

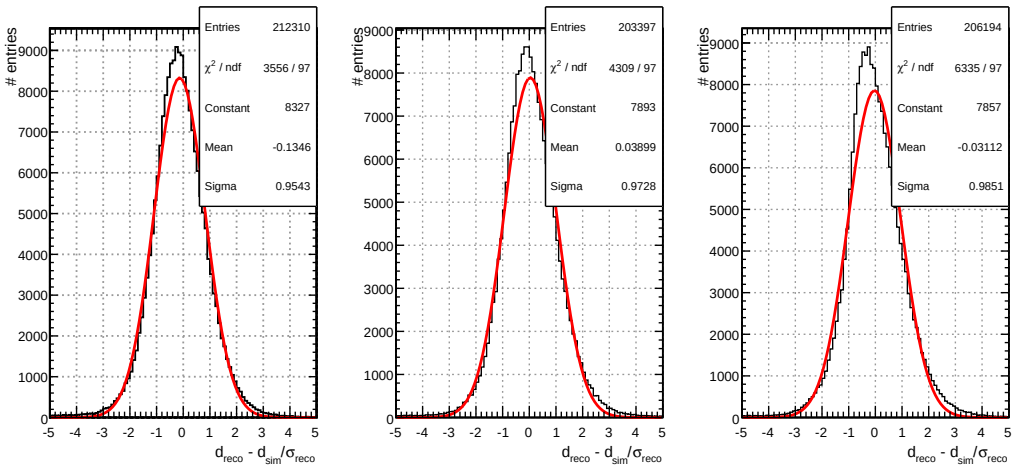

Figure 4.5: *Pulls for reconstructed distance from the wire. The 3 plots refer to the first (left) second (center) and third (right) reconstruction step of the drift time parametrization in superlayers r-ϕ.*

Table 4.3: *Pulls for reconstructed distance from the wire. The mean value and the sigmas of the Gaussian fit are reported for the three reconstruction steps with the drift-time parametrization in r-ϕ and r-z superlayers.*

	Superlayer type							
	r-ϕ		*r*-*z*, **Wheel** 0		*r*-*z*, **Wheel** $\pm$1		*r*-*z*, **Wheel** $\pm$2	
	mean	σ	mean	σ	mean	σ	mean	σ
Step 1	-0.134	0.954	0.029	1.001	0.023	0.792	-0.020	0.873
Step 2	0.039	0.973	0.032	1.003	0.028	0.946	-0.016	1.067
Step 3	-0.031	0.985	-0.037	0.992	-0.021	0.967	-0.058	1.019

that of the GARFIELD parametrization in case of large non-linearities. The plots in Fig. 4.7 show the residuals between the reconstructed and simulated distance from the wire as a function of the simulated one. They are referred to the first reconstruction step in *r*-*z* superlayers of wheels +2 and -2, where the large impact angle and the non-negligible magnetic field enhance the effect of the non-linearities in the drift of electrons. The plot on the left shows the results obtained using the drift-time parametrization while the one on the right shows the performance of the constant drift velocity method. In the first case, the effect of the non-linearities is well contained below 100 μm also in the most problematic region which is the one close to the anode. The situation is completely different in the plot on the right where the average value of the residuals can vary of more than 150 μm moving a few millimeters away from

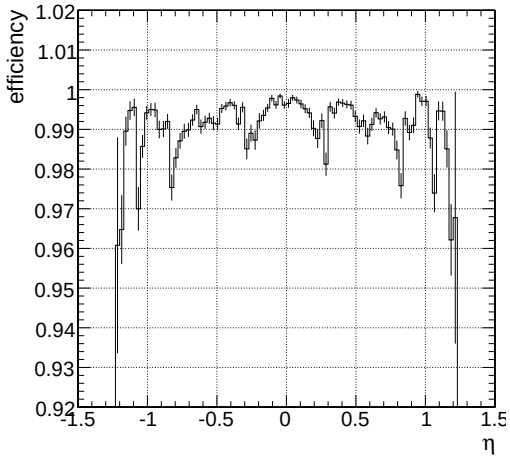

Figure 4.6: *Efficiency of RecHit reconstruction as a function of the pseudorapidity. The plot refers to the first reconstruction step of the drift time parametrization in superlayers r-ϕ.*

the anode. It is worth to notice that the effect is much less important in the

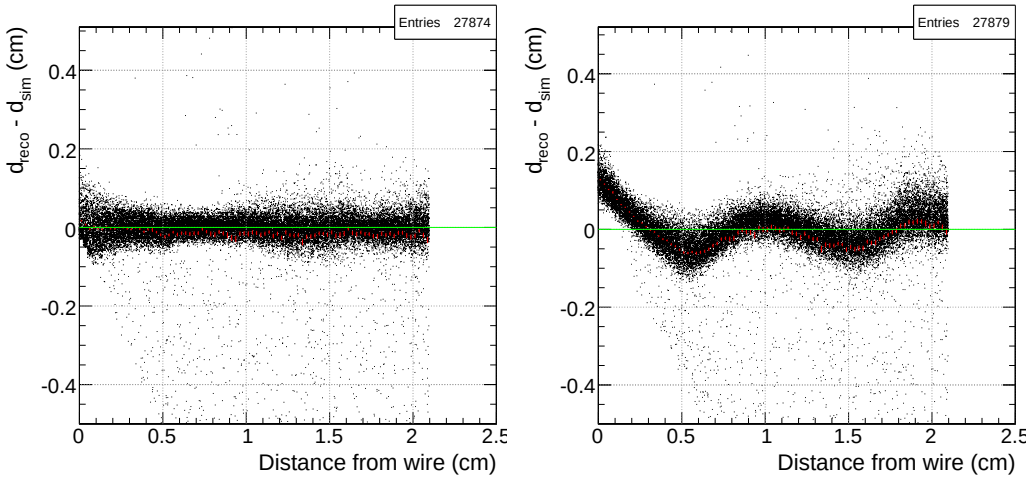

Figure 4.7: *Residuals between the reconstructed and simulated distance from the wire as a function of the simulated one. The plots are referred to hits reconstructed using the time-to-distance parametrization (left) and the constant drift velocity (right) in r-z superlayers of wheels ±2.*

r-ϕ superlayers and in the r-z superlayers of the central wheel where the impact angles are on average smaller.

4.3 Segment Reconstruction

Under ideal circumstances, a muon from the interaction region traversing the chamber will give rise to twelve hits, one in each of the layers. In practice some hits may be missing due to inefficiencies, large angle tracks may give rise to two hits in adjacent cells of the same layer and there may be additional hits due to background from electromagnetic debris, neutrons, and noise. The purpose of the segment building procedure is twofold: first, to identify which of the reconstructed hits stem from the muon track and, second, to resolve the left-right ambiguity for each of these. Moreover, the combined use of many hits allows an increase in the spatial resolution of the DT chambers, and reduces the combinatorics to be dealt with in track reconstruction. Last, but not least, the reconstruction of a segment allows a precise determination of the impact angle on the chamber and of the hit position along the wire, allowing the refinement of the computation of the drift distance (cf. Section 4.2).

The segment reconstruction acts on the r-ϕ and r-z projections independently: only at the end of the procedure the two projections are combined and a three-dimensional segment is built. The reconstruction in each projection is an exercise of pattern recognition and linear fitting, with the complication of left-right ambiguity. The reconstruction is performed in three steps:

- segment candidates are built from sets of aligned hits;
- the best segments among those sharing hits are selected, solving conflicts and suppressing ghosts;
- the hit reconstruction is then updated using the information from the segment and the segments themselves are eventually re-fitted.

Building segment candidates. The first step begins by selecting pairs of hits in different layers, staring from the most separated. For each pair the reconstruction of a segment candidate is then attempted.

Both hypotheses, left and right, are considered and the pair is kept if the angle of this proto-segment is compatible with a track pointing to the nominal interaction point with a tolerance of 0.1 rad for the r-z projection and 1.0 rad for the r-ϕ ones since this is the projection interested by the track bending.

For each pair, additional compatible hits are searched for in all layers checking if the left and right hypothesis have a distance from the extrapolated segment smaller than 10 times the position error, as estimated by the hit building algorithm. It is possible that the left and right hypotheses are both compatible with the segment. In this case, the ambiguity is solved later and both candidates are retained. If a muon passes close to the I-beam separating two cells it can

generate a signal in both. In this case, both hits are considered for that layer, in order to avoid any bias.

Once the pattern recognition is completed each collection of hits is fitted using the position and the error assigned to the hits. For each seed (*i.e.* pair of hits) only the segment candidate with the maximum number of hits and the minimum χ^2 is retained; all the others are rejected. Finally, a quality criterion is applied, requiring the number of hits ≥ 3 and the χ^2/d.o.f. < 20 for all the candidates.

The same algorithm is applied for a single superlayer r-z or, in the case of the r-ϕ projection, for two superlayers, considering all 8 layers together.

In case of showering, the occupancy in the chamber can be extremely high leading to an explosion of the combinatorics which can deteriorate the performance of the pattern recognition. For this reason the segment building is not attempted if the number of hits in a given projection is greater than a predefined number (default is 100). In this case a different way of reconstructing segments should be put in place.

Segment selection. The pattern recognition described above produces a set of segment candidates. A consistency check is performed in order to test whether two segments use different hypothesis for the same left-right hit pair. In this case, the conflicting hit is removed from the poorer of the two segments, where the quality is defined, as above, by the maximum number of hits and the minimum χ^2. The segments are allowed to share non conflicting hits up to a configurable number: the default is just two. If more are present, the worst candidate is rejected.

The hits from the leftover candidates are updated (this is the "second step" mentioned in Section 4.2.2), taking into account the incidence angle as reconstructed by the segment. The segment linear fit is then recomputed using the updated hits.

Matching of the two projections. Up to this point, the r-ϕ and r-z projections are treated independently. As the two projections are orthogonal, a segment in one projection cannot be used to validate or invalidate a segment in the other: all combinations of segments from the two projections are kept.

The knowledge of the position along the wire is provided to the hit reconstruction algorithm which updates the hit positions in the cells before performing the final fit of the segment. The result is a segment with parameters in space, suitable for use in the global reconstruction.

4.3.1 Performance of the Segment Reconstruction

The three-dimensional segments built combining the r-ϕ and r-z measurement projection, are the the basic ingredients for the track fit. Figure 4.8 shows

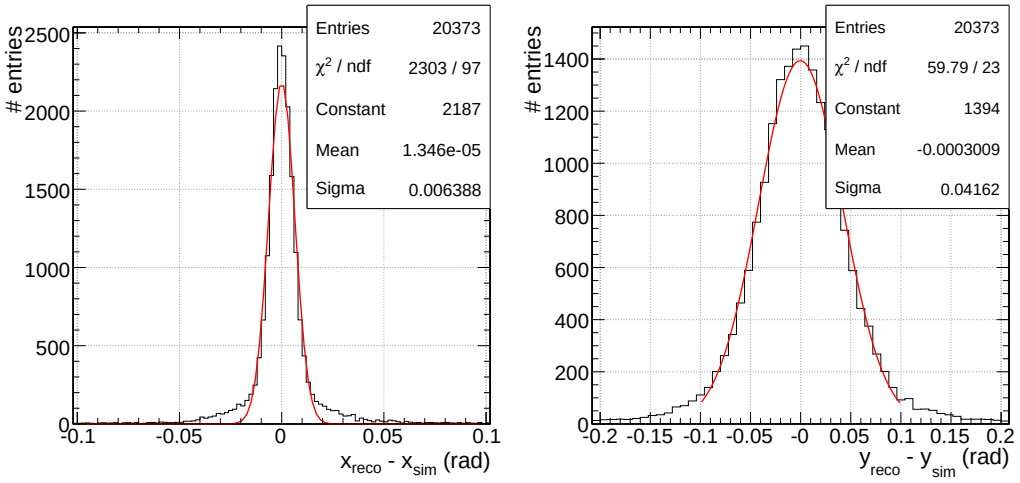

Figure 4.8: *Residuals on the x (left) and y (right) coordinates of three-dimensional segments reconstructed with the drift-time parametrization. The plots are obtained comparing the simulated and reconstructed track positions in the chamber reference frame.*

the residuals on the measured coordinates x (left) and y (right) which are the components measured by r-ϕ and r-z superlayers respectively. Starting from an uncertainty of about 170 μm (cf. Section 4.2.3) on the position of the one-dimensional hits within the cell it is possible to achieve a resolution of 64 μm in the bending coordinate. The wider distribution for the measurement of r-z superlayers is actually, just an effect of the choice of the reference frames (cf. Section 2.4.1.1). In fact, since the position of a three dimensional segment is defined on the surface passing from the center of the chamber, the measurement of the r-z superlayer must be extrapolated to that plane. The distribution in the right plot of Fig. 4.8 is therefore the convolution of the uncertainties on the segment position and direction. This suggests that improved resolution on the θ angle of the muon track can be achieved using the segments in the separate views for the track fit. However, even if the two-dimensional segments are used in the track reconstruction, the three-dimensional segments are useful for the pattern recognition and the refinement of the computation of the hit position. The plot in Fig. 4.9 shows the actual accuracy on the measurement of r-z superlayers: the residual distribution is computed considering the position of two-dimensional r-z segments in the superlayer reference frame. In this case, the sigma of the Gaussian fit performed to the central part of the peak is around

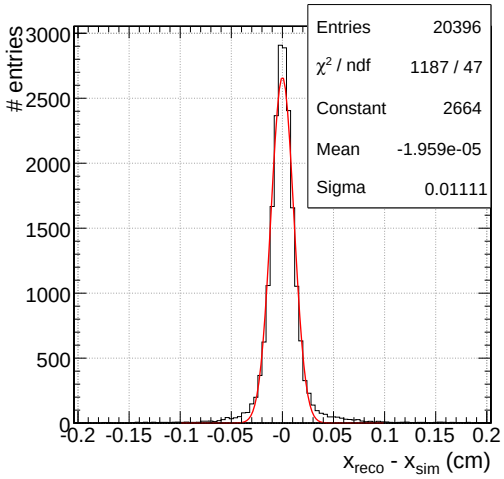

Figure 4.9: *Residuals on the position of r-z two-dimensional segments in the superlayer reference frame.*

110 μm. Note that this value is still poorer than the one for the other projection: this is due to the fact that, in this view, only four layers instead of eight are available.

As far as the direction of the reconstructed segments is concerned, the plots in Fig. 4.10 show the resolution on the two measured angles. A very good resolution, around 0.5 mrad, is achieved in the r-ϕ projection. The large non-Gaussian tails of the distribution are mainly due to the presence of hard secondary hits which, crossing different layers, can affect the pattern recognition. The resolution on the angle measured by r-z superlayers is around 5 mrad. The difference between the two projections is mainly due to the longer lever arm available for the two r-ϕ superlayers.

Also in this case the pattern recognition executed using eight measurement layers represent a clear advantage. This is illustrated in the plots in Figures 4.11 and 4.12. The histogram on the left of Fig. 4.11 shows the distribution of the reconstructed angle measured in the r-ϕ projection while the plot on the right shows the reconstructed angle versus the simulated one. These distributions are referred to three-dimensional segments: therefore the pattern recognition in the r-ϕ view is performed on eight layers. The two plots in Fig. 4.12 show the same distributions obtained, in this case, considering only one r-ϕ superlayer at the time. In this case large angles are reconstructed giving tails well beyond 0.5 rad. As shown in Fig. 4.13, this effect is suppressed in the r-z view, which is the non-bending coordinate, because of the stringent cut applied to the segment angle requiring only segments pointing toward the nominal interaction point. In this projection the range of angles can go up to 1.1 rad. The asymmetry in the distribution is due to the choice of the chamber reference frame, which has

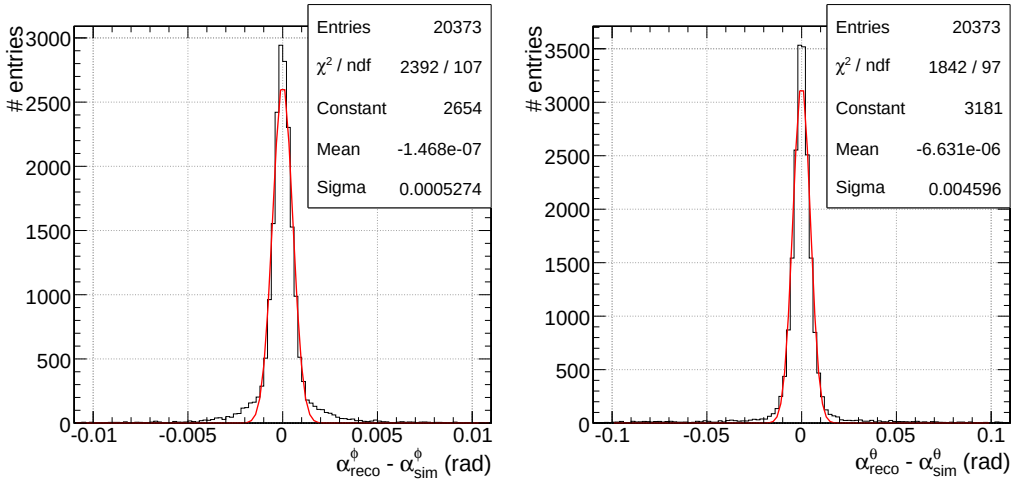

Figure 4.10: *Distribution of the residuals on the angles measured by three-dimensional segments. The plot on the left refers to the angle measured by r-ϕ superlayers while the plot on the right is referred to the r-z projection. The residuals are computed comparing reconstructed and simulated quantities.*

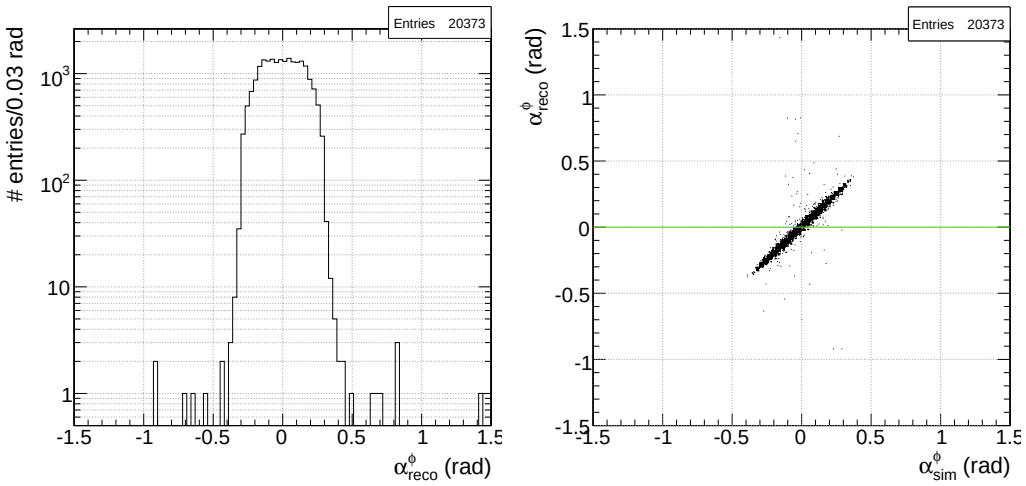

Figure 4.11: *Distribution of the angle measured by three-dimensional segments in the r-ϕ projection. The plot on the right shows the reconstructed angle versus the simulated one.*

the y-axis always pointing outward with respect to the CMS center.

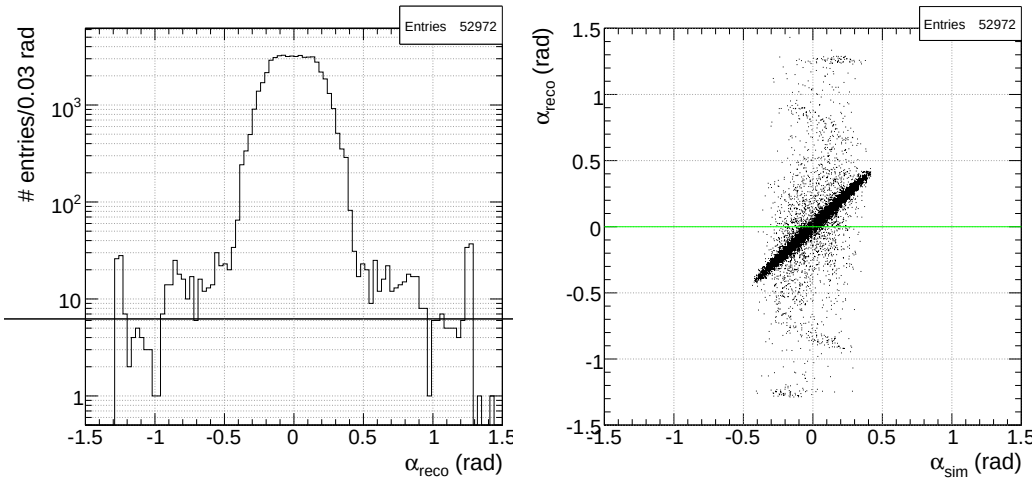

Figure 4.12: *Distribution of the angle measured by two-dimensional segments reconstructed in r-ϕ superlayers exploiting only 4 layers for the pattern recognition. The plot on the right shows the reconstructed angle versus the simulated one.*

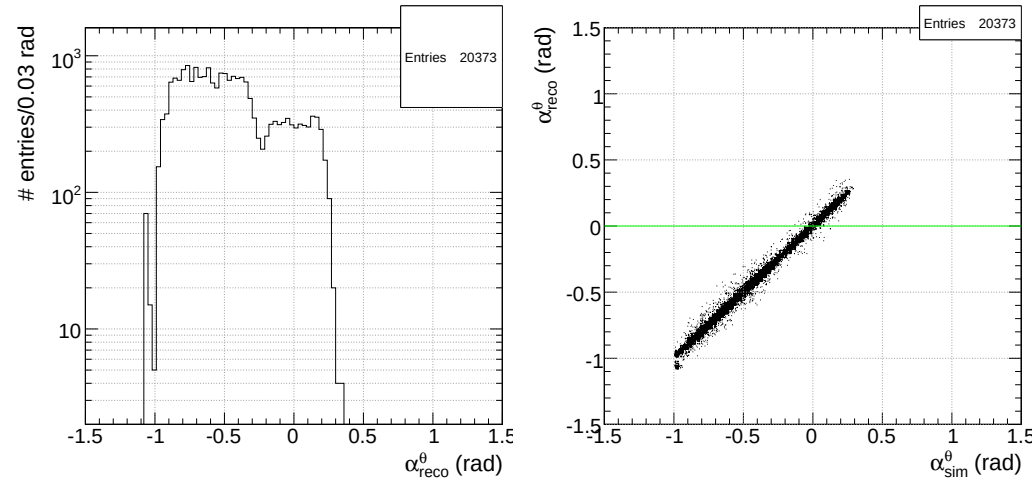

Figure 4.13: *Distribution of the angle measured by three-dimensional segments in the r-z projection. The plot on the right shows the reconstructed angle versus the simulated one.*

4.4 Conclusions

The development of the local reconstruction algorithms for the DT chambers and the study of their performance on real and simulated data has been one of my tasks within the Muon Physics Reconstruction and Selection Group of the CMS experiment.

The segment reconstructed in the DT stations are the basic input to the muon track fit in the barrel spectrometer both in the offline and in the High Level Trigger reconstruction. The performance of the reconstruction must therefore meet the reliability and robustness requirements needed by such task, providing good resolution on the position and the direction and reduced processing time also in high multiplicity environment.

Concerning the resolution, an important improvement came from the usage of the GARFIELD parametrization in the reconstruction of cell hits. The modeling of the cell non-linearities and of the average drift velocity allows more precise reconstruction, especially in the most critical regions, with respect to the constant drift velocity. This has been also tested on real test-beam data, as it will be described in Section 6.3.2.

However, the parametrization of the cell is still open to further improvements. In fact, the parametrization currently used was not designed for the reconstruction: a more detailed treatment would require a dedicated GARFIELD simulation. In particular the simulation should be used to build the distribution of the distances corresponding to a certain drift time, extracting from that a parametrization of the average drift-distance and of the width of the distribution which would allow to parametrize also the error associated to the reconstructed hit.

As far as the segment building is concerned, the problem of high occupancy in presence of muon showering should be addressed with a dedicated reconstruction not based on the current combinatorial pattern recognition. A possible solution which is under study is a clustering algorithm of the hits in the chamber; this would allow to skip the segment building when the hit multiplicity is too high.

It is worth noticing that the local reconstruction procedure has been designed for p-p events, namely for bunched muons from the interaction point. However, since October 2005 the reconstruction has been extensively used also for cosmic events acquired during the chamber commissioning and the Cosmic Challenge both in the offline analysis of the data for the certification of the chamber functionality and in the on-line monitoring of the data quality. Further optimization would be required to improve the performance of the segment building with this kind of events: when the vertex constraint is removed to reconstruct non-pointing muons other methods should be developed to limit the number of segment candidates.

The tests of the reconstruction on real data have been an extremely useful benchmark for the whole reconstruction chain, leading also to many improvements in its design. This experience suggested a design capable to guarantee to the end user the needed flexibility to treat data acquired in different running conditions: cosmics, test-beam and simulated p-p data require completely dif-

ferent treatment of calibration, synchronization constants and custom tuning of the algorithms.

Chapter 5

Calibration of the DT Local Reconstruction

As already discussed in the previous chapter, the input to the local reconstruction in the DT detectors are TDC measurements stored in the "digi" objects. The interesting information contained in the digi-times is the drift-time of the electrons in the cell but this is not the only contribution to the measurement. The first goal of the calibration procedure is therefore to determine the time pedestal needed to extract the drift-time associated to each digi.

Once the drift-time is determined the reconstruction can be performed using one of the two algorithms described in Section 4.2: a constant drift velocity over the entire cell or the GARFIELD parametrization.

The latter, by design, does not require any calibration procedure; it relies on the fact that the dependence of the drift times on the stray magnetic field and on the impact angle has been parameterized. Small variations in the electrostatic field and in the gas conditions with respect to those used in the GARFIELD simulation have a little effect as the cell is operated in regime of saturated drift velocity.

The algorithm using a constant drift velocity instead requires an accurate calibration to take into account the dependence of the effective drift velocity on the track impact angle and the residual magnetic field in the gas volume. Therefore the calibration procedure must determine the best average drift-velocity with a granularity suited to take into account local variations of such parameters.

Since the pattern recognition and the segment reconstruction are based on linear fits and quality selection exploiting the χ^2, the error assignment plays a key role. For this reason, the calibration algorithm must also be able to assign a correct uncertainty to the reconstructed hits.

The procedures for the determination of the time pedestals are described in Section 5.1 while Section 5.2 introduces the calibration of the drift velocity and

describes the algorithm based on the computation of the meantimers.

5.1 Calibration of the Time Pedestals

As already discussed in Section 3.2.2.3, the TDC measurement contains several contributions other than the drift time:

- propagation time of the signal along the anode wire;
- delays due to the cable length and read-out electronics;
- delays due to the Level-1 trigger latency;
- time-of-flight of the muon from the interaction point to the cell.

The goal of the calibration of the time pedestals is to determine the average value of these contributions needed to estimate the drift-time. This delay is usually referred as t_{trig} because of its dependence on the trigger latency.

The inter-channel synchronization can be obtained with a special hardware procedure described in Section 5.1.1. This procedure allows to compute only the relative offset among different wires, called t_0, due to different cable length and delays in the read-out electronics circuits. The absolute pedestal is accounted by the t_{trig} which is estimated from the distribution of the digi-times superlayer by superlayer. The calibration of the t_{trig} pedestal is described in Section 5.1.2.

Note that the determination of these two delays does not solve completely the problem of the synchronization of the digi times: the t_{trig} offset only accounts for the average time-of-flight and for the average delay for the signal propagation along the wire. Further corrections for these quantities are applied on an event by event basis during the reconstruction procedure, as already described in Section 4.1, and they can be as high as ~ 2 ns for the TOF and ~ 6 ns for the signal propagation delay.

5.1.1 Determination of the Relative Offsets Among Different Channels

The computation of the relative offset among different channels is needed since each wire has a different signal path length to the readout electronics. In the data, the determination of this t_0 is performed through special calibration runs: a test-pulse is generated at the input of the front-end chip for 4 wires at once, simulating a muon track crossing a superlayer. These simultaneous signals generate a Level-1 trigger which starts the local readout. The sequence is then repeated scanning all the channels of the chamber.

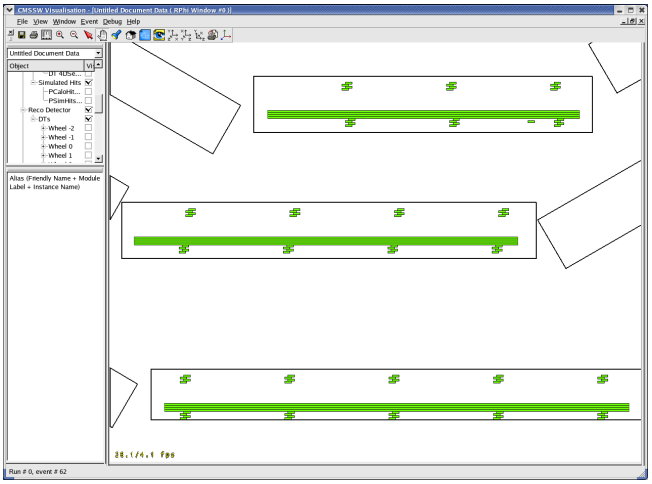

Figure 5.1: *Event display of a test-pulse run acquired during the Magnet Test and Cosmic Challenge data taking. The green boxes represent the test pulse signals on each wire. The picture is obtained with the* IGUANA *visualization package [35, 36].*

The resulting distribution of the measured times is extremely narrow, with a width of 1 or 2 TDC counts [1]. The average time value of each channel is stored in a database to be used later during the reconstruction. Note that the only relevant information contained in these delays is the relative difference among different channels since the absolute offset is just determined by the particular latency of the trigger used to read out the test-pulses.

Such dedicated calibration runs will be taken before the beam injection in the LHC and allow to scan all the DT channels in a short time working on all chambers in parallel. Figure 5.1 shows the event display of a test-pulse run acquired during the Magnet Test and Cosmic Challenge data taking. These data will also provide a verification of the status of the entire electronic chain.

The inter-channel calibration performed subtracting the t_0 from pulses to the digi-times allows to compute the absolute offset of the drift-time distribution for a superlayer at a time.

5.1.2 Determination of the Drift-Time Pedestals

Since the digi times of the different channels have already been synchronized among each other subtracting the t_0 offset, the t_{trig} can be computed with every possible granularity within the chamber. The usual choice is to compute it superlayer by superlayer, balancing the accuracy in accounting for the average TOF with the need of statistics.

[1] For the HPTDC chip used in the DT electronics 1 TDC count = 0.7812 ns.

Due to its dependency on the trigger latency the t_{trig} pedestal must be calibrated each time the trigger configuration and synchronization are changed. Moreover, as it accounts for the average contribution of the time-of-flight and signal propagation along the anode wire the t_{trig} also depends on the running conditions: these contributions will be different if the superlayer is not illuminated uniformly as for example in test-beam data taking. This has to be taken into account when using the pedestals in the reconstruction (cf. Section 4.1.1).

The pedestal can be estimated directly from the distribution of the digi-times. It is therefore necessary to find a feature of this distribution which can be identified in unambiguous and automatic way. Earlier studies have shown that such suitable feature is the derivative of the time-box peak since it can be approximated with a Gaussian [37]. This method is not robust against noise and spikes due to the read-out electronics. Since an automatic procedure must be implemented in order to run the fit of the drift-time box in unattended mode for all the superlayers of the 250 DT chambers we developed an alternative more robust procedure. This method estimates the pedestal fitting the rising edge of the drift-time distribution with the integral of a Gaussian function:

$$f(t) = \frac{1}{2} I \left[1 + \mathrm{erf}\left(\frac{t - \langle t \rangle}{\sigma\sqrt{2}} \right) \right]. \tag{5.1}$$

An example of such fit is shown in Fig. 5.2 for the time distribution of a superlayer r-z of a chamber exposed to a muon test beam.

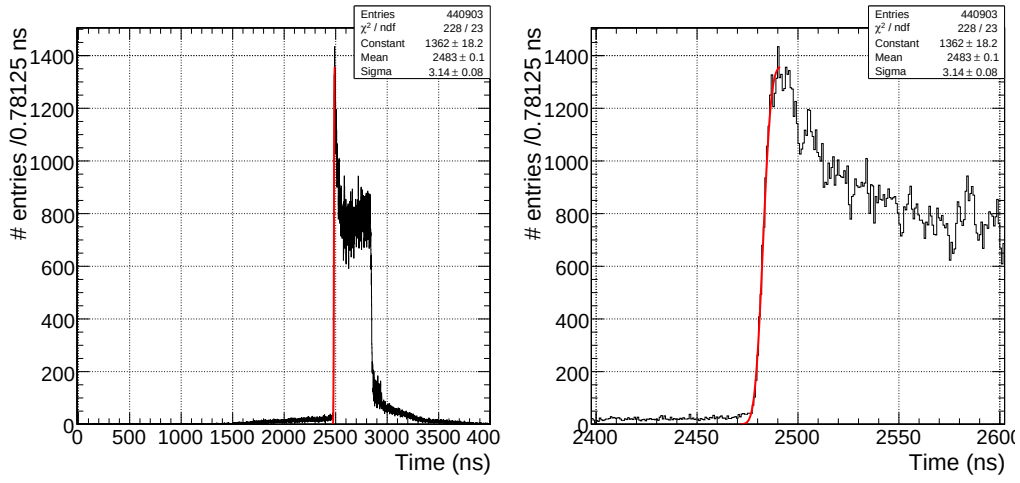

Figure 5.2: *Distribution of the digi times of one superlayer acquired during the test-beam 2004. The rising edge of the time box (right) is fitted with the integral of a Gaussian to measure the time pedestal of the drift times (t_{trig}).*

This fit allows to estimate the mean of the Gaussian which is located in the middle of the rising edge of the drift-time distribution while the optimal value

of the t_{trig} pedestal must determine the beginning of the rising edge. This is computed using the sigma of the Gaussian through the relation:

$$t_{trig} = \langle t \rangle - k \cdot \sigma; \tag{5.2}$$

where k is a factor used to tune the delay: the fine tuning of the t_{trig} is performed superlayer by superlayer, requiring the minimization of the residuals on the reconstructed hit position.

Note that the value of t_{trig} depends on the algorithm used in the reconstruction. For example, the GARFIELD simulation can have a small intrinsic offset deriving from the way the signal arrival time is computed (cf. Section 3.2.2.1). A fine tuning of the t_{trig} has to be done differently when the reconstruction is performed using the parametrization.

Also the effect of a mis-calibration of the time pedestal is different for the two reconstruction algorithms.

If the reconstruction is performed using a constant drift velocity over the entire cell, a t_{trig} not perfectly calibrated results in an error on the estimated drift time and therefore in a constant offset for all the reconstructed distances from the wire.

This is illustrated in Fig. 5.3 which shows the residuals on the distance from the wire for two particular choices of the time pedestal: the "optimal" value and a t_{trig} mis-calibrated of $\Delta t = 6$ ns [2]. The error on the pedestal affects the mean value of the distribution of a quantity which is given by $-\Delta t \cdot v_{drift}$ while the sigma of the Gaussian fit is not modified.

This property is used for the optimization of the t_{trig} value superlayer by superlayer: the k factor of eq. 5.2 is used to tune the pedestal in order to minimize the mean of the residual distribution.

The calibration of the t_{trig} is more critical when the reconstruction is performed using the GARFIELD parametrization. In this case the effect of a mis-calibration of the pedestal is more complex than for the constant drift-velocity. In fact, an offset in the t_{trig} pedestal not only introduces an offset in the mean value of the residuals but also implies that the non-linearities as a function of the drift time are not correctly accounted.

This is illustrated in Fig. 5.4 which shows again the residuals on the reconstructed distances from the wire for two extreme choices of the t_{trig} pedestal. The scatter plot of the residuals shows that the mis-calibration introduces further artificial non-linearities in the reconstruction. This results in a wider residuals distribution. As a consequence, in this case, the optimization of the t_{trig} value is performed minimizing the sigma of the Gaussian fit of the residuals.

[2] This value of the pedestal corresponds to an extreme case of mis-calibration and it has just be chosen for illustration purpose since the t_{trig} can be usually calibrated with much higher accuracy.

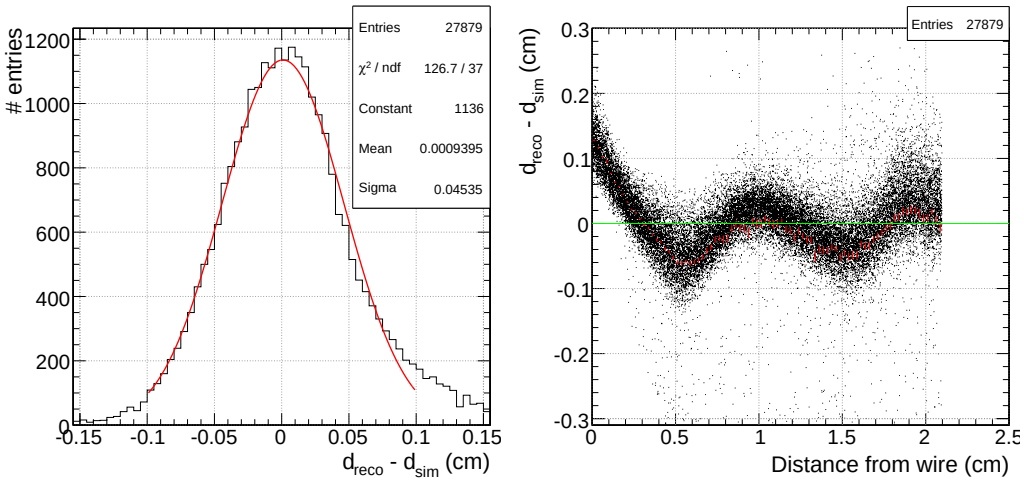

(a) Optimal time pedestal t_{trig} (MC truth)

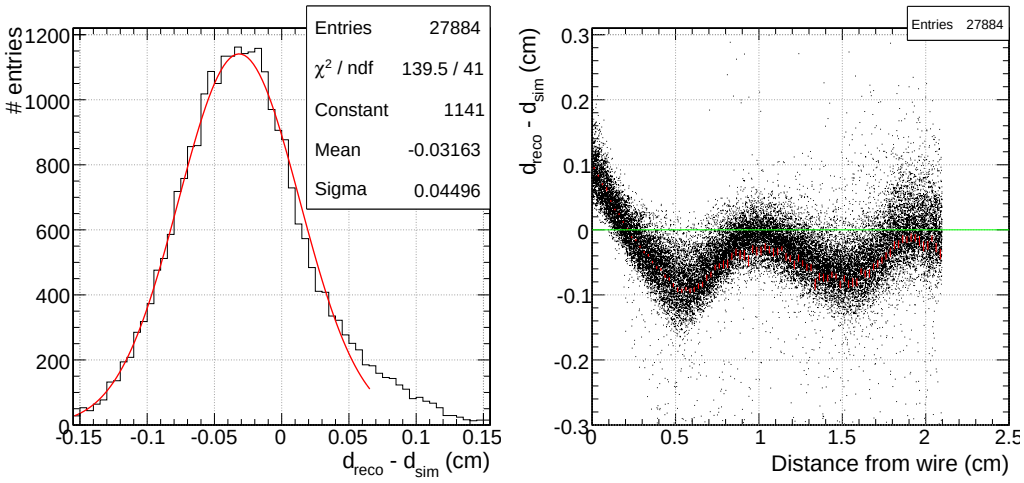

(b) Mis-calibrated time pedestal (t_{trig}+ 6 ns)

Figure 5.3: *Residuals between the reconstructed and the simulated hit distances from the wire for r-z superlayers in wheels ±2. The plots on the right show the residuals as a function of the distance from the wire. The plots have been obtained using a constant drift velocity (first reconstruction step) with the optimal value of the t_{trig} (a) and with a t_{trig} 6 ns bigger than the optimal one (b).*

5.2 Calibration of the Drift Velocity

As already discussed in Section 3.1 the drift velocity depends on many parameters such as the gas purity and conditions and the electrostatic configuration of the cell. Moreover, the bending induced by the magnetic field and the effect of the track angle can have an influence on the effective drift velocity modifying

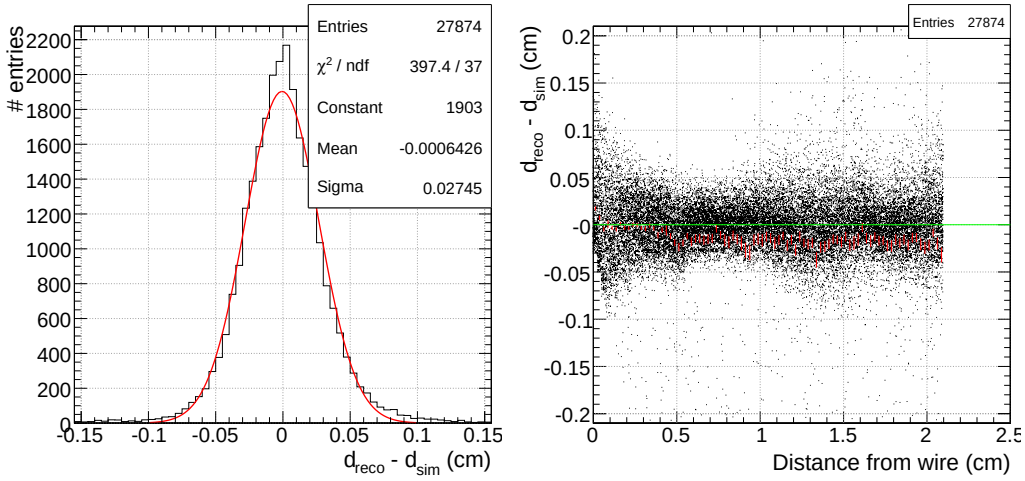

(a) Optimal time pedestal t_{trig} (MC truth)

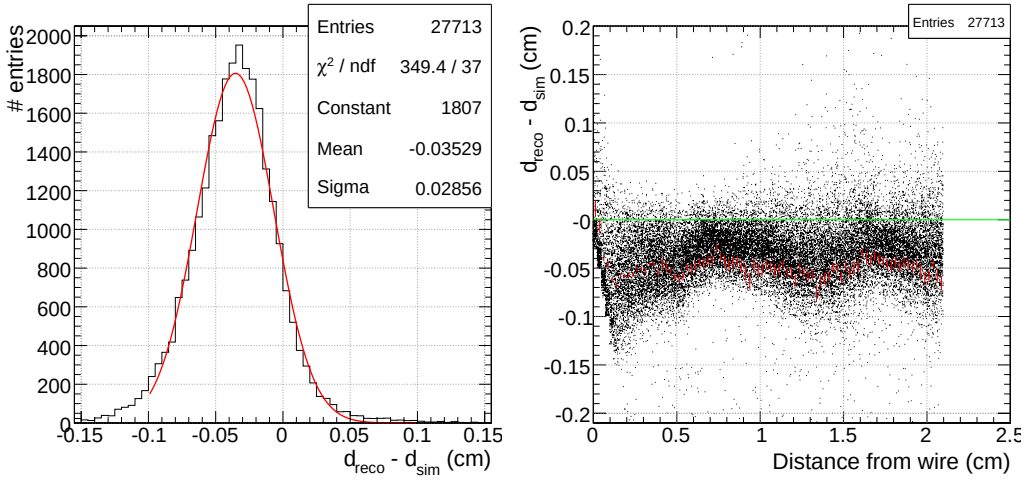

(b) Mis-calibrated time pedestal (t_{trig}+ 6 ns)

Figure 5.4: *Residuals between the reconstructed and the simulated hit distances from the wire for r-z superlayers in wheels ±2. The plots on the right show the residuals as a function of the distance from the wire. The plots have been obtained using the* GARFIELD *parametrization (first reconstruction step) with the optimal value of the t_{trig} (a) and with a t_{trig} 6 ns bigger than the optimal one (b).*

the drift path of the ionization electrons.

The working conditions of the chambers will be continuously monitored and important variations are not expected among different regions of the spectrometer. The situation is different for the stray magnetic field and for the impact angle: such external parameters will substantially vary moving from chamber

to chamber and also from superlayer to superlayer due to the different position within the return yoke and to the different pseudorapidity for the impact angle in r-z cells.

For this reason, the reconstruction algorithm using a constant drift velocity requires a calibration procedure which allows to find the average velocity for different groups of cells.

To match these requirements a calibration algorithm based on the so called *meantimer* computation has been developed and it is described in the following. This technique allows to estimate the maximum drift time and therefore the average drift velocity in the cell. Moreover, it also allows to measure the cell resolution, which can be used as an estimate of the uncertainties associated to each measurement.

Meantimer computation. The meantimer formulas are relations among the drift times produced by a track in the different layers of a superlayer and the maximum drift time in the semi-cell.

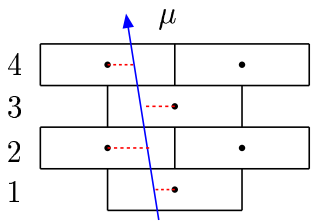

Figure 5.5: *Sketch representation of a muon crossing a semi-column of cells.*

The mathematical expression of the meantimer relation depends on the track angle and on the pattern of cells hit by the track. The most trivial relation is the one for a track crossing a semi-column of cells (see Fig. 5.5): from simple geometric considerations it descends that the drift-times in three consecutive layers (t_1, t_2, t_3) are related by:

$$T_{max}^{123} = \frac{t_1 + t_3}{2} + t_2; \tag{5.3}$$

where T_{max}^{123} represents the maximum drift time in the semi-cell. Note that this is true only if no delta-rays are produced: the signal generated by the secondary would mask the one produced by the muon resulting in a shorter drift-time and therefore in a smaller T_{max}^{123}.

The meantimer relations for different track angles and patterns of hit cells are listed in Appendix A. The possibility of computing the T_{max} for various configuration of fired channels is extremely important for the calibration task which

must take into account the dependence of the drift-velocity on the track angle. The adequate meantimer formula is chosen among those listed in Table A.1 track by track using the information on the direction and position provided by the three-dimensional segments. This implies an iterative calibration procedure starting with values of the drift-velocity and of the t_{trig} which already allow an efficient pattern recognition and segment reconstruction.

Calibration procedure. The calibration procedure consists of the following steps:

- a fit with a Gaussian of the meantimer distributions for each pattern j to estimate the mean value T^j_{max} and the sigma σ^j_T and the error on the mean $\sigma^j_T/\sqrt{N_j}$ (where N_j is the number of entries in the distribution). The T^j_{max} contains the information about the average drift-velocity in the different regions of the cell, since it is computed using drift-times produced by hits in all the gas volume;

- the weighted average of the T^j_{max} is computed where the weights are taken as $(\sigma^j_T)^2/N_j$:

$$\langle T_{max} \rangle = \frac{\sum_j \frac{T^j_{max}}{(\sigma^j_T)^2} N_j}{\sum_j \frac{N_j}{(\sigma^j_T)^2}}. \tag{5.4}$$

  This allows to account for the relative importance of the different cell patterns in the computation of the maximum drift time.

  The meantimer is normally computed superlayer by superlayer. It may be however interesting to calibrate the average drift velocity with finer granularity to take into account possible local variations within the layer quadruplet due to magnetic field inhomogeneities;

- once the $\langle T_{max} \rangle$ is computed it is straightforward to find the average drift velocity through the relation:

$$v_{drift} = \frac{L/2}{\langle T_{max} \rangle}; \tag{5.5}$$

  where L is the width of the cell. The drift-velocity computed for each superlayer is then stored in a database and it can be used both by the HLT and the off-line hit reconstruction.

Estimate of the cell resolution from the meantimer distribution. The meantimer technique is particularly suited for the calibration of the reconstruction algorithm since it also allows to estimate the cell resolution, and therefore

the uncertainties on the reconstructed distance, which is crucial as the pattern recognition and segment building are based on quality cuts relying on the χ^2 of the fit.

The sigma of the meantimer distributions (σ_T^j) are a measurement of the resolution on the T_{max}^j. They can be therefore used to estimate the uncertainty on the measurement of the drift-times (σ_t^j) with a relation which depends on the particular formula used to compute the meantimer. In case of tracks crossing a semi-column of cells, given the meantimer relation in eq. 5.3, the time resolution can be computed as:

$$\sigma_t^j = \sqrt{\frac{2}{3}} \cdot \sigma_T^j \tag{5.6}$$

which is valid under the assumption that the uncertainties are the same for the three layers used in the meantimer computation.

Since the cell resolution depends on the track angle, an average effective value is computed averaging the different values obtained for the contributing cell patterns weighted on the number of entries in each meantimer histogram (N_j):

$$\langle \sigma_t \rangle = \frac{\sum_j \sigma_t^j \cdot N_j}{\sum_j N_j}. \tag{5.7}$$

The resolution on the reconstructed distance is therefore given by:

$$\sigma_d = v_{drift} \cdot \langle \sigma_t \rangle. \tag{5.8}$$

This is the value used during the reconstruction to assign the uncertainties to the one-dimensional RecHits in the gas volume.

5.2.1 Meantimer Computation and Time Pedestals

The reconstruction using a constant drift velocity requires both the calibration of the time pedestals needed for the synchronization and of the average drift velocity. These two tasks are not independent since the computation of the meantimer requires the knowledge of the time pedestals and, vice-versa, the fine tuning of the t_{trig} is based on the analysis of the residuals which are directly affected by a mis-calibration of the drift velocity.

If the determination of the t_{trig} is affected by a systematic shift Δt:

$$t'_{trig} = t_{trig} + \Delta t; \tag{5.9}$$

the meantimer will be consequently biased of a quantity which depends on the particular formula among those in Table A.1. In case of tracks crossing a semi-column, from eq. 5.3 we can evaluate the effect on the T_{max} as:

$$T'_{max} = T_{max} - 2\Delta t. \tag{5.10}$$

In a simplified scenario where this particular pattern is the one determining the meantimer calculation ($\langle T_{max} \rangle \sim T'_{max}$) the bias on the t_{trig} determination will result in a mis-calibration of the drift-velocity Δv_{drift} which can be estimated as:

$$\begin{aligned} v_{drift} + \Delta v_{drift} &= \frac{L}{2 \cdot T'_{max}} \\ &= \frac{L}{2 \cdot (T_{max} - 2\Delta t)}. \end{aligned} \tag{5.11}$$

At first order this is equivalent to require:

$$2 v_{drift} \Delta t - T_{max} \Delta v_{drift} = 0 \tag{5.12}$$

which can be considered as a calibration condition [38]: all the values of drift velocity and time pedestal satisfying this relation will not affect the mean value of the residuals. This is strictly true only for small variations around the "optimal" values of t_{trig} and v_{drift} since larger fluctuations may affect the pattern recognition efficiency and the segment building reliability: without external system for the track measurement the segment is used as reference for the computation of the residuals on the reconstructed drift distance.

The main sources of uncertainty in the determination of the time pedestal are due to fluctuations in the mean value $\langle t \rangle$ and in the sigma σ of the fit in the different layers of the superlayer; the intrinsic statistical error, the presence of noise before the drift-time box, the finite step size of the TDC (0.78 ns) and the fact that the distribution is not perfectly described by eq. 5.1, put a limit on the accuracy of the t_{trig} determination of about 1 ns. Further systematic uncertainties come from the uncertainty on the drift velocity, as demonstrated by eq. 5.12, therefore higher accuracy can only be achieved using a procedure for the fine tuning of the time pedestal independent on the drift-velocity.

An alternative approach consists in the usage of the different dependence on a t_{trig} mis-calibration of the various meantimer formula listed in Table A.1 to calibrate the pedestal. The difference between the T_{max} computed using different formulas can be used to measure the value of the mis-calibration Δt once the dependence of the meantimer on the track impact angle is well under control. This would allow to tune the t_{trig} without relying on the residual distribution and therefore without convolving the error on the calibration of the drift-velocity.

5.3 Conclusions

The calibration task is fundamental for the performance of the local reconstruction: the knowledge of the time pedestal is a prerequisite for the computation of

the drift distance, while the calibration of the average drift velocity determines the accuracy of the reconstruction.

For this reason a great effort has been put in the development of a robust calibration procedure which satisfies the requirements imposed by the different running conditions and the user necessities: the treatment of cosmics, test-beam and p-p-collision data requires the full control over the computation and the handling of the calibration and synchronization constants.

The calibration algorithms described in present chapter have been tested both on the simulation and on real data acquired during the commissioning and the 2004 test-beam (cf. Chapter 6). The results are satisfactory allowing a reliable and precise reconstruction.

The tools developed for the calibration and synchronization procedure also allowed to study the effect of possible mis-calibration of the pedestals and of the drift-velocity on the muon track fit and, eventually, on higher level reconstructed quantities. This has been applied for the study of the systematic uncertainties in the study of the physics reach of the experiment documented in the Volume II of the Physics Technical Design Report [2].

Further optimization is however possible. In particular, the accuracy of the current procedure is limited by the interdependence of the time pedestal and the drift velocity used in the reconstruction. Other methods for the fine tuning of the t_{trig} are under study; the procedure based on the usage of different meantimer formulas to estimate the best value of the time pedestal is the most promising.

Chapter 6

Analysis of DT Test-Beam Data

In October 2004 two Drift Tube chambers were tested on a 40 MHz bunched muon beam at the SpS facility at CERN. The primary goal of this data taking was the test of the final on-chamber electronics of read-out and Level-1 trigger [39, 40]. The data collected during the test also are an important sample for the validation of the simulation and digitization chain and for the study of the performance of the local reconstruction and calibration [41]. In particular, the time structure similar to that foreseen for LHC events makes these data particularly suited for this task. All following tests have been performed with cosmic muons without external trigger sources; cosmic rays, due to their flat arrival time distribution, can not be used for a detailed study of the chamber resolution, as the local trigger is designed for bunched data taking.

This validation task is very important to understand the simulation of physics processes involving muons in the final state. The comparison with real data allows to test the reliability of each step of the simulation. In particular it is possible to study the accuracy of the modeling of the interaction of particles with the detector material, the agreement of the parametrization of the cell response with the real data and the impact of the assumptions used in the simulation.

In the present chapter, after a brief introduction to the setup used for the data taking, the comparison of simulated and real events is presented in Section 6.2. A similar comparison for the results of the reconstruction is presented in Section 6.3.

Finally, the data collected during the test beam have also been used to compare the performance of the two reconstruction algorithms available for the hit reconstruction in the cell volume: the resolution achieved with a constant drift velocity and with the GARFIELD parametrization of the cell are presented in Section 6.3.2.

6.1 Test-Beam Setup

The experimental setup of the test-beam 2004 consisted of two DT chambers, belonging one to the first (MB1) and one to the third (MB3) barrel stations, exposed to a muon beam in the H2 zone of the CERN SpS North Area.

A time structure similar to that foreseen for the LHC operation was chosen for the SpS proton beam, with bunches of about 2 ns with 40 MHz frequency. Trains of 48 bunches occurred every 25 μs (each train lasts 48×25 ns $= 1200$ ns) during a spill of 2.2 s length (a so called slow-extraction cycle of the SpS). From the collision of the protons with a primary target a muon beam was extracted selecting the proper particle momentum in a range between 30 GeV/c and 300 GeV/c. This secondary beam had the same time structure of the primary one but the mean occupancy in a bunch was rather low, of the order of 10^{-2} - 10^{-3}, therefore muons were separated in time by several microseconds, on average.

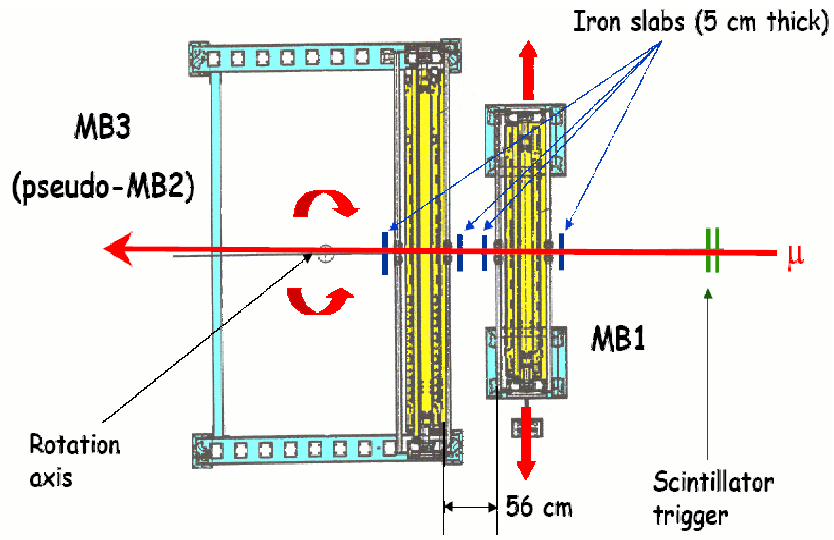

Figure 6.1: *Schematic top view of the setup used for the data taking of test-beam 2004.*

The picture in Fig. 6.1 shows a schematic top view of the chamber setup. The first chamber encountered by the muon beam was the MB1 type chamber. It was placed on a support which allowed lateral displacements in the direction perpendicular to the beam and parallel to the floor. Also the support of the MB3 chamber could be moved: it was in fact possible to rotate the chamber with respect to a vertical axis and to horizontally translate it in all possible directions. Both chambers were placed with the wires of r-ϕsuperlayers in the

vertical direction, with the front-end electronics at the bottom. With this setup it was possible to study the chamber behavior for various impact angles of the muon beam, emulating the bending of the muon tracks in the CMS magnetic field. In order to consider the effect of the material of the CMS yoke it was possible to insert on the beam trajectory four iron slabs of 5 cm thickness ($\sim 2.8X_0$), in front and after each chamber.

Figure 6.2: *The setup used in the test-beam 2004. From left to right, it is possible to distinguish the beam trigger scintillators, the MB1 and the MB3 chambers. The muon beam was entering in the experimental hall from the concrete wall behind the scintillators.*

The chambers were flushed with the Ar/CO_2 (85%/15%) gas mixture with a flow of 2 l/min. The concentration of the oxygen in the mixture was continuously monitored by an oxygen monitor, placed downstream on the gas circuit, and it was maintained below 100 ppm during the whole data taking.

The chambers were operated at the nominal high voltages: the potential of the wire, the strips and the cathodes were respectively set to 3600 V, 1800 V and -1200 V. The discrimination threshold of the front-end read-out electronics was set to the minimum value of 15 mV.

Both chambers were equipped with the final on-chamber read-out and trigger electronics (details can be found in [21]). A prototype of the full DT trigger chain [40] was put in place therefore the two chambers could be run in the so called "auto-trigger" mode where two track candidates for each bunch crossing

were delivered as output by the whole system. An external beam trigger was also available through the coincidence of two plastic scintillators defining a 10×10 cm^2 area covering the full muon beam.

The data were collected for different inclination angles, from 0 to 30 degrees of the MB3 chamber with respect to the MB1. Moreover, energy scans between 50 to 300 GeV/c were performed, studying the effect of the material, acquiring data with and without the iron absorbers.

During this data-taking no magnetic field was available; a sample collected with magnetic field would have been particularly suited for the test of the simulation of the chamber response in presence of stray magnetic field and for the test of the reconstruction using the GARFIELD parametrization.

6.1.1 Event Selection

The detailed validation of the simulation and reconstruction chain requires the comparison of the response of the apparatus to muons at different energies and impact angles. For this reason, runs acquired at different beam energies and with different angles of the MB3 chamber with respect to the beam have been considered. The list of the runs used in the following is provided in Table 6.1 together with the main information about the corresponding data-taking conditions.

Table 6.1: *List of the runs used for this study. The beam energy, the angle of the MB3 chamber with respect to the beam and the presence of the iron absorbers are also reported.*

Run #	Muon Energy (GeV)	MB3 Rotation	Iron Absorbers
2575	100	0°	no
2562	100	0°	yes
2597	150	0°	no
2701	150	10°	no
2618	150	20°	no
2699	150	30°	no

To disentangle the effect of the local reconstruction performance from that of the Level-1 local trigger, only data samples collected using the external scintillator trigger have been used or this study.

To be able to compare real data and simulation, we need to select events which contain only a single muon track, since in the simulation the occurrence of double muon events or showering in the concrete wall in front to the chambers is not modeled.

To this purpose, all the results which will be presented in the following are referred to the MB3 chamber selecting a sub-sample of events with only one reconstructed segment in the MB1 chamber. Given the different size of the two chambers it was also necessary to mask the MB3 channels outside the geometric acceptance of the MB1. Except where it is differently specified all the histograms are made with the same number of events (10000) passing this selection for real and simulated data and no additional normalization was required.

This test-beam has been the first data taking with the final on-chamber read-out electronics. With this setup an electronic effect has been observed in the distribution of the time difference between the first and the second hits in a cell shown in in Fig. 6.3. The two narrow peaks around 5 ns and 100 ns

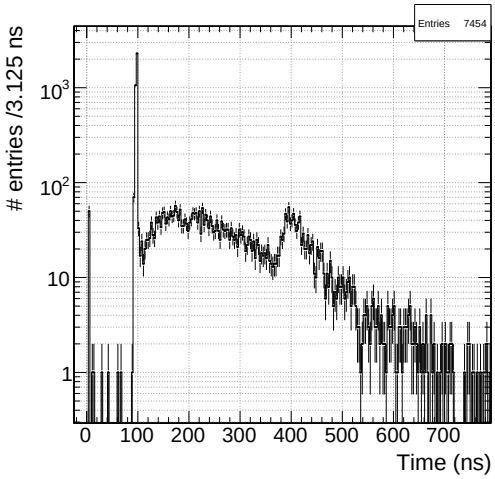

Figure 6.3: *Distribution of the time difference between the second and the first digi in a cell. The peaks at 5 ns and 100 ns are due to signal reflection in the read-out electronics while the peak around 400 ns is due to the production of photo-electrons on the cathode surface.*

were recognized to be the effect of signal reflections in the front-end electronics. Following this observation the TDC dead time has been raised to 120 ns in the following data taking. This effect is therefore not interesting for our study. For this reason a similar dead time of 120 ns was introduced in the off-line analysis of both simulated and real data.

6.1.2 Simulation of the Test-Beam Setup

The detailed validation of the whole simulation and reconstruction chain requires the generation of samples simulating the data taking conditions during the test-beam. The simulation of the chamber response is performed using the official CMS simulation already described in Chapter 3.

GEANT4 requires a detailed description of the geometry and of the materials of the apparatus. In the CMSSW framework this can be done with XML technology. For this study I implemented the various test-beam setups with different angles between the MB1 and the MB3 chambers, with and without the iron absorbers before and after each measurement station. Figure 6.4 shows two of these configurations, visualized using the IGUANA visualization package [35, 36].

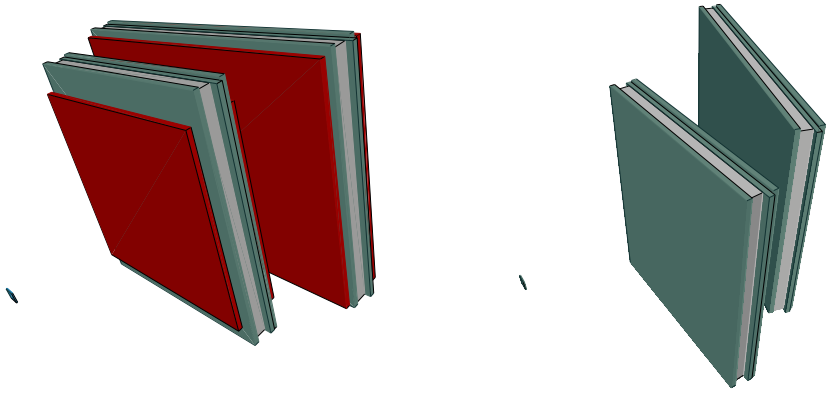

Figure 6.4: *Visualization of two test-beam configurations implemented in the simulation for this study. The picture on the left shows the setup where the MB1 and the MB3 are parallel and the iron slabs (in red) are inserted. In the picture on the right the MB3 chamber is rotated of 20° with respect to the beam. Both pictures have been produced with the* IGUANA *event display package.*

Since the main goal of this study was the test of the simulation and reconstruction chain used in the production of simulated samples, the standard set of cuts and production thresholds has been used for the GEANT4 simulation of the interaction of particles with the detector material.

The digitization process based on the GARFIELD parametrization described in Section 3.2.2, was applied to the simulated hits. To reproduce the resolution observed on real data (cf. Section 6.3) it was necessary to introduce an additional Gaussian smearing ($\sigma = 2.4$ ns) to all the digitized times. In part this smearing can be attributed to the resolution of the scintillator trigger. Contributions can also come from misalignment between the layers which was not considered in this study. Further studies are needed to disentangle this effect from the intrinsic cell resolution.

The TDC dead-time used in the digitization was set to 120 ns to match the one used for the real data, as described in Section 6.1.1.

Different samples, simulating the different running configurations of the test beam, were generated and are listed in Table 6.2.

Table 6.2: *List of simulated samples used for the study.*

Muon Energy (GeV)	MB3 Rotation	Iron Absorbers	Number of Events
100	0°	no	50000
100	0°	yes	50000
150	0°	no	50000
150	10°	no	50000
150	20°	no	50000
150	30°	no	50000

6.2 Validation of the Simulation and Digitization Chain

When comparing the output of the simulation and digitization chain with the data acquired during the test-beam, two major aspects need to be tested in details:

- the simulation of the hit multiplicity in the detector sensitive volumes;
- the modeling of the cell response to crossing particles.

The first is related to the GEANT simulation of the interaction of particles with the detector material and to the way the GARFIELD parametrization handles secondary hits. In fact, as explained in Section 3.3, not all the hits in the sensitive volume can be treated with the parametrization. Moreover, effects not simulated, like noise and after-pulse hits, can contribute to the total number of digis.

The second issue consists in the test of the GARFIELD simulation and parametrization of the drift-cell behavior used to compute the drift-time associated to each hit in the sensitive volume.

Hit multiplicity in the chambers. One of the primary goals of the validation is the comparison of the hit multiplicity in the detector since this has direct impact on the performance of the cell and on the behavior of the pattern recognition.

The number of digis in the event is determined by the contribution of several aspects of the simulation:

- the cuts and production thresholds used in the GEANT simulation;
- the handling of secondary hits in the parametrization;

- effects not considered in the simulation, like noise and after-pulses.

The two plots in Fig. 6.5 show the number of hits per cell for the simulated and real samples for a muon energy of 100 GeV without (left) and with (right) iron absorbers. The number of multiple hits grows when the iron slabs are

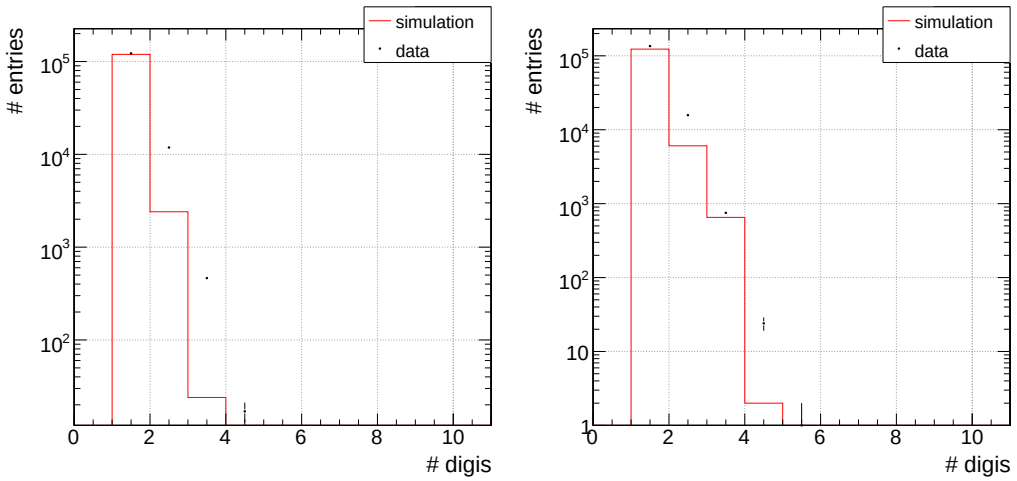

Figure 6.5: *Distributions of the total number of digis per cell for simulated and real data. The plots are referred to a 100 GeV/c muon beam without (left) and with (right) iron absorbers.*

inserted due to the production of secondaries at the iron surface. Although this behavior is also reproduced by the simulation both in the left and right plot the number of hits per cell is slightly underestimated.

To understand the reason of this difference it is useful to observe the plot of the time difference between the first and the second hit in the same cell: this is shown, for the two running conditions, in Fig. 6.6. The shape of the distributions for simulated and real data are different. The peak around 400 ns visible in the real data is due to after-pulse signals: during the avalanche development close to the anode wire photons are emitted; when these photons hit the cathode surface an electron can be knocked out by photo-electric effect. This electron will produce a second signal (the after-pulse) after a time compatible with the maximum drift-time since this is the time needed to drift from the cathode to the anode. Currently, the production of after-pulse electrons is not simulated since its effect on the hit reconstruction is expected to be small. Most of the after-pulse hits will fall outside the time window considered in the reconstruction (cf. Section 4.2) which for this study has been set in order to select digis associated to drift-time between -3 and 400 ns.

Other sources of hits contributing to the multiplicity observed in the data can be identified in the plot of Fig. 6.7 showing the distribution of the digi times

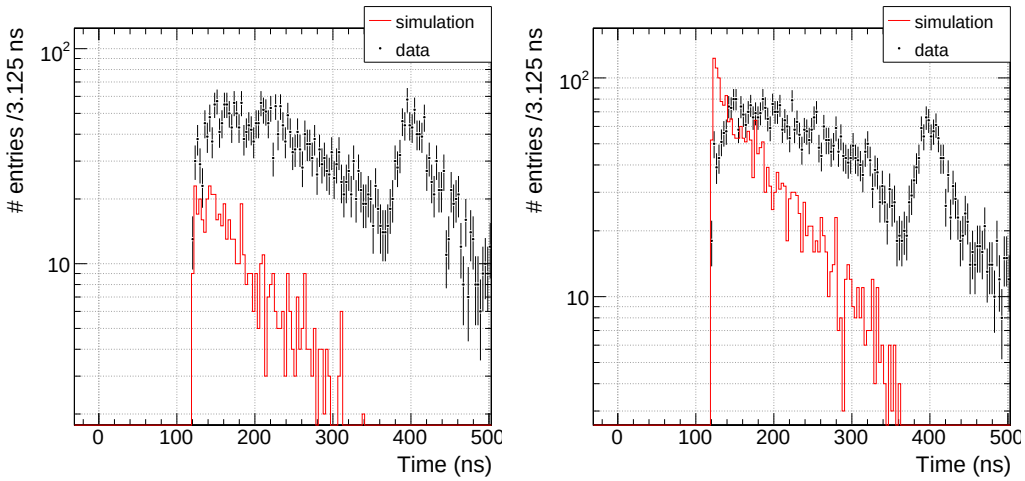

Figure 6.6: *Time difference between the second and the first digi in the cells of a r-ϕ superlayer in the MB3 chamber. The plots are referred to a 100 GeV/c muon beam without (left) and with (right) iron absorbers.*

collected within the superlayer.

The long tails below 1000 ns and above 4000 ns (marked with (a) and (f) in the plot) visible in the data are due to random noise in the tubes. From this plot it is possible to estimate the average noise in the superlayer to be about 20 Hz/wire. This effect is not accounted in the simulation since the noise hits in different layers are uncorrelated and they have a flat distribution in time: their effect is therefore negligible both on the Level-1 trigger and on the performance of the local reconstruction.

The two shoulders of the drift-time distribution (labeled with (b) and (e) respectively) are due to "pile-up" hits produced by muons belonging to different bunches of the spill (cf. Section 6.1) with respect to the trigger one; these hits are still in the TDC buffer when it is read-out. Their effect in the range of times of the signal drift-time distribution (labeled with (c)) is suppressed by the selection of events with only one segment in the MB1 chamber (cf. Section 6.1.1) and its contribution is estimated to give an excess of hits of about 1% in the 403 ns window used for the reconstruction. This contribution is clearly not included in the simulation and this has to be taken into account in the comparison.

All the plots presented up to now include all the measurements collected by the TDC. As already noted only the digis falling in a relatively small time window are used in the reconstruction. From now on we will therefore focus on this population of digis whose drift time falls between -3 and 400 ns.

The multiplicity of these "in-time" digis per cell is shown in Fig. 6.8, again for samples acquired without (left) and with (right) iron slabs.

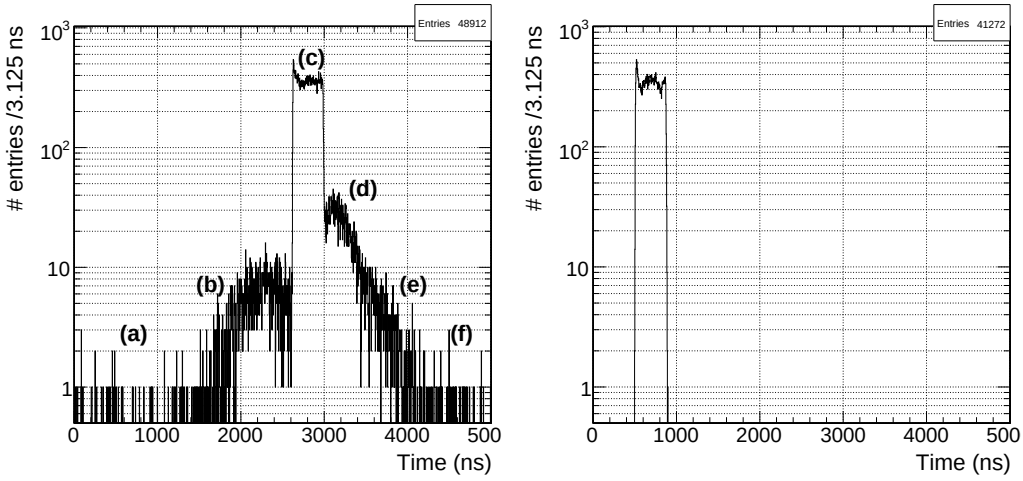

Figure 6.7: *Distribution of digi times for real data (left) and simulation (right). The different contributions to the hit multiplicity in the data are: (a) and (f) random noise tails; (b) and (e) pile-up hits from muons in the other bunches of the train; (d) after-pulses; (c) drift-time distribution for the signal bunch. The simulation does not include all these contributions since only the digis in the 400 ns window used in the reconstruction are simulated. Note that the time pedestal is different for simulation and real data.*

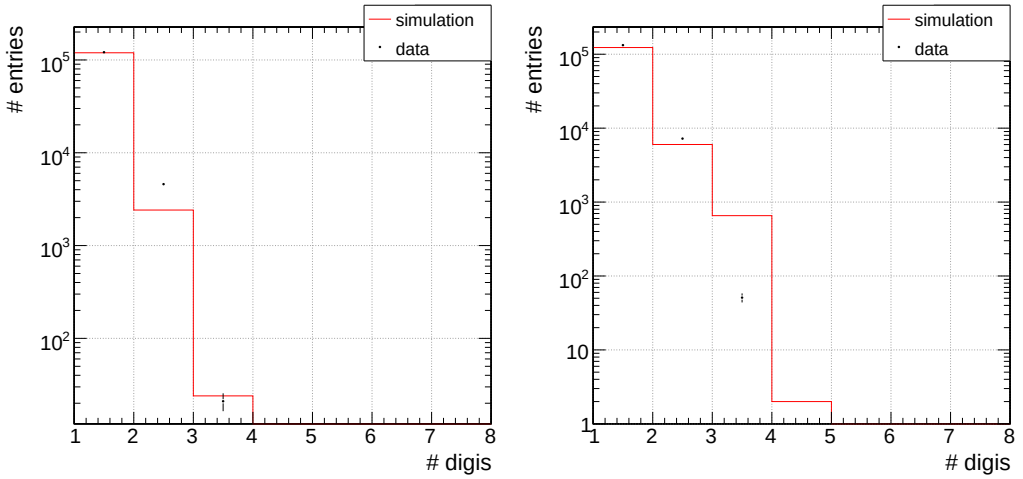

Figure 6.8: *Distributions of the number of digis per cell for simulated and real data. Only digis giving a drift time between -3 and 400 ns are considered. The plots are referred to a 100 GeV/c muon beam without (left) and with (right) iron absorbers.*

In this case, the discrepancy between simulated and real data is smaller, since the contribution of the random noise and of the after-pluses in the se-

lected range of times is almost negligible and the contribution of the pile-up is also less important. This is illustrated in Fig. 6.9 which shows the time difference between the first and the second hit in a cell: comparing to Fig. 6.6 it should be noted that the peak due to photo-electric extraction on the cathode is almost completely suppressed. The different behavior on the trailing edge of

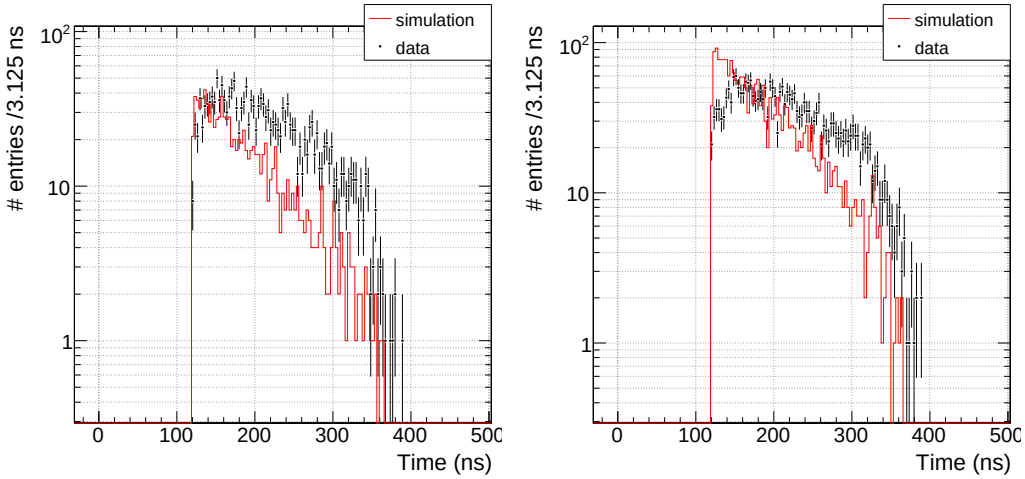

Figure 6.9: *Time difference between the second and the first digi in the cells of one r-ϕ superlayer of MB3 chamber. Only digi times between -3 and 400 ns are considered. The plots are referred to a 100 GeV/c muon beam without (left) and with (right) iron absorbers.*

the distribution is due to the efficiency of the TDC to the second hit which is not reproduced by the simulation; this is however a minor effect.

We conclude that for the hits relevant in the reconstruction the agreement between data and simulation is acceptable.

The overall multiplicity of digis per chamber, falling in the time-window used for the reconstruction, in shown in Fig. 6.10. The shape of the distribution is well reproduced especially for high multiplicity events. We can observe a smaller number of digis in the simulation, both with and without the iron slabs inserted: the difference between simulation and data accounts respectively for 4.2% and 6.3% of the total number of digis in the data. This is more than the 1% abundancy expected because of the pile-up hits produced by other muons in the spill discussed previously.

This effect can be due to the GEANT simulation of production of secondary particles in the material or to the hits which are discarded during the digitization. To understand this, the relative fraction of the various processes contributing to the GEANT hit multiplicity in the sensitive volume is shown in Fig. 6.11 for the two considered setups. Due to the particular geometric configuration

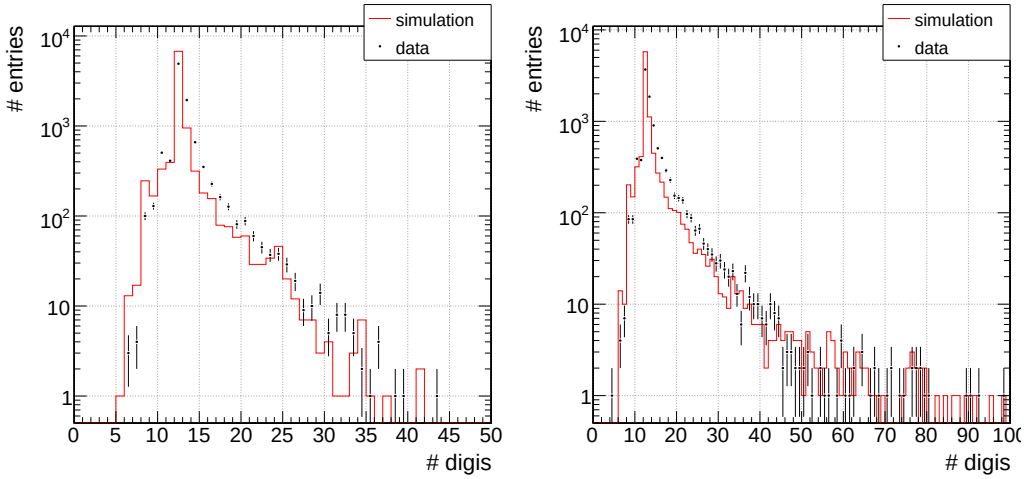

Figure 6.10: *Distributions of the number of digis per chamber for simulated and real data. Only digis giving a drift time between -3 and 400 ns are considered. The plots are referred to a 100 GeV/c muon beam without (left) and with (right) iron absorbers.*

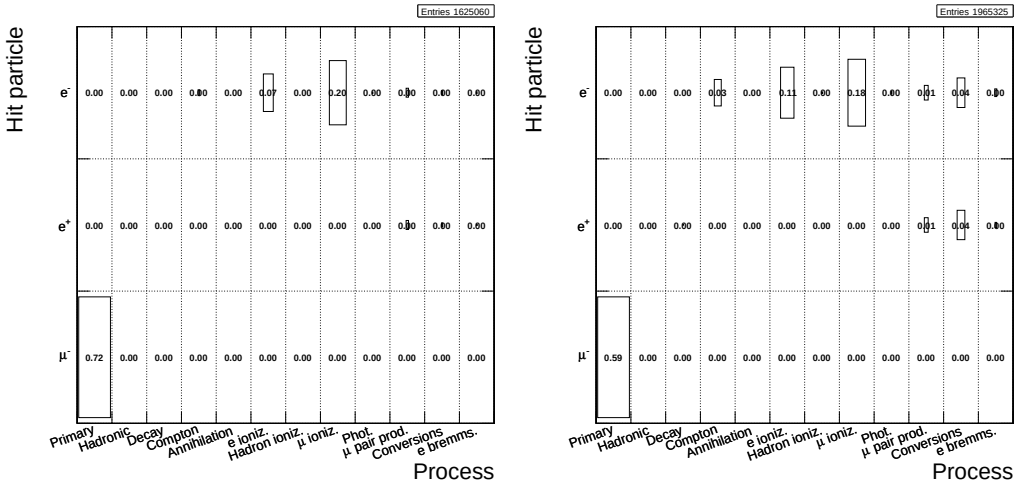

Figure 6.11: *Relative fractions of the various particles and processes for the* GEANT *hits in the gas volume for simulated samples of 50000 muons with momentum of* 100 *GeV/c without (left) and with (right) iron absorbers.*

and to the absence of magnetic field, the fraction of hits which can not be handled by the parametrization is lower than what registered for the simulation of the DTs within the CMS detector (cf. Section 3.3) being 2.6% of the total when simulating the setup without the absorbers and 3.6% in the other case. The relative composition of these hits is shown in Fig. 6.12. Considering that most

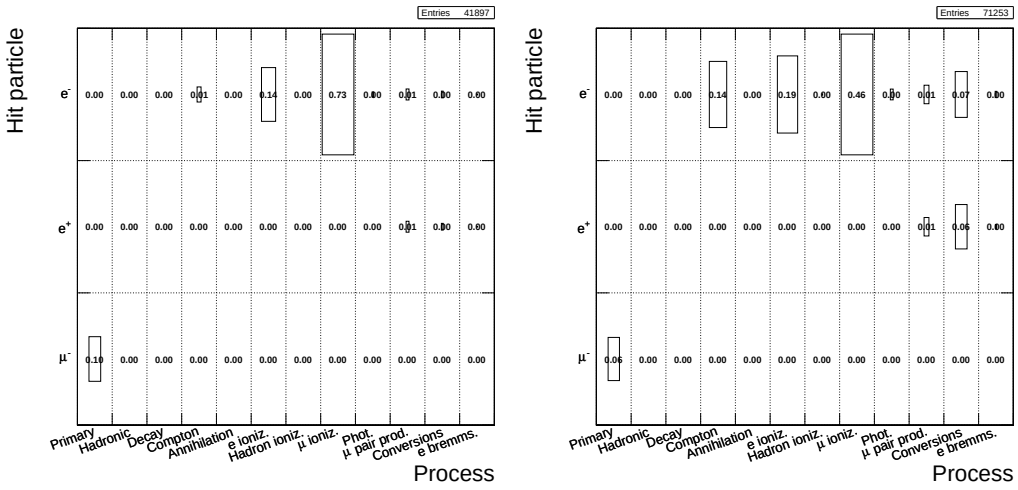

Figure 6.12: *Relative fractions of the various particles and processes for the* GEANT *hits which can not be treated by the* GARFIELD *parametrization. The plots are referred to simulated samples of 50000 muons with momentum of* 100 *GeV/c without (left) and with (right) iron absorbers.*

of these hits are not expected to produce a detectable signal (cf. Section 3.3) this small fraction of hits not digitized is not sufficient to explain the whole observed difference in the number of digis.

We expect that a fine tuning of the GEANT secondary production cuts would improve the agreement between simulation and data, while we see no evidence that the development of a special treatment for the hits not digitized would substantially improve these results.

In order to estimate the contribution of delta-rays and other secondaries to the number of digis it is interesting to plot the meantimer distribution. If we

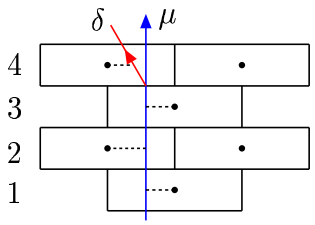

Figure 6.13: *Sketch representation of a muon crossing a semi-column of cells. The meantimer computed using the time of layer 4 will be smaller than the maximum drift time due to the presence of a delta-ray.*

consider the four drift-times (t_1, t_2, t_3, t_4) produced in a semi-column of cells in a

superlayer, as shown in Fig. 6.13, it is possible to compute the two meantimers [1]:

$$T_{\max}^{123} = \frac{(t_1 + t_3)}{2} + t_2; \tag{6.1}$$

$$T_{\max}^{234} = \frac{(t_2 + t_4)}{2} + t_3. \tag{6.2}$$

As explained in Chapter 5, if the three signals detected in the layers are produced from the same track (*i.e.* they are not masked by the occurrence of a δ-ray), the meantimer measures the maximum drift-time in half a cell, independently on the track position and angle. When a delta-ray, or a secondary particle in general, is produced and detected the resulting meantimer is smaller than the maximum drift-time, since the real hit will fall in the TDC dead-time. The plots in Fig. 6.14 show the meantimer distributions of simulated and real data for 100 GeV muon beams. The tails toward smaller times is, for the previous considerations, directly related to the number of delta-rays and other secondaries. In order to avoid any bias due to the different hit multiplicity per cell, only the first hit in each cell was used for the $T_{\max}$ computation.

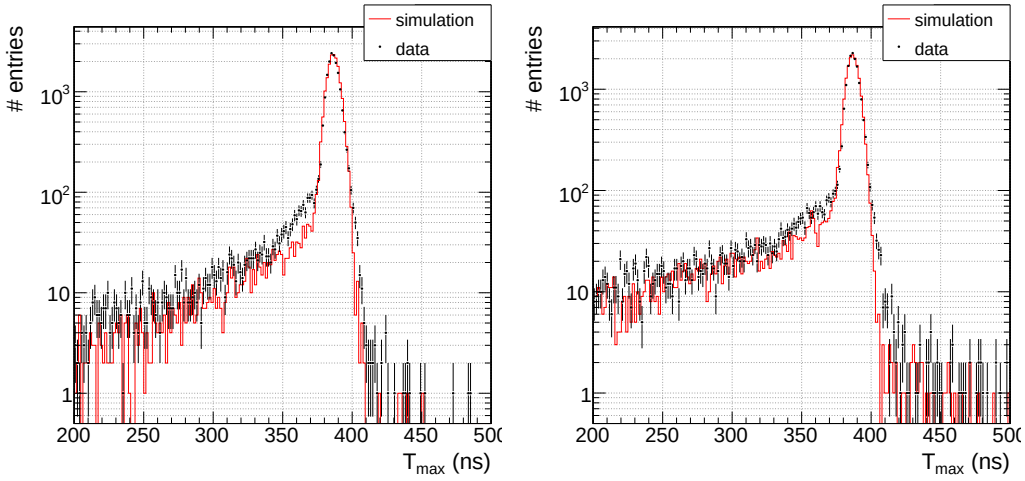

Figure 6.14: *Meantimer distribution for simulated and real data in one r-ϕ superlayer of the MB3 chamber. The plots are referred to a 100 GeV/c muon beam orthogonal to the chambers, without (left) and with (right) iron absorbers.*

Although the simulation appears to slightly underestimate the contribution of delta-rays to the tail, we can consider the agreement between simulated and real data quite satisfactory. In particular, the increasing of secondaries in the data collected with the iron absorbers in place is well reproduced.

[1] The meantimer formula for various patterns of cells and various track angles are listen in Appendix A.

A qualitative estimate of the contribution of soft and hard delta-rays to the secondary multiplicity can be obtained from the scatter plots in Fig. 6.15. They

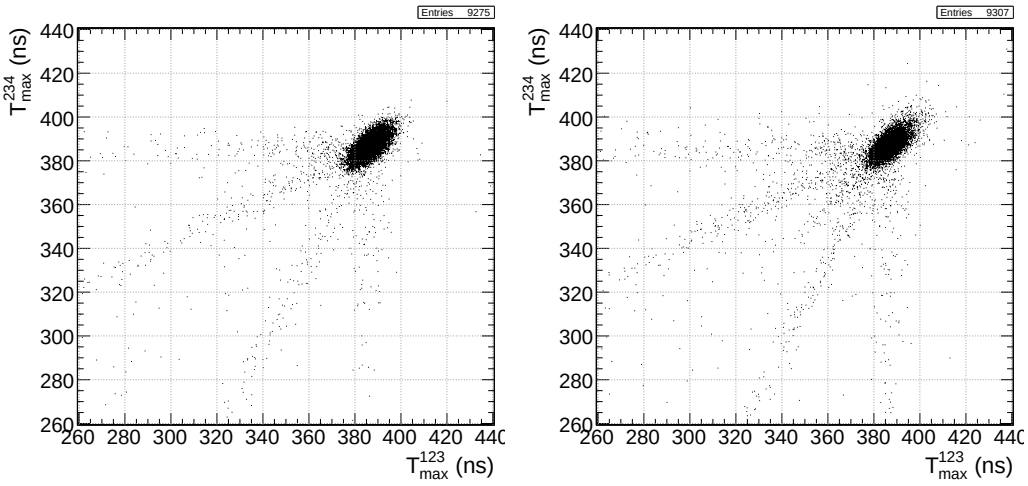

(a) Iron absorbers not inserted, simulated (left) and real (right) data.

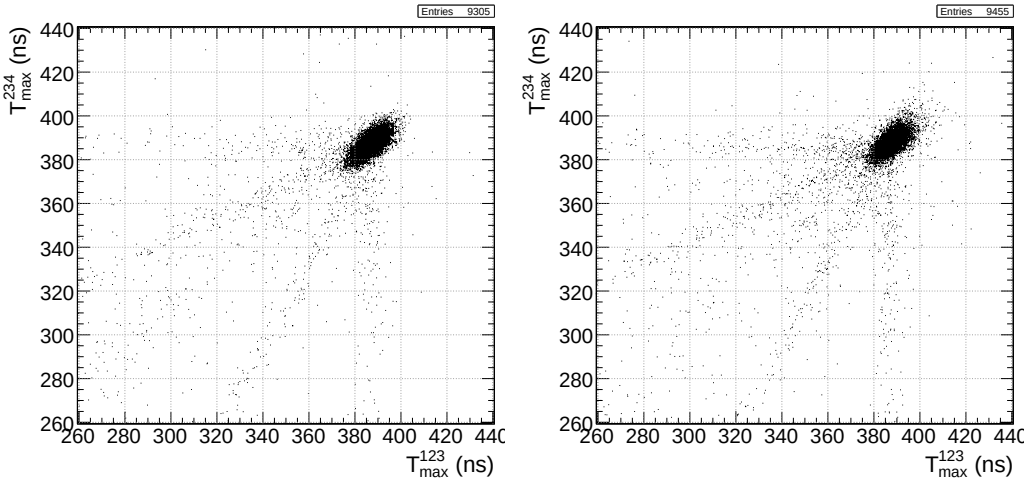

(b) Iron absorbers inserted, simulated (left) and real (right) data.

Figure 6.15: *Meantimer computed with the times of layers 1, 2 and 3 (T^{123}_{max}) versus that computed in layers 2, 3 and 4 (T^{234}_{max}) in one superlayer r-ϕ. The plots are referred to simulated and real data with 100 GeV/c muon beam orthogonal to the chamber without (a) and with (b) iron slabs inserted.*

show the meantimers $T^{123}_{\rm max}$ versus $T^{234}_{\rm max}$. A secondary hit affecting only one layer would result in a correlation between the two meantimers: a secondary in the most external cells will affect only one of the two meantimers, while a delta-ray in one of the central layers will affect both of them, giving a point along one of the two inclined lines. In case of hard secondaries crossing more than one layer

this correlation is lost.

Both in the data and in the simulation the points are mostly distributed along four equally spaced lines demonstrating that most of the delta rays are contained in in a single cell.

Modeling of the cell response. The validation of the GARFIELD parametrization described in Section 3.2.2.1 requires the test of two aspects of the cell response:

- comparison of the average space-time relation in the cell. The parametrization must model the average drift velocity and the effect of the non-linearities for different track configurations;
- comparison of the intrinsic cell resolution. The parametrization must statistically reproduce the effect of the spread of the drift times.

In the following, a comparison of the drift properties of the simulated and real cell is performed, investigating, in particular, the dependence of the drift-time distribution on the track angle. Other interesting information about the modeling of the cell response will be shown in the section about the analysis of the reconstruction results.

The meantimer distributions of Fig. 6.14 contain interesting information about the simulation of the cell behavior. Since the peak of the distribution is a measurement of the maximum drift-time in the semi-cell, it can be used to estimate the average drift velocity in the gas. The agreement of the simulation with the real data is satisfactory, since the Gaussian fit of the peak of the distribution gives in both cases a mean value for the meantimer around 386.5 ns corresponding to a drift-velocity of 54.3 μm/ns. The agreement between simulation and data is satisfactory also for track with larger impact angles, as shown in Table 6.3 which reports the drift velocities for different samples, computed using the meantimer technique described in Section 5.2.

The matching between simulation and data is also satisfactory on the width of the meantimer peak. This is a measurement of the dispersion of the drift times (cf. Section 5.2) and, therefore, of the average cell resolution. As mentioned in Section 6.1.2, to obtain a good agreement a smearing, partially attributed to the resolution of the scintillator trigger, was introduced in the simulation. Both for the simulation and the data, the sigma of the Gaussian fit of the meantimer peak is about 4.5 ns.

Another interesting comparison concerns the shape of the drift-time distribution, a test of the performance and the accuracy of the parametrization of the cell response in the different regions of the cell. The plots in Fig. 6.16 show the drift-time distribution for real and simulated data collected with a 100 GeV muon beam. In order to avoid any bias due to the different hit multiplicity,

only the first hit of each cell is considered in the plots. Note that no additional

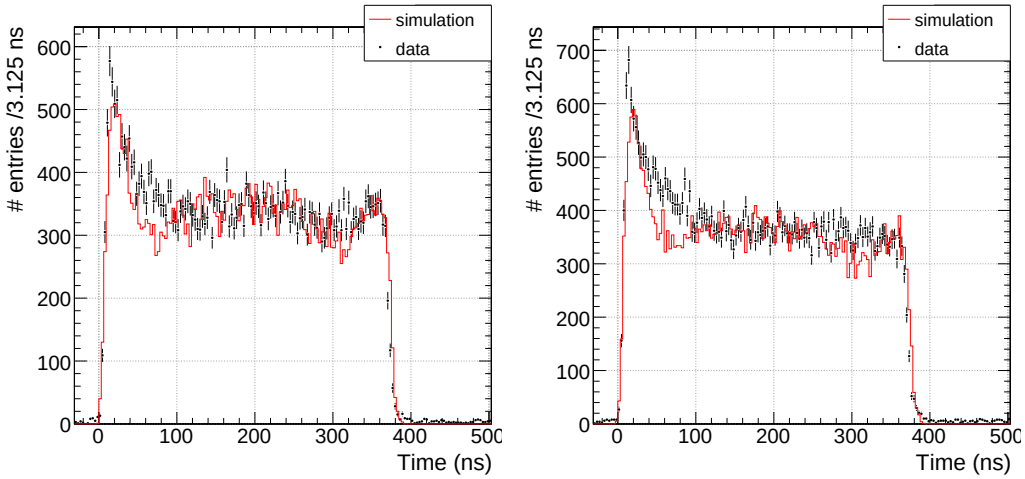

Figure 6.16: *Distributions of the drift-times collected in one r-ϕ superlayer exposed to 100 GeV/c muon beam without (left) and with (right) iron absorbers.*

normalization was applied a part from the selection of events described in Section 6.1.1; the agreement on the number of entries is therefore satisfactory both with and without the absorbers, although small differences in the shape of the distribution are present.

This difference can be explained taking into account the different beam profile in the real data taking and in the simulation: for not uniformly illuminated cells the shape of the time box is distorted.

In order to account for this effect, the same plots of Fig. 6.16 were produced considering only the digis in one uniformly illuminated cell of each layer in a superlayer r-ϕ. The resulting plots are shown in Fig. 6.17, again for the runs at 100 GeV/c with and without the absorbers. Due to the differences in the beam profile, in this case, the number of hits in the cell was different for simulation and reality, the two plots have been therefore normalized to the number of entries between 0 and 400 ns. These time boxes show very good agreement between data and simulation apart from a small excess of hits under the peak at small times, corresponding to the region close to the anode wire. In both case the bulk of the distribution is smooth and the trailing edge drops sharply, as expected for a cell with saturated drift velocity.

In order to test the response the parametrization at different angles the same selection of uniformly illuminated cells was applied also to data taken with different rotation angles of the MB3 chamber with respect to the 150 GeV muon beam. The resulting plots are shown in Fig. 6.18 for impact angles of 0°, 10°, 20° and 30°. In all cases the agreement is satisfactory. The non-linearities occurring at large impact angles are well reproduced by the parametrization.

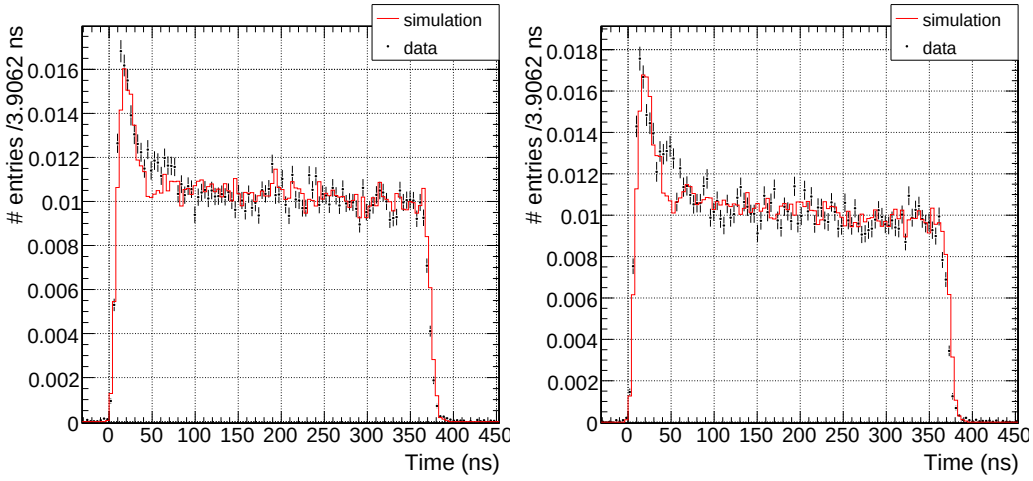

Figure 6.17: *Drift-time distributions for data and simulation for 100 GeV/c muon beam orthogonal to the chamber, without (left) and with (right) iron absorbers. The plots are referred to one uniformly illuminated cell of each layer of r-ϕ superlayer in MB3 chamber. The distributions are normalized to the number of entries between 0 and 400 ns.*

6.3 Local Reconstruction with Test-Beam Data

The comparison of the local reconstruction performed on simulated and real test-beam data allows to:

- compare the performance (resolution, etc...) of the reconstruction;
- study of the performance of the GARFIELD parametrization for the mono-dimensional hit reconstruction.

The first topic is mainly a test of the impact of the differences observed in the previous section between data and simulation. The hit multiplicity may affect the pattern recognition and therefore the segment reconstruction. Moreover, the modeling of the cell response during the digitization procedure directly determines the cell resolution and its behavior in the different regions of the cell.

For this test the reconstruction has been performed using a constant drift velocity (cf. Section 4.2.1) over the entire cell, in order to disentangle the performance of the parametrization used during the digitization from that of the parametrized drift velocity reconstruction algorithm.

The second topic is a test of the GARFIELD parametrization for the reconstruction (cf. Section 4.2.2), consisting in the study of its behavior for various

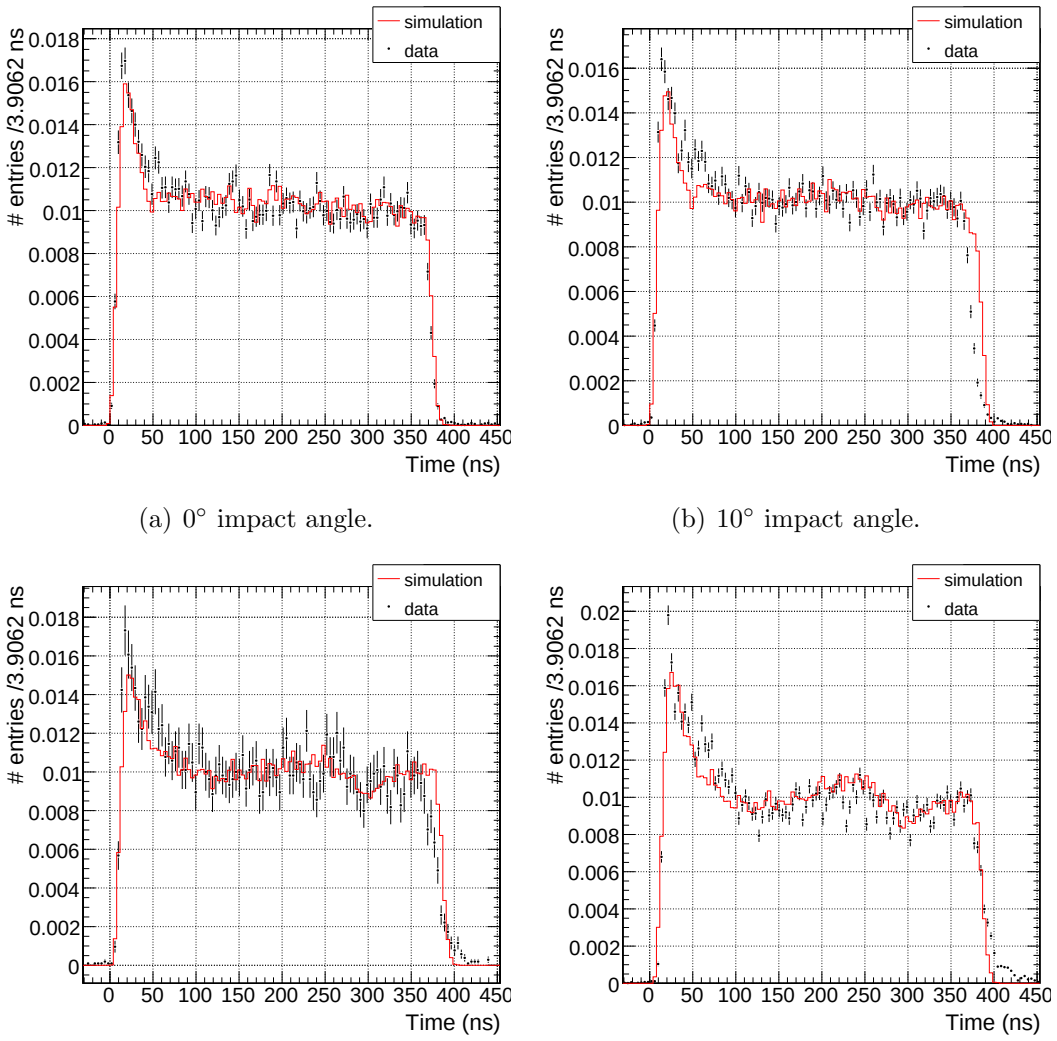

(a) 0° impact angle.

(b) 10° impact angle.

(c) 20° impact angle.

(d) 30° impact angle.

Figure 6.18: *Drift-time distributions for data and simulation for different impact angles of the 150 GeV/c muon beam with respect to the normal to the chamber: 0° (a), 10° (b), 20° (c) and 30° (d). The plots are referred to the uniformly illuminated cell of each layer of r-ϕ superlayer in MB3 chamber. The distributions are normalized to the number of entries between 0 and 400 ns.*

track angles.

In order to perform an unbiased comparison, the same event selection described before has been applied also for this study: the distributions presented in the following have been normalized to the number of selected events having only one clean track and no shower activity in MB1.

6.3.1 Reconstruction Using a Constant Drift-velocity.

Synchronization and calibration. The reconstruction of the test-beam data first of all represents an important benchmark for the synchronization and calibration procedures described in Chapter 5. Real and simulated data have been treated with the same calibration procedures.

Concerning the computation of the time pedestals, in both cases the t_{trig} has been computed directly from the distribution of the drift times, as described in Section 5.1.2, without using the knowledge of the offsets set during the digitization. In both cases, no further corrections for the time-of-flight and for the signal propagation along the wire were needed: since the the area illuminated by the beam was small the jitter introduced by these delays is negligible. The only difference between simulation and real data is the subtraction of the relative t_0 offset (cf. Section 4.1.1), which, in the first case, is not needed.

The calibration of the drift velocity based on the meantimer technique was used in both data and simulation. The drift velocity was computed for each of the analyzed samples and, in particular, for each of the data sets taken at different impact angles of the beam on the MB3 chamber. The resulting velocities obtained on real and simulated samples are listed in Table 6.3. As

Table 6.3: *Drift velocities computed with the meantimer technique (cf. Section 5.2) for data and simulation and for different impact angles of the 150 GeV muon beam with respect to the normal to the chamber.*

Impact Angle	Simulation (μm/ns)	Data (μm/ns)
0°	54.3	54.3
10°	54.4	54.4
20°	54.5	54.5
30°	54.7	54.6

already mentioned, the agreement between the two set of values demonstrates that the angular dependence of the effective drift velocity is well described in the digitization.

Performance of the Local Reconstruction. As already discussed in the previous section and shown in Fig. 6.5, the number of digis with a drift-time suitable for the reconstruction (-3 to 400 ns) is slightly underestimated in the simulation, therefore also the number of one-dimensional hits reconstructed at the cell level is underestimated of the same amount: 4.2% of the total hits when running without absorbers and 6.3% when running with the iron slabs.

The resulting number of three-dimensional segments reconstructed in the MB3 chamber per event is shown in Fig. 6.19. The agreement between simulation and real data is satisfactory even if the number of segments is slightly underestimated when the iron slabs are inserted.

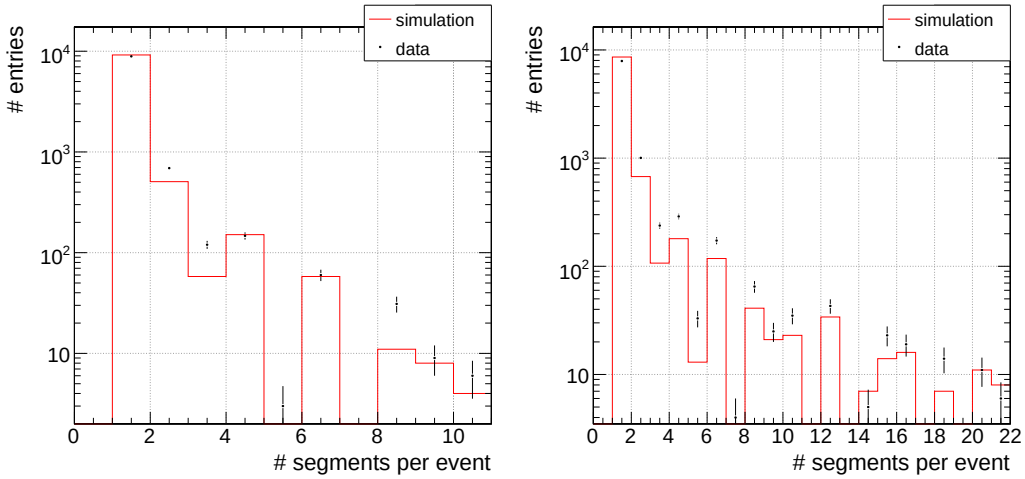

Figure 6.19: *Number of three-dimensional segments per event reconstructed in the MB3 chamber for simulation and data. The plots are referred to the 100 GeV/c muon beam orthogonal to the chamber without (left) and with (right) iron absorbers.*

The plots in Figures 6.20, 6.21, 6.22 and 6.23 show the residuals on the reconstructed distance from the wire for different angles (0°, 10°, 20°, and 30° respectively) of the 150 GeV/c muon beam with respect to the normal to the chamber. The two plots at the top of each figure refer to the simulation while the two at the bottom are the results obtained on real data.

These residuals are computed comparing the hit distance from the wire with that resulting from the extrapolation of the segments it belongs to, since no external tracking system was available for the measurement of the muon position [2]. The width of these distributions receive a contribution from the additional smearing of the digi times described in Section 6.1.2 and this should be taken into account when comparing the results presented in this section with the residual distributions presented in Section 4.2.3 for the simulation.

The agreement between data and simulation is quite satisfactory for all considered angles. The sigmas of the Gaussian fit of these regions vary from 180 μm, for tracks orthogonal to the chamber, to almost 250 μm for 30° segments

[2]Note that, due to the fact that the hits are used in the fit of the segment, the width of this distribution is not the actual resolution on the measurement which can be estimated from the sigma through simple algebraic relations as described in [42].

and the values obtained for data and simulation are in general compatible. The simulation slightly underestimates the non-Gaussian tails of the distributions.

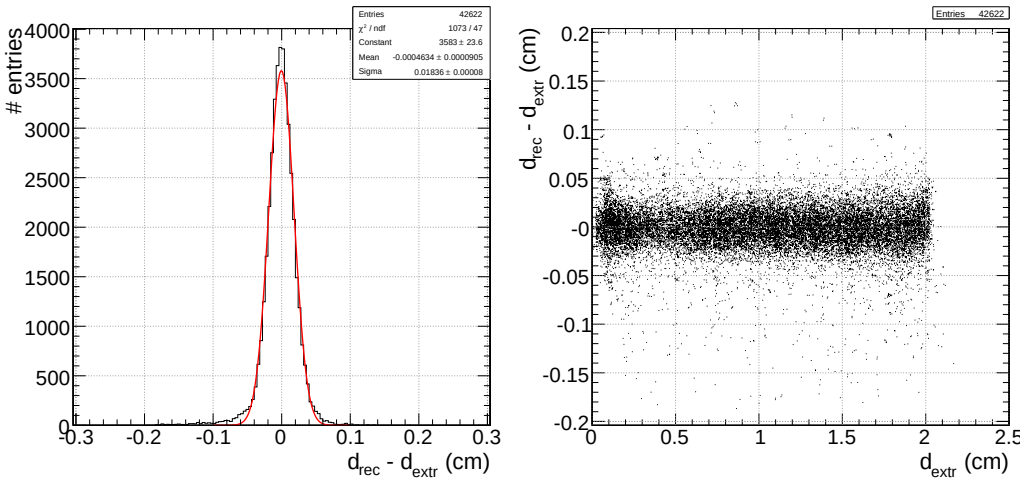

(a) Simulation, 0° impact angle.

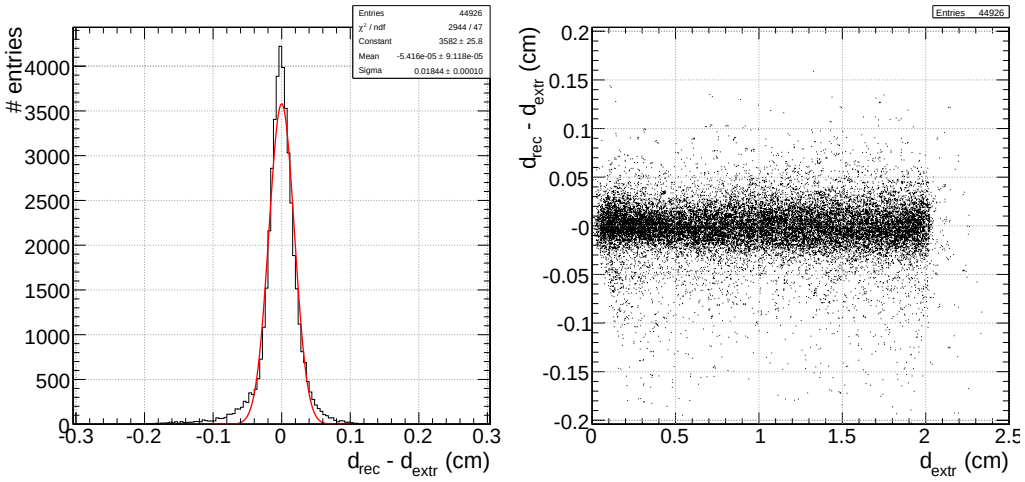

(b) Data, 0° impact angle.

Figure 6.20: 0° impact angle. *Residuals on the distance from the wire of 1D RecHits reconstructed using a constant drift velocity over the entire cell volume. The residuals are computed comparing the reconstructed value with the segment extrapolation on the mid plane of the cell. The plots on the right show the residuals versus the extrapolated distance. The plots are referred to one r-ϕ superlayer of MB3 chamber for simulation (a) and data (b) with 150 GeV/c muons with impact angle of 0° with respect to the normal to the chamber.*

It is also very interesting to compare the scatter plots of the residuals as a function of the distance from the wire. This is, in fact, a further proof of

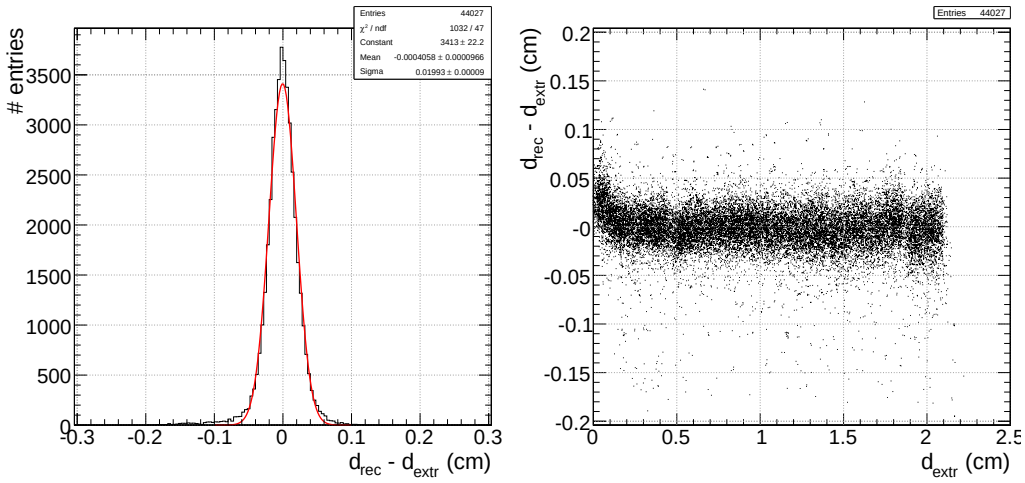

(a) Simulation, 10° impact angle.

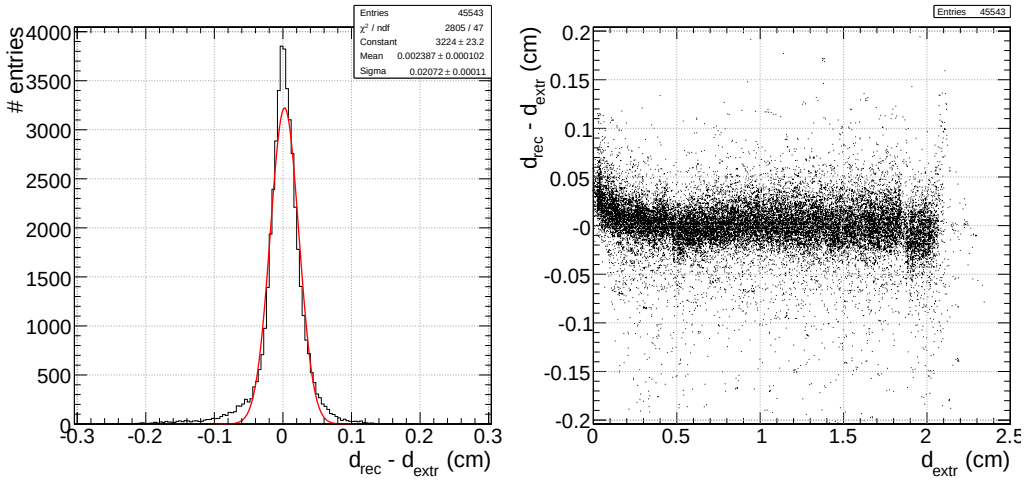

(b) Data, 10° impact angle.

Figure 6.21: 10° **impact angle.** *Residuals on the distance from the wire of 1D RecHits reconstructed using a constant drift velocity over the entire cell volume. The residuals are computed comparing the reconstructed value with the segment extrapolation on the mid plane of the cell. The plots on the right show the residuals versus the extrapolated distance. The plots are referred to one r-ϕ superlayer of MB3 chamber for simulation (a) and data (b) with 150 GeV/c muons with impact angle of 10° with respect to the normal to the chamber.*

the reliability of the parametrization used to model the cell response during the simulation. The non linearities are well reproduced, especially in the region close to the anode, where they are more important. The agreement is less satisfactory in the cathode region; this is however the region of the cell where

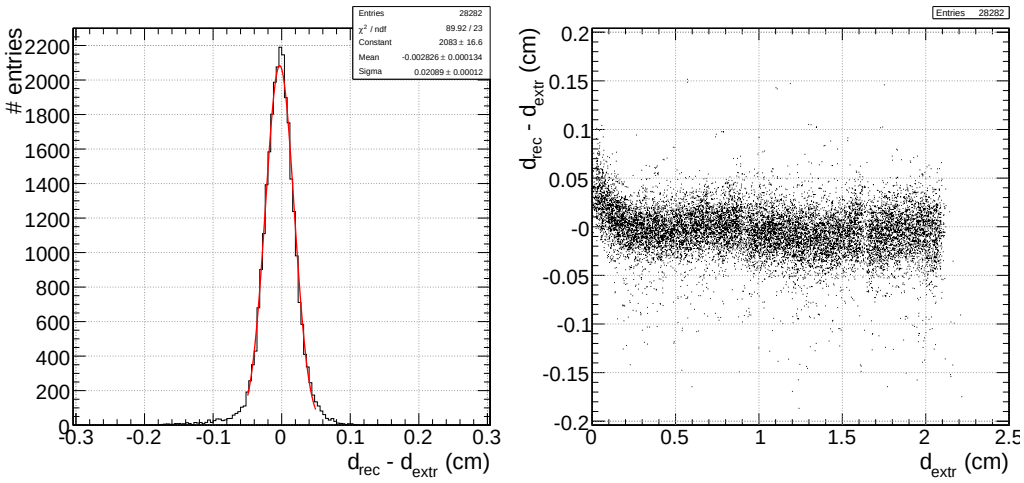

(a) Simulation, 20° impact angle.

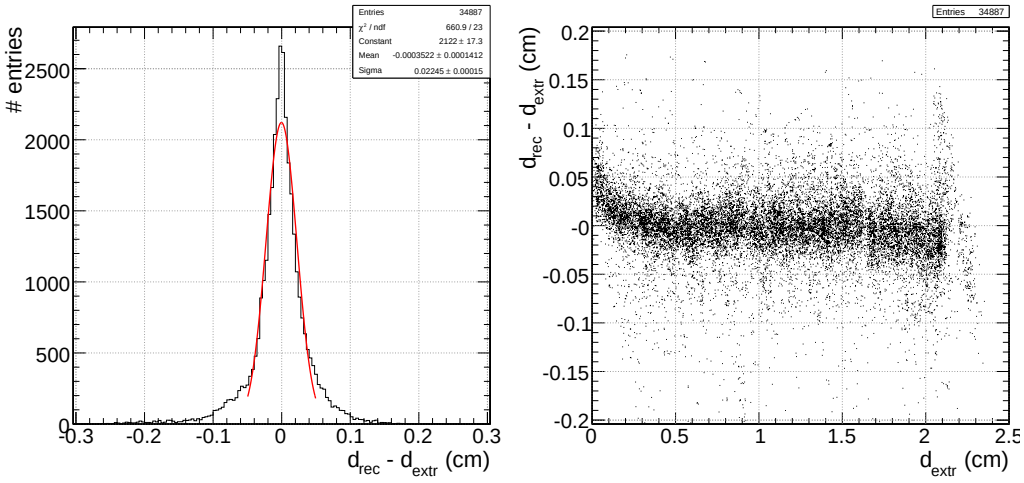

(b) Data, 20° impact angle.

Figure 6.22: 20° **impact angle.** *Residuals on the distance from the wire of 1D RecHits reconstructed using a constant drift velocity over the entire cell volume. The residuals are computed comparing the reconstructed value with the segment extrapolation on the mid plane of the cell. The plots on the right show the residuals versus the extrapolated distance. The plots are referred to one r-ϕ superlayer of MB3 chamber for simulation (a) and data (b) with 150 GeV/c muons with impact angle of 20° with respect to the normal to the chamber.*

the relative weight of the non linearities with respect to the drift distance is smaller.

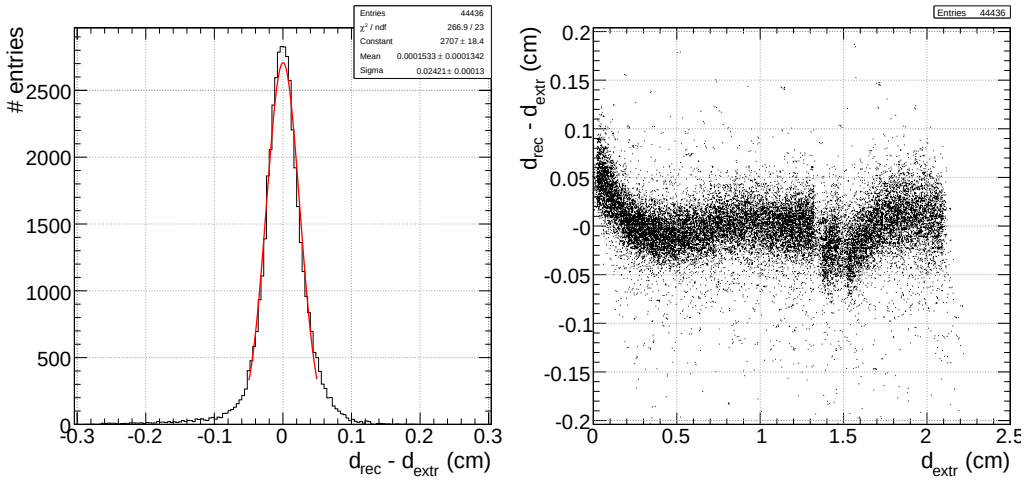

(a) Simulation, 30° impact angle.

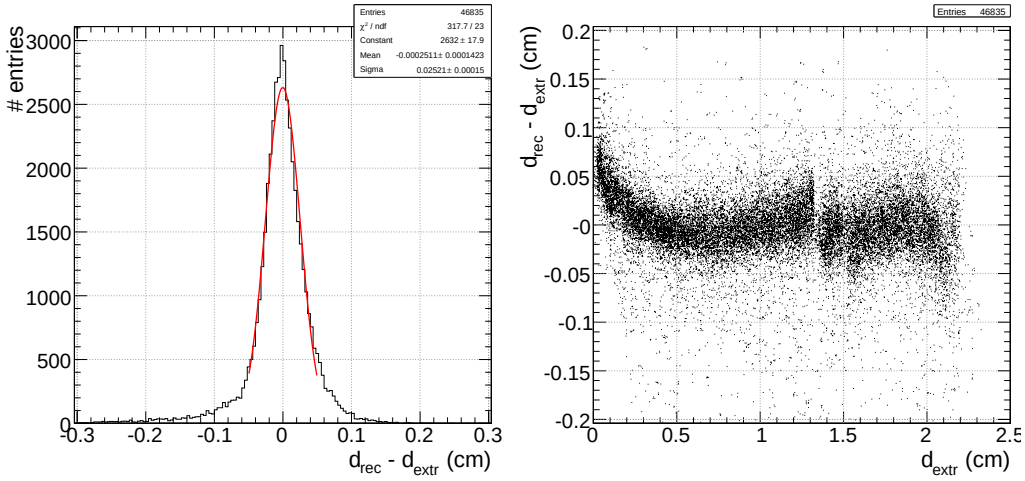

(b) Data, 30° impact angle.

Figure 6.23: 30° **impact angle.** *Residuals on the distance from the wire of 1D RecHits reconstructed using a constant drift velocity over the entire cell volume. The residuals are computed comparing the reconstructed value with the segment extrapolation on the mid plane of the cell. The plots on the right show the residuals versus the extrapolated distance. The plots are referred to one r-ϕ superlayer of MB3 chamber for simulation (a) and data (b) with 150 GeV/c muons with impact angle of 30° with respect to the normal to the chamber.*

6.3.2 Reconstruction Using the GARFIELD Parametrization

Finally, the data recorded in the test-beam were used to study the performance of the reconstruction algorithm based on the GARFIELD parametrization of the cell (cf. Section 4.2.2).

In particular the test of the parametrization for various muon impact angles on the MB3 chamber has been performed. This test is not exhaustive since no data acquired with magnetic field were available; as already explained in Section 3.2.2.1 the presence of the magnetic field has a non-negligible impact on the average drift velocity and, in case of components parallel to the wire, on the residual non-linearities which become more important.

Note that the calibration of the time pedestals is particularly critical for the reconstruction using the GARFIELD parametrization and it has been therefore performed as explained in Section 5.1.2.

The reconstruction efficiency for three-dimensional segments, which was already close to 100% using the constant drift velocity, remains almost unchanged when the reconstruction is performed with the parametrization.

The residuals obtained with this algorithm are shown in Fig. 6.24 for the various impact angles. As already explained they have been computed comparing the reconstructed distance from the wire with the distance resulting from the segment extrapolation. The width of the distribution is unchanged with respect to the linear drift algorithm for tracks orthogonal to the chamber (Fig. 6.24(a)) while sensible improvements are obtained for wider impact angles. This illustrated in Fig. 6.25, where the sigma of the Gaussian fit to the residuals distribution at the various angles are plotted for the constant drift velocity and the parametrization algorithms. The improvement in the sigma goes from 3% for 10° tracks to almost 10% for 30° angles.

In particular, looking to the scatter plots of the residuals as a function of the extrapolated distance from the wire in Fig. 6.24 and comparing them with the corresponding plot in Figures 6.20 - 6.23 it is clear that the parametrization accounts in an accurate way for the non-linearities in the region close to the anode, sensibly reducing the residuals.

Despite these satisfactory results the scatter plots for 20° and 30° impact angles (Figures 6.24(c) and 6.24(d) respectively) still show the effect on the reconstruction of non-linearities not completely corrected by the parametrization.

6.4 Conclusions

This chapter presents the validation of the simulation and digitization chain using the data acquired during the test-beam of the Autumn 2004.

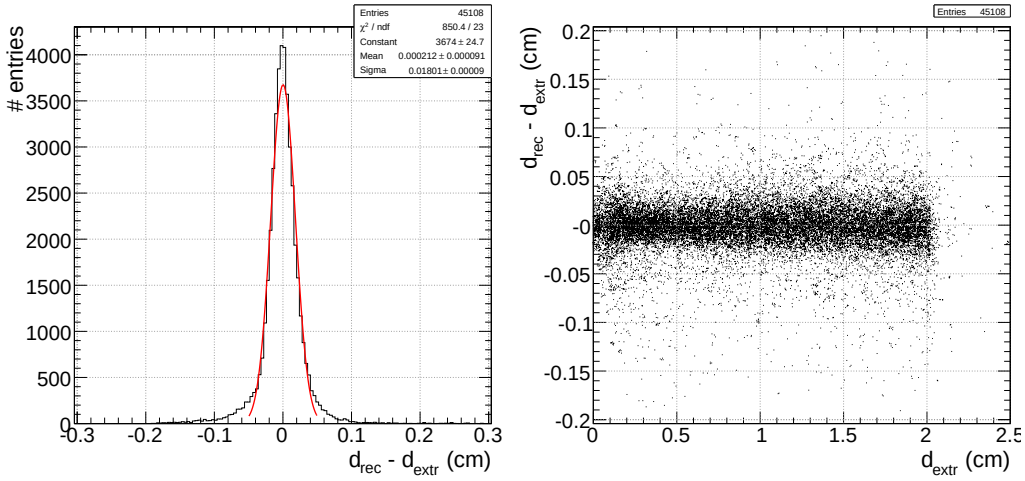

(a) Impact angle of 0°

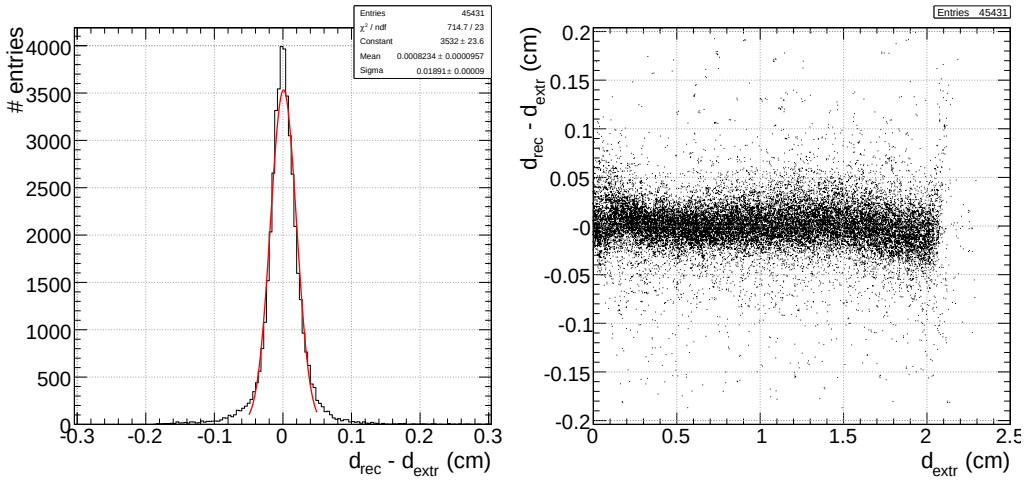

(b) Impact angle of 10°

Figure 6.24: *Residuals on the distance from the wire of 1D RecHits reconstructed using the* GARFIELD *parametrization. The residuals are computed comparing the reconstructed value with the segment extrapolation on the mid plane of the cell. The plots on the right show the residuals versus the extrapolated distance. The plots are referred to data acquired in one r-ϕ superlayer of the MB3 chamber for 150 GeV/c muons with different impact angles with respect to the normal to the chamber: 0° (a), 10° (b), 20° (c) and 30° (d).*

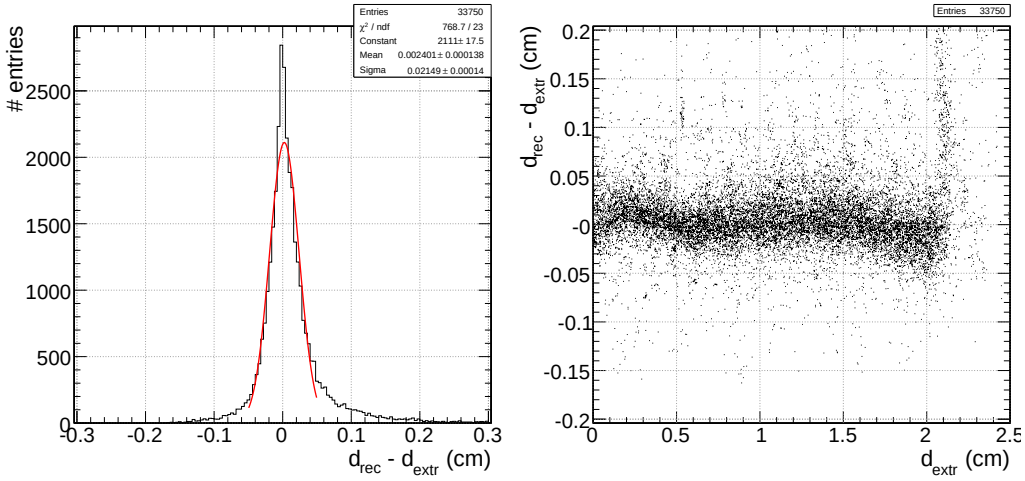

(c) Impact angle of 20°

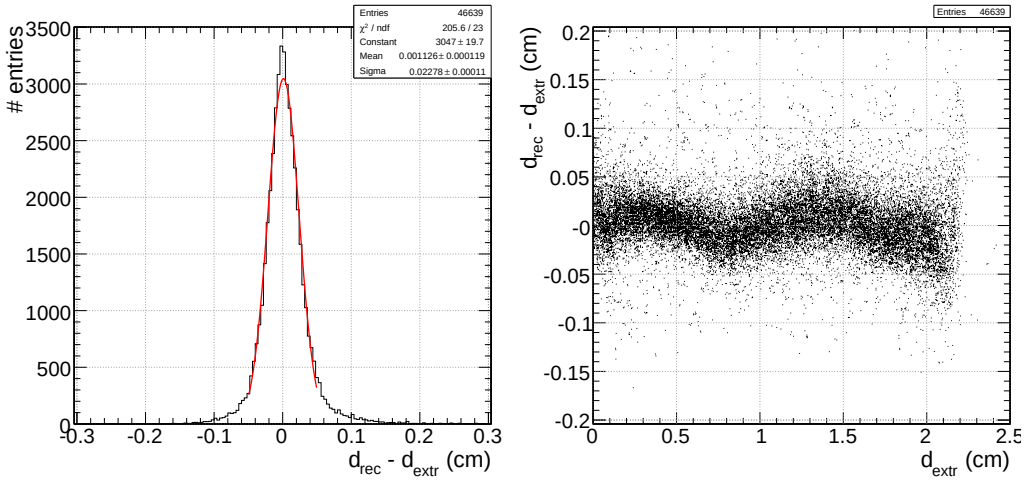

(d) Impact angle of 30°

Figure 6.24: continued.

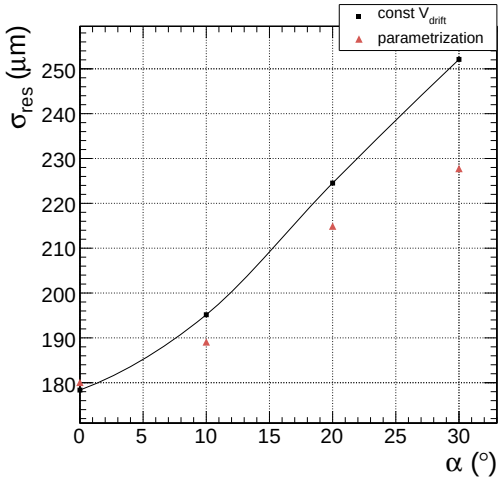

Figure 6.25: *Sigmas of the Gaussian fit to the residual distributions for different impact angles obtained with the constant drift velocity and the parametrization on real data.*

The overall performance of the simulation of the DT response is quite satisfactory. The small differences in the multiplicity of hits in the sensitive volume with respect to the real data will require a fine tuning of the production thresholds for secondary particles in the GEANT simulation. This is left for further studies.

The data show that the choice of not considering in the simulation effects such as the random noise in the tubes and the production of after-pulse signals is justified, since their effect on the reconstructed quantities is almost negligible.

The modeling of the cell response with the GARFIELD parametrization describes well the behavior of the cell at different impact angles; this is demonstrated both by the agreement of drift-time distributions for real and simulated data and by the study of the cell resolutions for different track angles. To reproduce the cell resolution it is necessary to introduce an additional smearing of 2.4 ns in the digitization. This smearing is in part due to the resolution of the scintillator trigger used for this particular data taking. It has been introduced in the simulation as a tuning parameter; once its value has been tuned the resolution is perfectly reproduced for all muon impact angles.

The test-beam data have also been an opportunity for the study of the performance of the local reconstruction and, in particular, for the test of the GARFIELD time-to-distance parametrization used for the reconstruction of the hits in the cell volume. The modeling of the non-linearities of the space time relation for the ionization electrons allows to sensibly improve the resolution. The impact of the parametrization is expected to be even more important when running with magnetic field since residual components parallel to the wire are

expected to increase the non-linear behavior of the drift field. Further tests, using data acquired with magnetic field are needed to confirm this hypothesis.

This study have also been a benchmark for the calibration strategies described in Chapter 5. The algorithms for the determination of the time pedestals have demonstrated their robustness against noise and possible instrumental effects. The reliability of the meantimer algorithm for the calibration of the drift velocity has been demonstrated by the calibration of runs acquired at different impact angles of the muon beam: the usage of the different formulas for different track patterns allows to account for the angular dependence of the effective drift velocity.

The analysis of real data is particular important also from the technical point of view to test the readiness of the reconstruction software to the real data taking as far as reading of the detector raw data, handling of the mapping between readout channels and wires and management of the calibration constants is concerned. The experience acquired during this analysis has been of great importance for the Magnet Test and Cosmic Challenge (MTCC) when the reconstruction algorithms described in Chapter 4 have been used on-line for DQM tasks.

The analysis of the data acquired during the MTCC is on-going and it will include further tests of the simulation chain validating, in particular, the response of the DT chambers in presence of the final CMS magnetic field.

Summary

A reliable simulation of the muon detectors and a robust muon reconstruction are relevant for the study of many physics channels since muons represent a clear signature in the LHC hadronic environment.

The subject of this thesis is the simulation of the DT chamber response and the calibration and local reconstruction of these detectors.

The simulation consists in the modeling of the cell response to crossing particles, taking into account their interaction with the detector material and the drift properties of the cell. The output of the simulation are simulated TDC measurements.

The local reconstruction is the first step of the muon reconstruction, it starts from the output of the Data Acquisition System and builds track segments at the chamber level. The position and the direction measured by these segments are the basic ingredients for the muon track fit both in the on-line High Level Trigger selection and in the off-line reconstruction.

The calibration consists in the computation of the drift-time pedestals and of the drift velocity used by the local reconstruction algorithms.

The work presented here covers both the implementation and the study of the performance of the simulation, reconstruction and calibration algorithms. In particular, concerning the simulation of the cell response, the study of the reliability of the whole chain requires the comparison with real data. For this reason the data acquired during the 2004 test beam have been studied and compared with the simulation. The results have been documented in the CMS Note [41] submitted in January 2006 and in the Physics Technical Design Report [1]. This study has been repeated in this thesis using the new framework of the CMS software. It is shown that the agreement between simulated and real data is satisfactory and the parametrization used to model the time response of the cell well reproduces the behavior of the drift field.

The 2004 test beam data have also been used for the test of the calibration algorithms presented in this thesis and for the study the performance of the local reconstruction. The two algorithms for the reconstruction of the hits in the cell volume have been tested and compared; they demonstrated to be robust and reliable. In particular, the parametrization of the time-to-distance relation

allows to improve the resolution with respect to the reconstruction using a constant drift velocity, since it accounts for the effect of the cell non-linearities for inclined tracks.

The simulation and reconstruction algorithms described in this thesis have been used for the study of the CMS physics reach presented in the Physics Technical Design Report Volume II submitted in June 2006 [2].

A further test for the reconstruction and calibration algorithms has been the Magnet Test and Cosmic Challenge. The local reconstruction has been used for Data Quality Monitoring tasks, running on-line. The calibration procedures have been used by the community for the analysis of the data. They demonstrated to fit the flexibility requirements imposed by different running conditions and to meet the needs of the user community.

Appendix A

Meantimer Computation for the Calibration of the Drift Velocity

In the current section all the meantimer equations used for the calibration of the drift-velocity with the algorithm described in Section 5.2 are presented.

The meantimer equations are mathematical relations between the drift times produced by a crossing tracks in three different layers and the maximum drift time in a semi-cell (T_{max}).

The meantimer formulas depend on the track angle and on the pattern of crossed semi-cells [43] and can be demonstrated through simple geometric considerations.

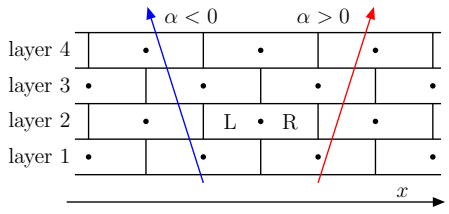

Figure A.1: *Sketch representation of a superlayer with the definition of the convention about the track segment angle and the pattern of semi-cell crossed by the track.*

Table A.1 reports all the equations implemented for the calibration of the drift-velocity together with the corresponding segment angle and cell pattern. A sketch representation of the superlayer is shown in Fig. A.1 for the definition of the convention used in the table.

Table A.1: *Meantimer equations for different track angles and patterns of hit semi-cells [44]. The definition of the sign of the segment angle α is given in Fig. A.1. The pattern is defined through four labels, one for each layer: L and R stand for left and right semi-cells respectively. The label enclosed in parenthesis is referred to the layer not directly used in the T_{max} computation. The time t_i is the measurement in the cell belonging to the layer i.*

ID	Meantimer formula	Segment direction	Semi-cell pattern
	Layers 1-2-3		
123LRL	$T_{max} = (t_1 + t_3)/2 + t_2$	$\forall$	LRL(L/R)
123RLR			RLR(L/R)
123LLR	$T_{max} = (t_3 - t_1)/2 + t_2$	$\alpha > 0$	LLR(L/R)
123RRL		$\alpha < 0$	RRL(L/R)
123LRR	$T_{max} = (t_1 - t_3)/2 + t_2$	$\alpha > 0$	LRR(L/R)
123RLL		$\alpha < 0$	RLL(L/R)
	Layers 1-2-4		
124LRR(1)	$T_{max} = 3t_2/2 + t_1 - t_4/2$	$\forall$	LR(L)R
124RLL(1)			RL(R)L
124LLR	$T_{max} = 3t_2/2 - t_1 + t_4/2$	$\alpha > 0$	LL(L/R)R
124RRL		$\alpha < 0$	RR(L/R)L
124LLL(1)	$T_{max} = 3t_2/2 - t_1 - t_4/2$	$\alpha > 0$	LL(R)L
124LRR(2)			LR(R)R
124RRR(1)		$\alpha < 0$	RR(L)R
124RLL(2)			RL(L)L
124RRR(2)	$T_{max} = -3t_2/2 + t_1 + t_4/2$	$\alpha > 0$	RR(L)R
124LLL(2)		$\alpha < 0$	LL(R)L
124RLR	$T_{max} = 3t_2/2 + t_1 + t_4/2$	$\alpha > 0$	RL(L/R)R
124LRL		$\alpha < 0$	LR(L/R)L
124LRL	$T_{max} = 3t_2/4 + t_1/2 + t_4/4$	$\alpha > 0$	LR(L/R)L
124RLR		$\alpha < 0$	RL(L/R)R

Table A.1: *(continued)*

ID	Meantimer formula	Segment direction	Semi-cell pattern
124LRR(3)	$T_{max} = 3t_2/4+t_1/2-t_4/4$	$\alpha > 0$	LR(R)R
124RLL(3)		$\alpha < 0$	RL(L)L
	Layers 1-3-4		
134LLR(1)	$T_{max} = 3t_3/2 + t_4 - t_1/2$	$\forall$	LRLR
134RLR(1)			RLRL
134LRR	$T_{max} = 3t_3/2 - t_4 + t_1/2$	$\alpha > 0$	L(L/R)RR
134RLL		$\alpha < 0$	R(L/R)LL
134RRR(1)	$T_{max} = 3t_3/2 - t_4 - t_1/2$	$\alpha > 0$	R(L)RR
134LLL(1)		$\alpha < 0$	L(R)LL
134LLL(2)	$T_{max} = -3t_3/2+t_4+t_1/2$	$\alpha > 0$	L(R)LL
134RRR(2)		$\alpha < 0$	R(L)RR
134LRL	$T_{max} = 3t_3/2 + t_4 + t_1/2$	$\alpha > 0$	L(L/R)RL
134RLR		$\alpha < 0$	R(L/R)LR
134RLR	$T_{max} = 3t_3/4+t_4/2+t_1/4$	$\alpha > 0$	R(L/R)LR
134LRL		$\alpha < 0$	L(L/R)RL
134LLR(2)	$T_{max} = 3t_3/4+t_4/2-t_1/4$	$\alpha > 0$	LLLR
134RLR(2)		$\alpha < 0$	RRRL
	Layers 2-3-4		
234RLR	$T_{max} = (t_2 + t_4)/2 + t_3$	$\forall$	(L/R)RLR
234LRL			(L/R)LRL
234LRR	$T_{max} = (t_2 - t_4)/2 + t_3$	$\alpha > 0$	(L/R)LRR
234RLL		$\alpha < 0$	(L/R)RLL
234LLR	$T_{max} = (t_4 - t_2)/2 + t_3$	$\alpha > 0$	(L/R)LLR
234RRL		$\alpha < 0$	(L/R)234RRL

References

[1] The CMS Collaboration, *CMS Physics: Technical Design Report. Volume I: Detector Performance and Software*, CERN/LHCC 2006-01, CMS TDR 8.1 (2006).

[2] The CMS Collaboration, *CMS Physics: Technical Design Report. Volume II: Physics Performance*, CERN/LHCC 2006-021, CMS TDR 8.2 (2006).

[3] M. Guidry, *Gauge Field Theories: an Introduction with Applications*, Wiley Publications, 1991.

[4] T. Hambye and K. Riesselmann, *Matching conditions and Higgs mass upper bounds revisited*, Phys. Rev. D **55** (1997) 7255.

[5] The LEP Electroweak Working Group, *LEP Electroweak Working Group web site*, Located at http://lepewwg.web.cern.ch/LEPEWWG/.

[6] LEP Working Group for Higgs boson searches, *Search for the standard model Higgs boson at LEP*, Phys. Lett. **B565** (2003) 61. hep-ex/0306033.

[7] G. Altarelli and M. L. Mangano (editors), *Proceedings of the Workshop on Standard Model Physics (and more) at the LHC* (2000) CERN 2000-004.

[8] The LHC Study Group, *The Large Hadron Collider Conceptual Design*, CERN/AC 95-05 (1995).

[9] H. L. Lai *et al.*, *Improved Parton Distributions from Global Analysis of Recent Deep Inelastic Scattering and Inclusive Jet Data*, Phys. Rev. D **55** (1997) 1280.

[10] The ATLAS Collaboration, *Atlas Detector and Physics Performance, Volume II*, CERN/LHCC 99-15 (1999).

[11] M. Spira and P. M. Zerwas, *Electroweak Symmetry Breaking and Higgs Physics*, CERN-TH/97-379 (1997).

[12] F. Gianotti and M. Pepe-Altarelli, *Precision Physics at LHC*, Nucl. Phys. **B89** (Proc. Suppl.) (2000) 177.

[13] The CMS Collaboration, *Technical Proposal*, CERN/LHCC 94-38, LHCC/P1 (1994).

[14] The CMS Collaboration, *The Magnet Project: Technical Design Report*, CERN/LHCC 97-10, CMS TDR 1 (1997).

[15] The CMS Collaboration, *The Tracker Project: Technical Design Report*, CERN/LHCC 98-6, CMS TDR 5 (1998).

[16] The CMS Collaboration, *Addendum to the CMS Tracker Technical Design Report*, CERN/LHCC 2000-016, CMS TDR 5 Addendum 1 (2000).

[17] The CMS Collaboration, *The Electromagnetic Calorimeter Project: Technical Design Report*, CERN/LHCC 97-33, CMS TDR 4 (1997).

[18] The CMS Collaboration, *The Hadronic Calorimeter: Technical Design Report*, CERN/LHCC 97-31, CMS TDR 2 (1997).

[19] The CMS Collaboration, *The Muon Project, Technical Design Report*, CERN/LHCC 97-32, CMS TDR 3 (1997).

[20] F. Gasparini *et al.*, *Bunch Crossing Identification at LHC Using a Meantimer Technique*, Nucl. Inst. & Meth. **A336** (1993) 91.

[21] P. Arce *et al.*, *Bunched beam test of the CMS drift tubes local muon trigger*, Nucl. Inst. & Meth. **A534** (2004) 441.

[22] J. Christiansen, *A data driven high resolution Time-to-Digital Converter*, in *Proceedings of the 6th Workshop on electronics for LHC experiments*, Cracow, Poland, 11-15 September 2000. Available in CERN-LHCC-2000-041.

[23] The CMS Collaboration, *The Trigger Project, Technical Design Report: The Level-1 Trigger*, CERN/LHCC 2000-038, CMS TDR 6.1 (2000).

[24] The CMS Collaboration, *The TriDAS Project, Technical Design Report: Data Acquisition and High-Level Trigger*, CERN/LHCC 02-26, CMS TDR 6.1 (2002).

[25] N. Amapane *et al.*, *Monte Carlo Simulation of Inclusive Single- and Di-Muon Samples*, CMS NOTE 2002/041.

[26] H. Sakulin, *Design and Simulation of the First Level Global Muon Trigger for the CMS Experiment at CERN*, PhD thesis (2002).

[27] R. E. Kalman, *A New Approach to Linear Filtering and Prediction Problems*, Transaction of the ASME–Journal of Basic Engineering (1960) 35.

[28] The Geant4 Collaboration, *GEANT – Detector Description and Simulation Tool* .
http://wwwinfo.cern.ch/asd/geant4/

[29] J. Puerta-Pelayo, M. C. Fouz and P. Garcia-Abia, *Parametrization of the Response of the Muon Barrel Drift Tubes*, CMS Note **2005/018** (2005).

[30] R. Veenhof, *Garfield, a Drift-Chamber Simulation Program user's guide*, CERN Program Library W5050 (1994).

[31] I. Smirnov, *HEED. Interaction of particles with gases*, CERN Program Library Writeup W5060 .
http://consult.cern.ch/writeup/heed/

[32] M. Aguilar-Benítez *et al.*, *Test Beam Results Obtained with the Q4 Prototype*, Nucl. Instr. and Met. A **480** (2002) 658.

[33] M. Cerrada *et al.*, *Results from the Analysis of the Test Beam Data taken with the Barrel Muon Protoype Q4*, CMS NOTE **2001/041** (2001).

[34] F. Cavallo *et al.*, *Test of MB3 Muon Barrel Drift Chamber with Cosmic Rays*, CMS Note **2003/017** (2003).

[35] *IGUANA Web Site*, Located at http://iguana.web.cern.ch/iguana/.

[36] G. Alverson, G. Eulisse, S. Muzaffar *et al.*, *IGUANA Architecture, Framework and Toolkit for Interactive Gr aphics*, ECONF **C0303241** (2003) MOLT008. cs.se/0306042.

[37] C. Autermann *et al.*, *Test Beam Analysis of the First CMS MB2 Drift Tube Muon Chamber*, CMS NOTE 2003/007.

[38] J. Fernández de Trocòniz *et al.*, *Calibration and alignment procedures at the 2001 testbeam analysis*, CMS IN 2003/020.

[39] M. Aldaya *et al.*, *Fine synchronization of the muon drift tubes local trigger*, Nucl. Inst. & Meth. **A564** (2006) 169.

[40] M. Aldaya *et al.*, *Results of the First Integration Test of the CMS Drift Tubes Muon Trigger*, CMS NOTE **2006/072** (2006).

[41] N. Amapane *et al.*, *Comparison of DT testbeam results on local track reconstruction with the OSCAR + ORCA simulation*, CMS Note **2006/009** (2006).

[42] J. Puerta-Pelayo, *Estudio sobre las Camaras de Tubos de Deriva para el Espectrometro de Muones del Experimento CMS*, Ph.D. thesis, CIEMAT Madrid, January 2004.

[43] M. De Giorgi *et al.*, *Design and Simulation of the Trigger Electronics for the CMS Barrel Muon Chambers*, CMS TN/95-001 .

[44] M. Giunta, *Private communication.*